

One Model to Rule them All: Towards Universal Segmentation for Medical Images with Text Prompts

Ziheng Zhao^{1,2}, Yao Zhang², Chaoyi Wu^{1,2}, Xiaoman Zhang^{1,2},
Ya Zhang^{1,2}, Yanfeng Wang^{1,2,†} and Weidi Xie^{1,2,†}

¹CMIC, Shanghai Jiao Tong University ²Shanghai AI Laboratory

Abstract. In this study, we focus on building up a model that aims to **Segment Anything** in medical scenarios, driven by **Text** prompts, termed as **SAT**. Our main contributions are three folds: (i) for dataset construction, we combine multiple knowledge sources to construct the first multi-modal knowledge tree on human anatomy, including 6502 anatomical terminologies; Then we build up the largest and most comprehensive segmentation dataset for training, by collecting over 22K 3D medical image scans from 72 segmentation datasets with careful standardization on both image scans and label space; (ii) for architecture design, we formulate a universal segmentation model, that can be prompted by inputting medical terminologies in text form. We present knowledge-enhanced representation learning on the combination of a large number of datasets; (iii) for model evaluation, we train a **SAT-Pro** with only **447M parameters**, to segment **72 different segmentation datasets** with text prompt, resulting in **497 classes**. We have thoroughly evaluated the model from three aspects: averaged by body regions, averaged by classes, and average by datasets, demonstrating comparable performance to **72 specialist nnU-Nets**, *i.e.*, we train nnU-Net models on each dataset/subset, resulting in 72 nnU-Nets with around **2.2B parameters** for the 72 datasets. We will release all the codes, and models in this work.

1 Introduction

Medical image segmentation involves identifying and delineating regions of interest (ROIs) like organs, lesions, and tissues in diverse medical images, which plays a crucial role in numerous clinical applications, such as disease diagnosis, treatment planning, and disease progression tracking [105, 113, 7, 79]. Traditionally, radiologists perform manual segmentation to measure volume, shape, and location in a slice-wise manner, which is both time-consuming and challenging to scale with the growing volume of medical data. Consequently, there is a pressing need for automated and robust medical image segmentation methods in clinical settings, to enhance efficiency and scalability.

Recent advancements in medical image analysis have been marked by a surge of deep learning. These developments have yielded a spectrum of segmentation models, each trained for specific tasks [71, 70, 5, 80, 7, 35, 69], often referred to as ‘specialist’ models. While these models demonstrate impressive segmentation capabilities, their major drawback lies in the narrow specialization. Designed and optimized for distinct ROIs and imaging modalities, these models [30, 32, 38, 75, 92] require distinct preprocessing methods for each dataset. As a result, they often fall short in diverse and dynamic clinical environments, where adaptability to new conditions and imaging techniques is essential.

There is a growing interest in developing universal models for medical image segmentation [68, 37], by adapting the pre-trained Segment Anything Model (SAM) [46] models from the computer vision community. However, while transferring to medical scenarios, these models trained on natural images suffer from fundamental limitations: (i) models typically perform 2D slice segmentation, that are later fused into 3D volumes through post-processing. This approach overlooks the critical contextual information inherent in 3D radiological imaging; (ii) models often require point or box inputs as prompts, thus is an interactive segmentation model, requiring considerable manual efforts for use in practice; (iii) models suffer from significant domain gaps, from image statistics to domain-specific medical knowledge, *e.g.*, ‘liver is distinctive for positioning in the upper-right part of the abdominal cavity, filling almost the entire right hypochondrium and often extending into the left hypochondrium as far as the mammillary line’.

In this paper, we present the **first knowledge-enhanced** universal model for 3D medical volume segmentation,

† Corresponding Authors.

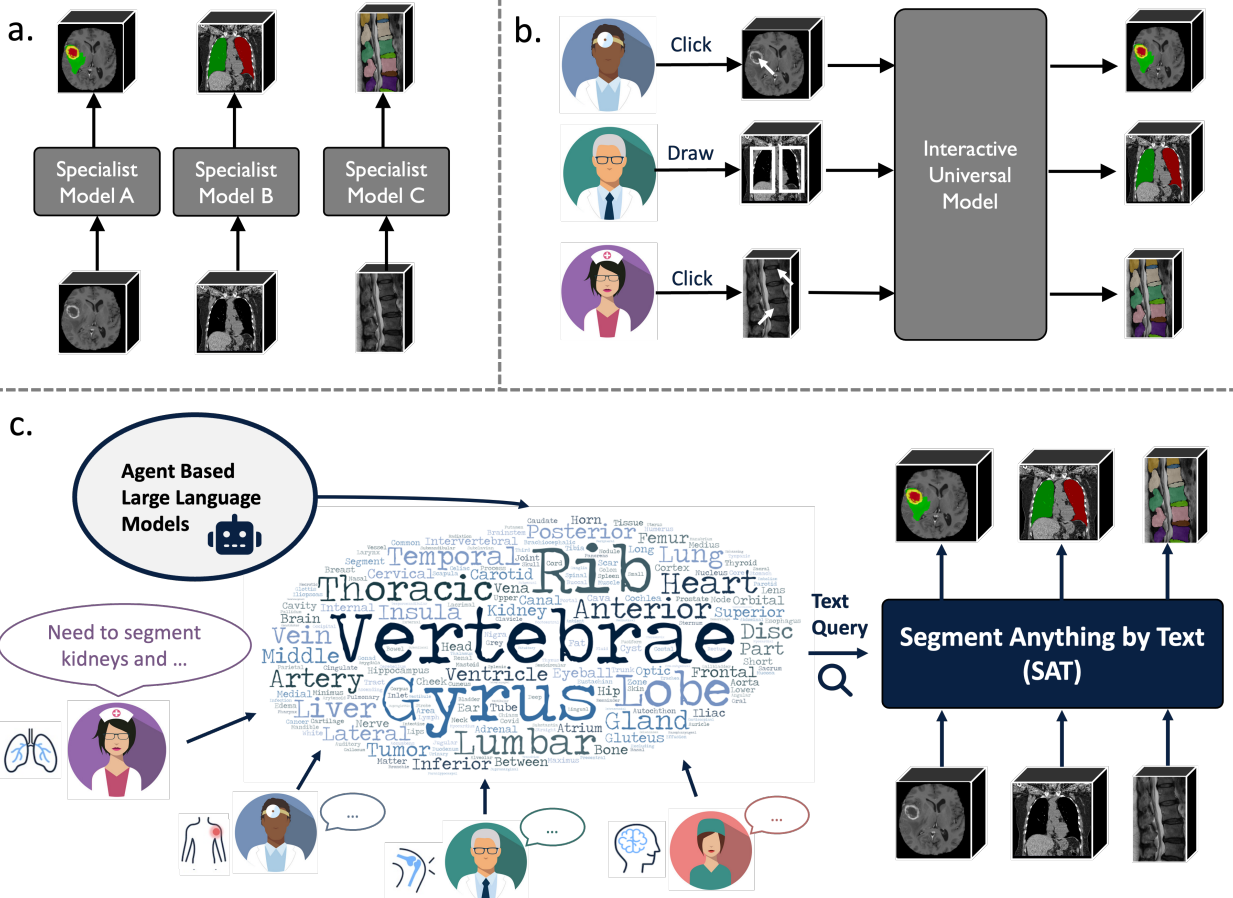


Figure 1 | Different from conventional specialist models (a) that develop specialized solution for each task, or recently proposed interactive universal segmentation models (b) relying on real-time human interventions, Segment Anything with Text (SAT) utilizes text prompts as queries and 3D volumes as inputs to perform a wide array of medical image segmentation tasks across different modalities, anatomies, and body regions (c). It can be easily applied to clinics or seamlessly integrated with any agent-based large language model.

with language/text as prompt, termed as SAT. In practice, our model can effectively take 3D volume as visual inputs along with text prompts, to seamlessly tackle various medical image segmentation tasks, across modalities, anatomies, and body regions. As illustrated in Fig. 1, our proposed method distinguish from previous medical segmentation paradigms, can be seamlessly applied to clinics or integrated with any large language model. Specifically, we make the following contributions:

On dataset construction, we construct a knowledge tree based on multiple medical knowledge sources, encompassing thousands of anatomy concepts and definitions throughout the human body. On the visual side, we curate over 22K 3D medical image scans with 302K anatomical segmentation annotations, covering 497 categories from 72 publicly available medical segmentation datasets, termed as **SAT-DS**. To the best of our knowledge, **SAT-DS denotes the largest and most comprehensive collection of public 3D medical segmentation datasets.** To achieve such goal, we have invested significant efforts in standardizing datasets and unifying annotation labels, paving the way for universal segmentation task. For complete list of datasets and download links, we refer the reader to Table 13 and Table 14.

On architecture design and training strategy, we build a universal medical segmentation model that leverages text prompts to guide segmentation, that enables flexible segmentation across a spectrum of medical imaging modalities. Specifically, we adopt knowledge-enhanced representation learning, leveraging textual anatomical knowledge and atlas segmentation of specific anatomical structure to train the text encoder. Through this training process, the visual features of these anatomical structures are aligned with their

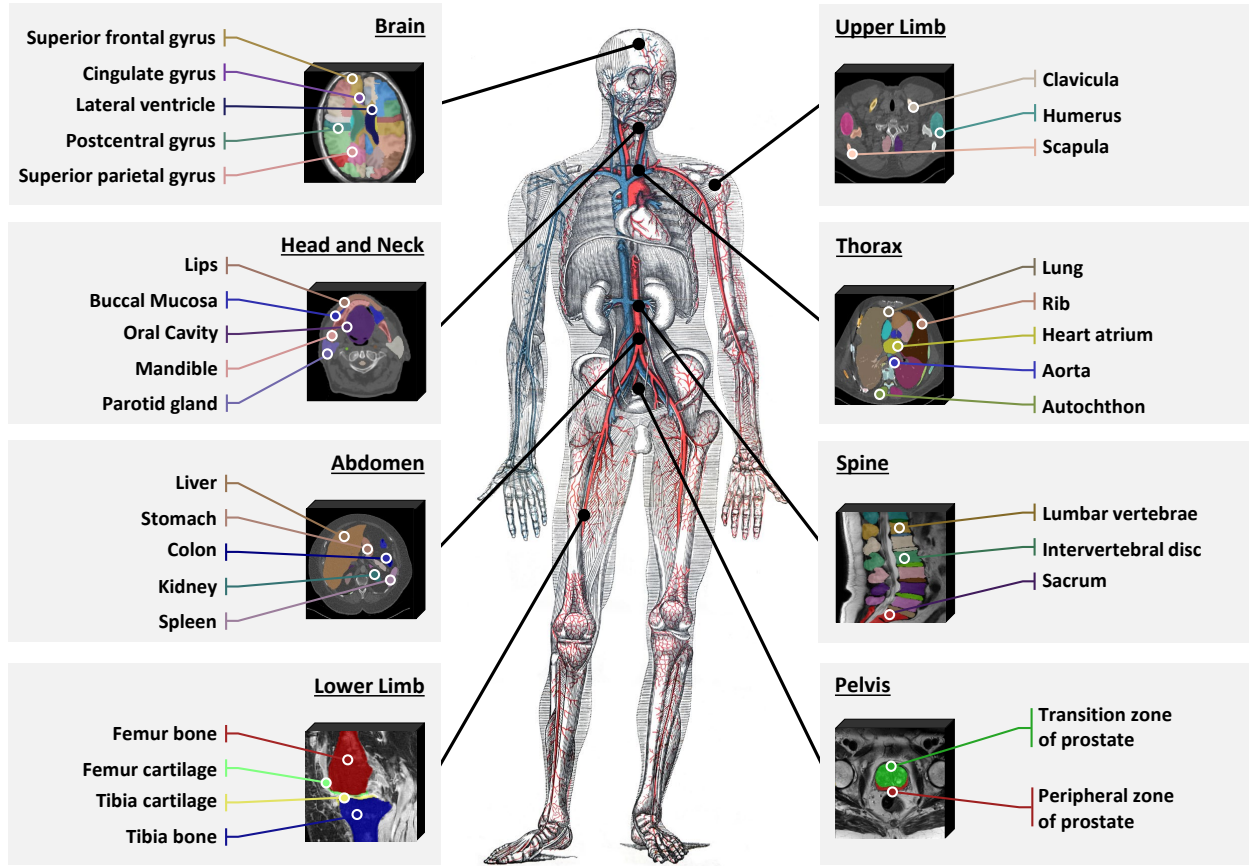


Figure 2 | Overview of our dataset for training universal segmentation model. Specifically, we collect datasets from a wide range of segmentation tasks across various modalities and anatomical regions of the human body, including the brain, head and neck, thorax, spine, abdomen, upper limb, lower limb, and pelvis.

corresponding text descriptions in the latent space. Later, the text embeddings of anatomy/abnormality are treated as queries in a Transformer-based architecture, enabling the model to selectively extract task-specific features for precise segmentation of the queried target. To satisfy the requirements from different computational resources, we train two models of varying sizes, namely, **SAT-Nano**, and **SAT-Pro**.

On evaluation, we devise comprehensive metrics for universal medical segmentation across various aspects, including region-wise average, organ-wise average, and dataset-wise average. Through extensive experiments, we demonstrate that:

- Building on the unprecedented dataset collection, SAT-Pro with only 447M parameters, can employ flexible text prompts for a wide range of downstream segmentation tasks, showing comparable performance to specialist nnU-Net models trained individually on each dataset, *i.e.*, results from 72 separate nnU-Net models.
- Benefiting from the standardized data processing and unified label system, SAT show excellent generalisation ability when performing zero-shot transfer to clinic data. It is worth emphasizing that SAT can flexibly satisfy the clinical needs of doctors from different departments, without any additional annotation and training.
- Enhanced by multimodal medical domain knowledge, our text encoder provides superior guidance for universal medical segmentation on 3D inputs, surpassing the state-of-the-art language model tailored for medical tasks. For the first time, we demonstrate how domain knowledge would facilitate the segmentation task.
- While enlarging model capacity, *i.e.*, from SAT-Nano to SAT-Pro, would significantly improve the

segmentation performance. This reveals the promising yet still under-exploited potential of a universal medical segmentation model.

- The text-prompted feature distinguishes SAT from all previous universal medical segmentation models that require human interaction. We demonstrate how SAT can be directly integrated with large language models like GPT-4 [2], automatically segmenting the targets of interests without human intervention.

2 Results

The goal of our proposed SAT is to build an universal segmentation for 3D medical images, driven by text prompt. Such method should be capable of handling diverse segmentation tasks excellently in one model, without laborious specialization and training for each single dataset. In addition, the universality should make it adaptable to clinic procedures with minimal extra efforts, addressing a broad range of clinical needs; and the text-driven character should equip it with immense potential as a flexible toolkit, bridging between language and segmentation. Also, to meet different hardware requirements, we train two variants of SAT, namely SAT-Pro and SAT-Nano.

2.1 Main Results

Building an universal segmentation model poses several new challenges compared to specialist models, such as the heterogeneity of data, the long-tail distribution, the limitation from model capacity and so on. To this end, we have constructed a large-scale training set, namely SAT-DS dataset, covering a wide spectrum of medical image segmentation tasks, covering 497 anatomical targets on 8 regions and lesions of the human body, across 72 datasets. We train two universal segmentation models, namely, SAT-Pro and SAT-Nano, and compare them with the powerful specialist model, *i.e.*, nnU-Nets trained on each dataset. To comprehensively understand such capability, we conduct the evaluations from the perspective of anatomical regions, classes, and datasets respectively. **Note that**, class-wise and region-wise evaluations require averaging results across different nnU-Nets. For example, the results on ‘brainstem’ in CT images is the macro average of nnU-Nets trained on ‘HAN Seg’, ‘PDDCA’ and ‘SegRap2023 Task 1’, since all these datasets contains annotation for this class.

2.1.1 Region-wise Results.

Table 1 shows the segmentation performance of our methods and nnU-Nets on 8 regions of human body, including Brain, Head and Neck, Thorax, Abdomen, Pelvis, Spine, Upper Limb, and Lower Limb, as well as Lesion, in terms of DSC and NSD, respectively. Classes existing in multiple regions are specifically grouped as Whole Body. Notably, SAT-Pro consistently outperforms nnU-Nets in three regions: on Head and Neck, it surpasses nnU-Nets by 5.21 on DSC and 8.27 on NSD; On Upper Limb, it surpasses nnU-Nets by 2.8 on DSC and 9.28 on NSD; On Lower Limb, it leads to 1.53 on DSC and 2.48 on NSD. SAT-Nano rank last in almost all the regions, except for Spine, where it slightly exceeds SAT-Pro by 0.82 on DSC and 0.81 on NSD.

For comparison, we visualize the results in Fig. 3 (c). Overall, SAT-Pro shows comparable segmentation performance to the 72 nnU-Nets, that are specialized for each dataset, and outperforms SAT-Nano in most cases. In addition, it’s worth noticing that SAT-Pro not only performs better, more flexible, but also significantly smaller, approximately $1/5$ of the assemble of nnU-Nets; While SAT-Nano is even smaller, remarkably only $1/20$ of the assemble of nnU-Nets in size.

2.1.2 Class-wise Results.

For a more detailed evaluation, we show the results on all 497 classes in Fig. 4 and Fig. 5. Classes from the same region are clustered together and sorted from high to low according to the results of SAT-Pro. The scores of SAT-Pro, SAT-Nano, nnU-Nets on the same class are plotted in a vertical line. Statistics over all classes show that SAT-Pro outperforms SAT-Nano on most classes: 439/497 on DSC, and 442/497 on NSD; Meanwhile, SAT-Pro exceeds nnU-Nets on 133/497 classes on DSC, and 192/497 classes on NSD, including some important segmentation classes such as liver (+2.15 on DSC & +1.43 on NSD), pancreas (+0.83 & +2.76), lumbar vertebrae (+10.69 & +14.05). Averaging over all 497 classes, SAT-Pro achieves 78.73 on DSC,

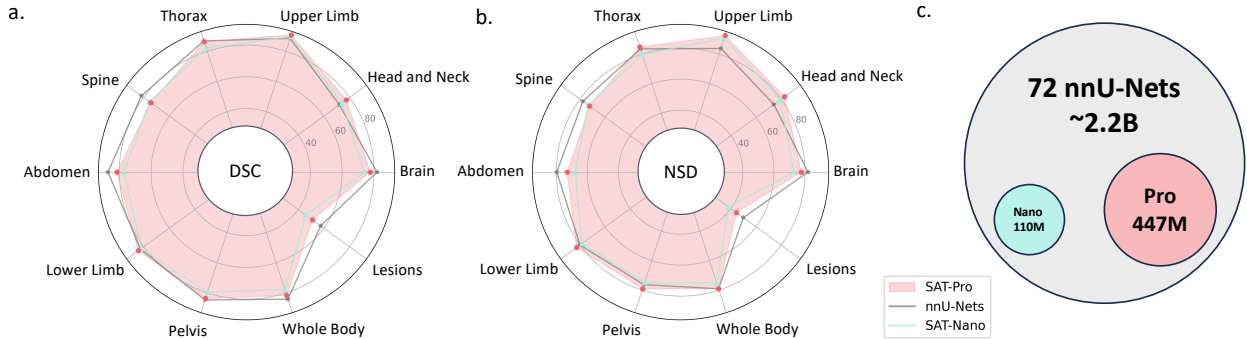


Figure 3 | Comparison between SAT-Nano, SAT-Pro and nnU-Nets on different regions and lesions. (a) Dice score comparison; (b) NSD score comparison; (c) Model size comparison. **SAT-Pro** is approximately 5 times smaller than the total size of all the specialist nnU-Nets, while SAT-Nano is merely one twentieth the total size of all the specialist nnU-Nets.

Table 1 | Segmentation results on different regions of human body and lesion. The best results are underlined. H&N: head and neck, LL: lower limb, UL: upper limb, WB: whole body.

Metric	Method	Brain	H&N	UL	Thorax	Spine	Abdomen	LL	Pelvis	WB	Lesion
DSC \uparrow	nnU-Nets	<u>81.93</u>	72.08	88.54	<u>86.90</u>	<u>81.75</u>	87.05	82.48	84.68	<u>84.14</u>	<u>57.52</u>
	SAT-Pro	77.70	<u>77.29</u>	<u>91.34</u>	86.38	74.73	81.47	<u>84.01</u>	83.01	82.19	51.39
	SAT-Nano	73.90	74.08	89.58	82.09	75.55	77.12	81.79	79.50	77.80	46.04
NSD \uparrow	nnU-Nets	<u>81.96</u>	74.18	83.86	83.55	<u>77.72</u>	<u>79.70</u>	80.02	76.34	79.11	<u>49.89</u>
	SAT-Pro	<u>77.77</u>	<u>82.45</u>	<u>93.14</u>	<u>84.80</u>	72.87	72.94	<u>82.50</u>	<u>78.66</u>	<u>79.61</u>	44.62
	SAT-Nano	72.95	79.15	90.94	79.68	73.68	67.83	78.42	74.89	75.36	38.17

which is about 4.26% improvement over SAT-Nano (75.51); and 77.71 on NSD, about 5.31% improvement over SAT-Nano (73.76). Compared with nnU-Nets, SAT-Pro achieves 97.55% the performance of nnU-Nets on DSC and 99.32% the performance of nnU-Nets on NSD, demonstrating very competitive segmentation performance as an universal model. We report the detailed class-wise and dataset-wise results in Table 3, Table 4 and Table 2.

2.2 Ablation Study

As will be illustrated in Sec. 6, to build an universal segmentation model driven by text prompts, we devise the visual encoder and decoder to process diverse medical images and perform segmentation; Meanwhile, domain knowledge is injected into the text encoder to provide precise prompts for the segmentation target, *i.e.*, the encoding of terminology. In this section, we conduct experiments and discuss the effect of different visual backbones and domain knowledge in SAT. To save computational cost, all the experiment in this section are conduct on a subset of SAT-DS, termed ast SAT-DS-Nano. It includes 49 datasets, 13,303 images, 151,461 annotations and 429 classes.

2.2.1 Effect of Visual Backbone

Extensive studies have been done discussing the applicability of different visual backbones across segmentation tasks. However, it remains unexplored on which visual backbone suits the need of universal segmentation. In addition to the ConvNet-based U-Net, we consider two alternative backbones, namely, SwinUNETR [31] and U-Mamba [29] to medical segmentation. We configure three SAT-Nano variants with SwinUNETR(107M), U-Mamba(114M) and U-Net(110M) in comparable size: For SwinUNETR, we use the same hypeparameters as in official implementation [30]; For U-Mamba, we refer to the official implementation [67], reserve configuration of the U-Net in SAT-Nano, and only add mamba layers at the end of last 3 blocks of the U-Net encoder.

To avoid repeating multimodal knowledge injection on each visual backbones, we use MedCPT [42] for all these variants as text encoder, without loss of generality. Like the text encoder we pre-trained in Sec. 6.2, MedCPT

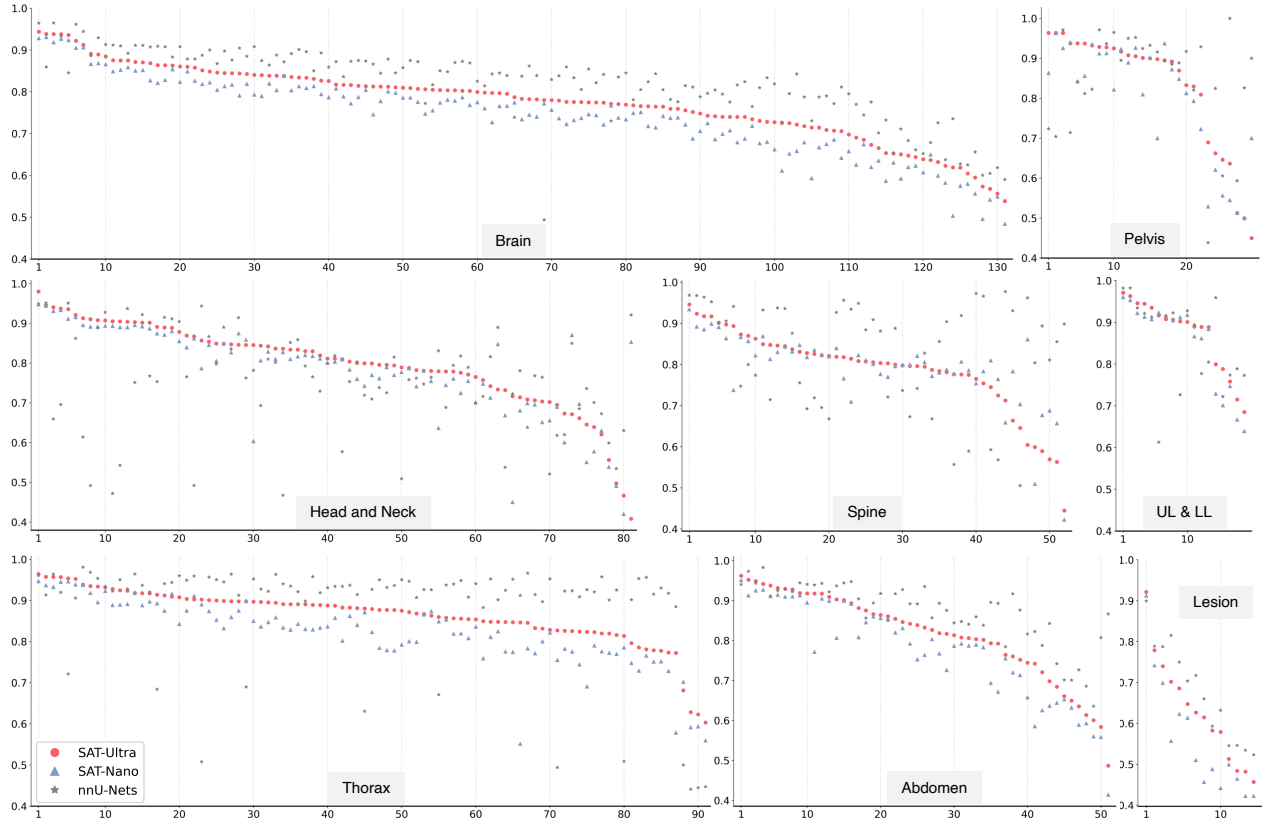


Figure 4 | DSC scores of SAT-Nano, SAT-Pro and nnU-Nets on each class. Classes from the same region are clustered together and sorted from high to low according to the results of SAT-Pro.

is a text encoder trained on 255 million in-house user click logs from PubMed [91], and shows state-of-the-art performance on various biomedical language tasks. We expect it to possess domain knowledge and embed terminologies properly as text prompts. Thus, we denote these variants as U-NET-CPT, SwinUNETR-CPT and U-Mamba-CPT. We demonstrate the region-wise evaluation results in Fig. 6. U-Net-CPT outperforms U-Mamba-CPT slightly on both DSC (0.35) and NSD (0.22) scores averaged over all classes. However, both U-Net-CPT and U-Mamba-CPT exceed SwinUNETR-CPT by a significant margin. These observations confirm our choice of U-Net as the visual backbone of SAT. For more detailed comparison on each dataset and class, we refer the reader to Table 8, Table 9 and Table 10.

2.2.2 Effect of Text Encoder

For an universal segmentation model with text as prompts, the neural representations of anatomical structures and lesions serve as the guidance for the segmentation model. And thus, the choice of text encoder should be carefully studied. In this section, we investigate the impact of domain knowledge on building a text encoder for medical universal segmentation task. Specifically, we train three SAT-Nano models with three representative text encoders: the text encoder pre-trained on our multimodal medical knowledge graph, as illustrated in Sec. 6.2; the state-of-the-art text encoder for various medical language tasks, *i.e.*, MedCPT; And BERT-Base, a prevalent text encoder in natural language processing but not specifically finetuned on medical corpus. For all the variants, we use U-Net as visual backbone, and denote them as U-Net-Ours, U-Net-CPT, U-Net-BB.

Region-wise evaluation. As shown in Fig. 7, the performance of U-Net-CPT and U-Net-BB are close, with U-Net-CPT slightly outperforms U-Net-BB on both DSC (+0.43) and NSD (+0.52) scores averaged over all classes, suggesting that finetuned on medical corpus, MedCPT might hold minor advantage. By contrast, U-Net-Ours surpasses U-Net-CPT consistently on all regions and lesions, leading notable margins on both DSC (+1.54) and NSD (+2.65) scores after average over all classes. This demonstrates the effectiveness of

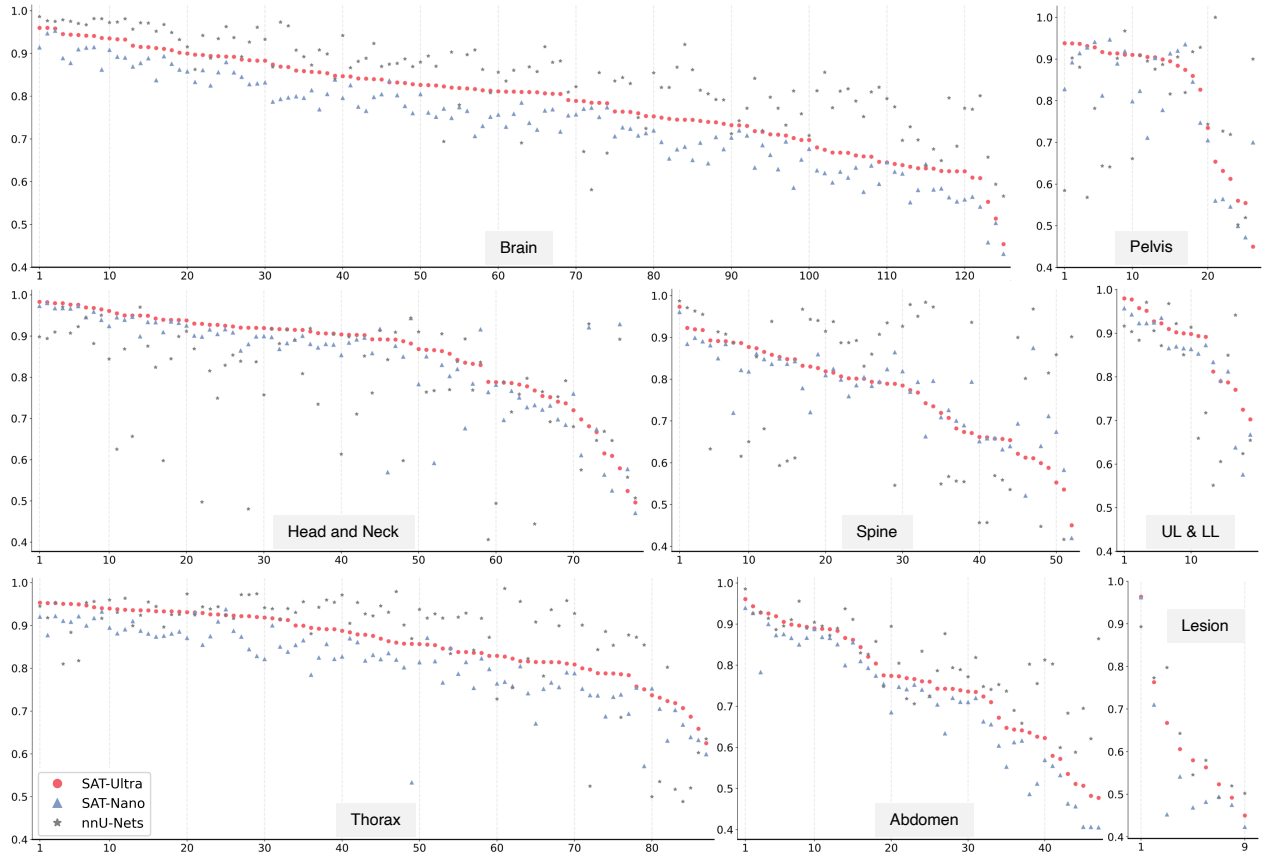


Figure 5 | NSD scores of SAT-Nano, SAT-Pro and nnU-Nets on each classes. Classes from the same region are clustered together and sorted from high to low according to the results of SAT-Pro.

multimodal knowledge injection for training SAT. For more detailed comparison on each dataset and class, we refer the reader to Table 5, Table 6 and Table 7.

Concept-to-definition retrieval. To demonstrate the advantage of our proposed knowledge injection on capturing the critical features of medical terminologies, we evaluate the three text encoders on concept to definition retrieval task, with the human anatomy knowledge we collect, totaling 6,502 anatomy concepts and definition pairs. We find that the recall at 1 (R1) for BERT-Base is merely 0.08%, suggesting it can hardly understand these anatomy concepts or possess almost no domain knowledge; The R1 for MedCPT is 11.19%. Though this is a significant improvement over BERT-Base, MedCPT still struggles to distinguish these concepts; By contrast, our proposed text encoder gets 99.18% R1, indicating the knowledge is successfully injected into the text embedding for each anatomy concept.

Knowledge injection helps segmentation of long-tail classes. The 429 classes in SAT-DS-Nano follow a typical long-tail distribution, as illustrated in Fig. 8 (a) and (b). The 10 classes with maximum annotations account for 12.75% of all the annotations in SAT-DS-Nano, denoted as ‘head’ classes; On contrast, the 150 classes with minimum annotations only accounts for 3.25%, even though they comprise 34.97% of 429 classes. We compare U-Net-Ours, U-Net-CPT and U-Net-BB on the ‘head’ classes, ‘tail’ classes and the rest ones (denoted as ‘middle’ classes). In Fig. 8 (c), we observe that prompted by our proposed text-encoder, U-Net-Ours achieves the best performance on all three type of classes. On ‘head’ classes, it outperforms the second best variant by 0.71 on DSC and 2.44 on NSD. While on ‘tail’ classes, the improvement is even more significant: 1.4 on DSC and 3.23 on NSD. Meanwhile, U-Net-CPT is better than U-Net-BB on ‘tail’ but slightly underperform on ‘head’. These results suggest our proposed text encoder is consistently better in a long-tail distribution, and the knowledge injection can effectively boost the segmentation performance on ‘tail’ classes.

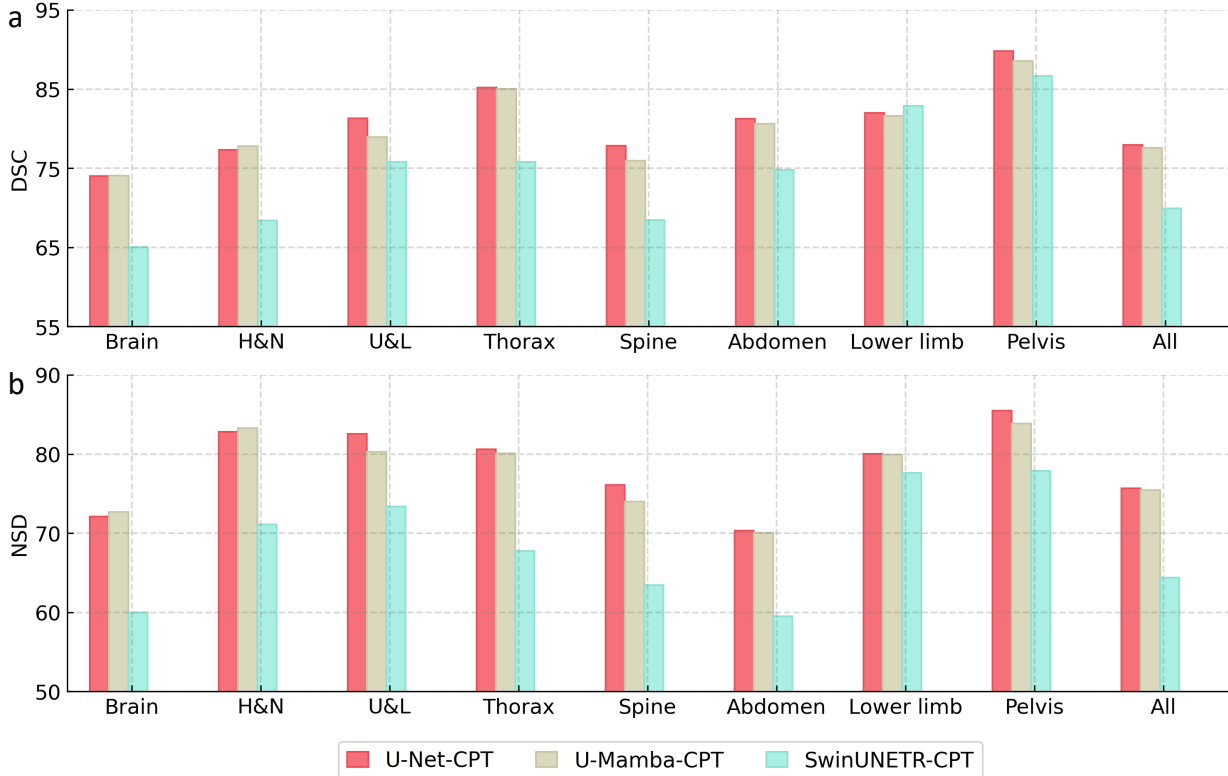


Figure 6 | Evaluations on different visual backbones on SAT-DS-Nano. ‘All’ denote the average scores over all the classes($n=429$), including lesion classes. (a) DSC comparison; (b) NSD comparison. U-Net-CPT and U-Mamba-CPT perform very close, while both surpass SwinUNETR-CPT considerably.

2.3 Qualitative Results in Different Scenarios

Benefiting from the universality and text-driven features of SAT, it can be flexibly applied in clinic scenario. We verify such capability qualitatively on real clinic data. As opposed to previous universal segmentation model [46, 68, 14] that strictly relies on human interactions, SAT is built on knowledge enhanced text prompts, that can precisely understand the segmentation needs in text-form, regardless the user is a human or machine.

We utilize GPT-4 [2] to directly extract the anatomical targets of interests from real clinical report and prompt SAT to segment them on the clinical image, **forming a fully automatic pipeline**. In Fig. 9 and Fig. 10, we demonstrate the zero-shot performance of SAT-Pro on four cases randomly selected from clinical practice: abdominal MR examination, chest CT examination, abdominal CT examination, and lumbar spine CT examination. The basic information of patients, the report written by doctors, and targets of interests detected by GPT-4 are attached to each cases. As can be seen, the targets in reports are well detected by GPT-4 and commendably segmented by SAT-Pro: In Fig. 9, Liver, Pancreas, Kidneys, Gallbladder and Spleen are segmented in both abdominal CT and MR images; While in Fig. 10, segments of right lung, heart and bronchi are segmented in thoracic CT image, lumbar vertebrae L1 to L5 are segmented in spinal CT image. Note that in this evaluation, **SAT-Pro is not fine-tuned on any data out of SAT-DS**, despite the diversity of image and segmentation targets.

3 Discussion

The heterogeneity of medical images has long called for versatile, effective and flexible universal medical segmentation model to meet clinical needs. To this end, we proposed SAT, a universal medical segmentation model trained on unprecedented dataset collection, and driven by knowledge enhanced text prompt. In this section, we discuss the performance, potential and limitations of the proposed SAT, based on our experiment

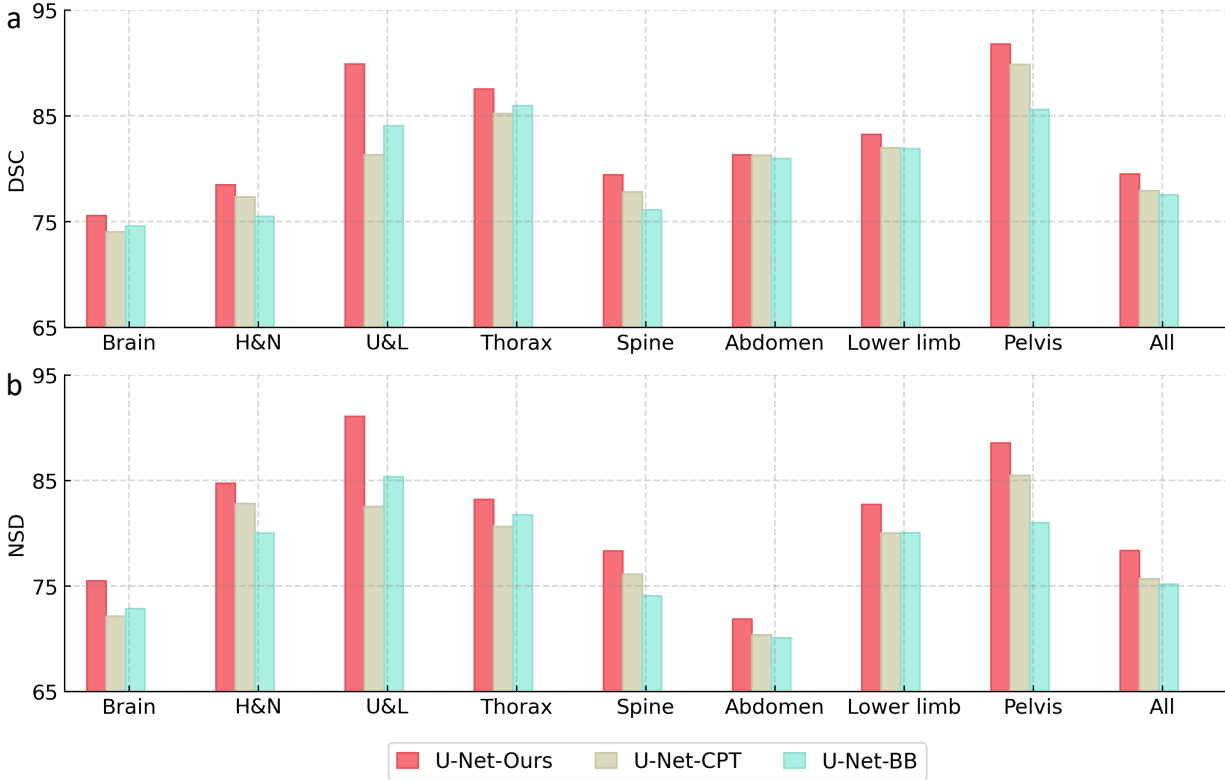


Figure 7 | Evaluations on different text encoders on SAT-DS-Nano. ‘All’ denote the average scores over all the classes(n=429), including lesion classes. (a) DSC comparison; (b) NSD comparison. Prompted by MedCPT, SAT achieves better performance over BERT-base on average over all the classes. While our pre-trained text encoder outperforms MedCPT consistently across all the regions and lesion.

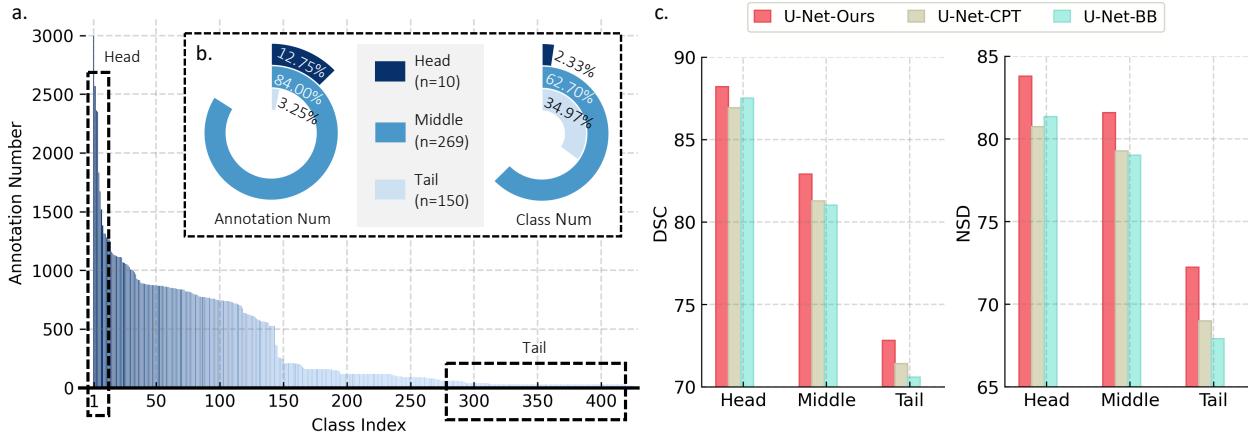


Figure 8 | The impact of domain knowledge on a long-tail distribution. (a) The annotation number of all the 429 classes in SAT-DS-Nano, sorted from highest to lowest. (b) The proportion of ‘head’, ‘middle’ and ‘tail’ in class number and annotation number. The DSC and NSD comparison on ‘head’, ‘middle’ and ‘tail’ classes.

results in Sec. 2.

An universal model is worth 72 specialist models. Through comprehensive experiments in both region-wise and class-wise evaluations, SAT-Pro has demonstrated comparable results to an assemble of 72 nnU-Nets specialized and trained on each dataset, and even surpass them on several regions and classes.

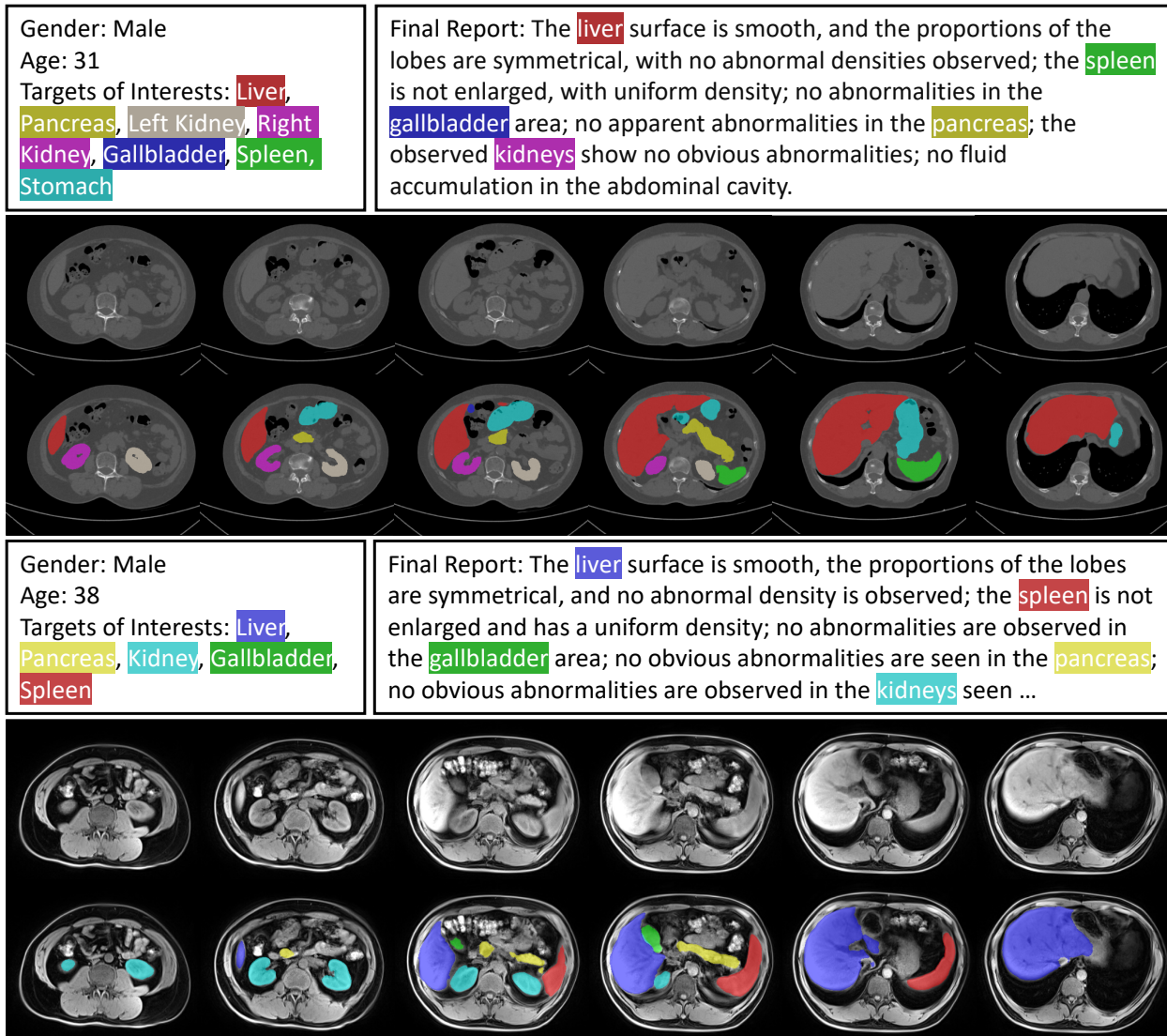


Figure 9 | Zero-shot transfer to real clinical data. Top: A case from abdominal CT examination, no abnormal is observed from the CT image; Bottom: A case from abdominal MR examination, no abnormal is observed from the MR image; Basic information of patients, predefined targets of interests, and final reports written based on the segmentation results were appended to each cases.

These promising results reveal universal segmentation model as a much more flexible method qualified for wide range of tasks. Even more impressive, SAT-Pro is of much smaller size, implying a more cost-effective alternative to training and deploying a series of specialist models.

Scaling models lead to better performance. Increasing model capacity has been demonstrated to effectively enhance model’s performance in large language models [110, 99], yet such scaling law remains to be verified in segmentation tasks. In this work, we build SAT-Nano (110M) and SAT-Pro (447M). In both region-wise and class-wise evaluations, SAT-Pro shows clear performance boost over SAT-Nano, outperforming the latter on most region and classes. This implies that scaling law is also applicable to universal medical segmentation, probably a promising way to continuously improve the performance.

Domain knowledge can boost segmentation performance. The impact of domain knowledge, especially multi-modal knowledge on human anatomy remains under-explored for segmentation task. In this work, we propose a multi-modal knowledge graph on human anatomy, and via knowledge injection, build a text encoder prompting the segmentation task. In Sec. 2.2.2, we demonstrate how it can enhance the segmentation

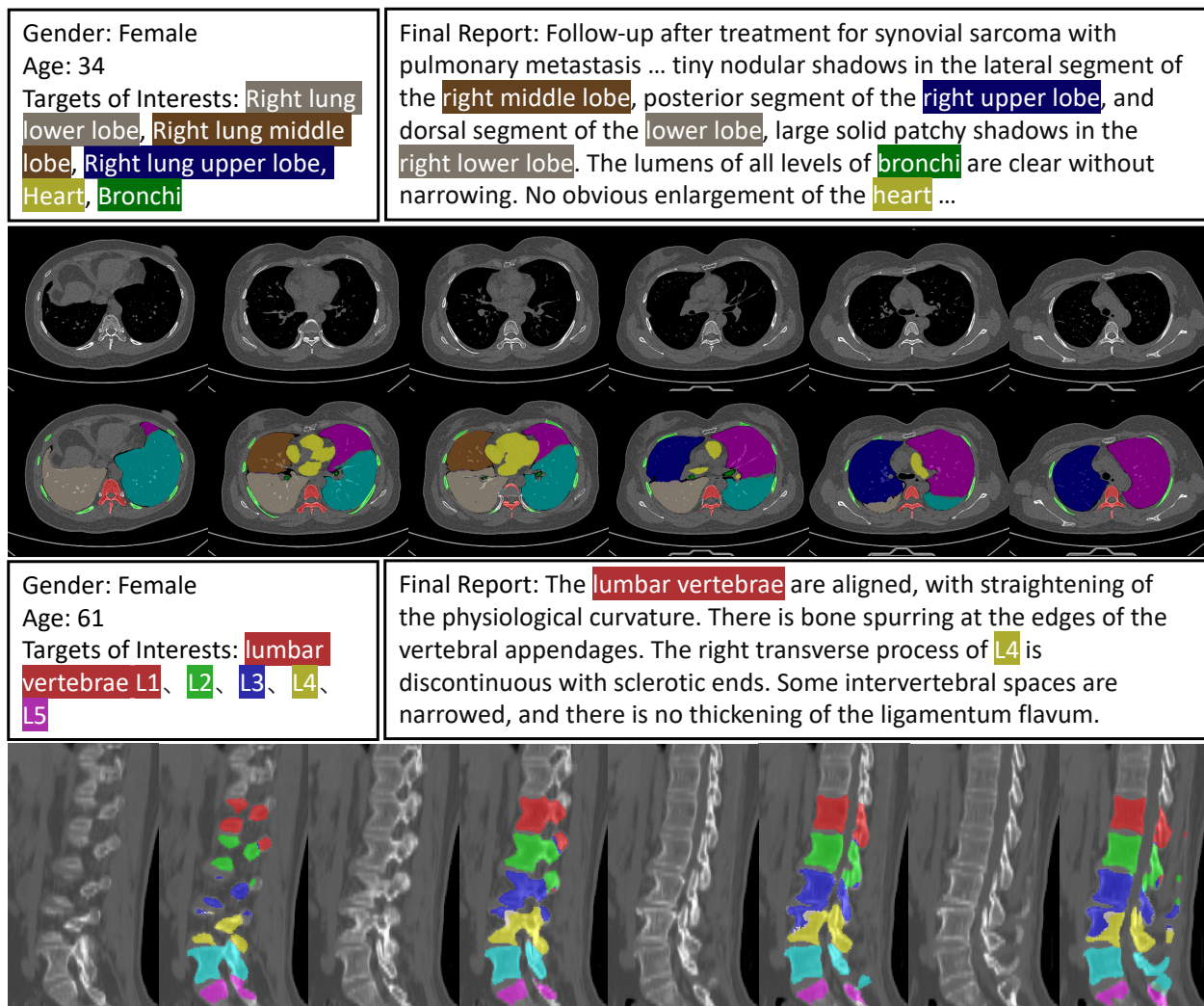


Figure 10 | Zero-shot transfer to real clinical data. Top: A case from chest CT examination, the patient is taking a follow-up examination after treatment for synovial sarcoma with pulmonary metastasis; Bottom: A case from lumbar vertebrae CT examination, some abnormalities are observed on the image; Basic information of patients, predefined targets of interests, and final reports written based on the segmentation results were appended to each cases.

performance, especially on these ‘tail’ classes. As we expect the segmentation targets in human body to continuously grow in the future, it will raise higher demand on generating informative and distinguishable text prompts.

SAT can be easily transferred to clinics. Clinic utility is crucial for segmentation methods. In Sec. 2.3, we show that SAT-Pro can be applied directly to real clinical data out of the scope of SAT-DS without extra annotation and fine-tuning. Despite the diversity of image and segmentation targets from different clinic scenes, SAT can flexibly handle them with just one model. This could save laborious efforts to collect, annotate and train a bag of specialist models. More importantly, SAT can be utilized with text prompts, saving the time for per-sample human intervention, thus functioning automatically with predefined targets, reducing the cost in real use. Furthermore, as we have normalized all the image with unified voxel spacing, the successful application of SAT in clinic would pave the way for estimating the spatial size of anatomical targets directly, providing reference for analysis, diagnosis and treatment.

SAT can be a powerful agent for large language models. In Sec. 2.3, we show that SAT can be applied to segment targets extracted by GPT-4 from clinical report, providing explainable grounded report for the patients. This demonstrates the potential of SAT as a powerful agent, seamlessly integrated with any large

language models, with text prompts bridging them. As grounding is an indispensable procedure in building generalist medical artificial intelligence [77], we expect the potential and significance of SAT to extend beyond a simple clinical tools.

Limitations. As an exploratory work in this field, though demonstrate impressive and promising results, we find certain limitation of SAT:

- *Firstly*, the performance of SAT-Pro still lags behind nnU-Net in some region including Brain, Spine and Abdomen, and many classes especially the lesions. This implies SAT, though flexible and versatile, can not fully replace specialist models, especially in scenarios where absolute performance is critical. However, we evaluate SAT-Pro on train set, derive its averaged DSC score of all class as 83.68. We suspect its performance is still unsaturated, and continuous scaling-up universal segmentation model may close the gap and even outperforms the counterparts specialist models.
- *Secondly*, SAT currently only supports text as prompts, thus not intended for scenes with human interaction requirements. For example, human annotation or refinement on the segmentation results.
- *Thirdly*, the distribution of SAT-DS is unbalanced, leading to the limitation on capability of SAT. For instance, SAT-DS contains 189 classes for MR images, while 137 exists in ‘Brain’ region. Comprehensive annotation for MR images still lags behind CT images in the scope of public datasets.
- *Fourthly*, because of the imbalance between different segmentation datasets, the long-tail distribution in assembled dataset collection remain challenging for building an universal segmentation method. As demonstrated in Fig. 8 (c), the performance gap between ‘head’, ‘middle’ and ‘tail’ classes is still significant.

4 Related work

4.1 Specialist Medical Image Segmentation

Recent years have witnessed significant advancements in the field of medical image segmentation for diverse clinical applications [84, 9, 69, 97, 5, 8, 71, 43, 70, 35, 66, 106]. Since the success of convolutional neural networks (CNNs), U-Net [92, 16, 38] have shown dominant performance for medical image segmentation, and the variants [75, 21, 57, 115, 125, 94, 119] are further developed to dive into specific clinical tasks. Meanwhile, the emerging Transformers [32, 12, 30, 112, 117, 14, 122] step in this field and obtain promising results. This stream of specialist methods typically employ a customly-designed solution and a supervised learning framework. Despite the success in specific segmentation tasks, it requires to be trained from scratch on a new segmentation task, posing limitation on the generalisability. More importantly, the data scarcity for specific tasks often significantly hamper the application in diverse and practical clinical scenarios. In this paper, we present a generalist model that covers a wide spectrum of medical image segmentation tasks.

4.2 Generalized Medical Image Segmentation

In the Medical Segmentation Decathlon [5], nnU-Net [38] takes a promising step towards generalized medical image segmentation. It offers an automatic pipeline to define the optimal network architecture and data pre-processing for each segmentation task. However, the issues of specialist model remain. It has to involve substantial overhead by training from scratch on each task, and the intrinsic correspondence among segmentation tasks is neglected. To effectively benefit a multitude of clinical segmentation tasks, advanced learning schemes have been proposed for generalized medical image segmentation, including multi-task learning [83, 120, 26, 24], transfer learning [13, 19, 104], and continual learning [118, 41, 124]. Multi-task learning incorporates multiple imaging modalities, *e.g.*, multi-parametric MR and multi-phase CT [83, 120], or anatomies, *e.g.*, multi-organ segmentation [24]. In contrast, transfer learning achieves generalized medical image segmentation by transferring segmentation model from one task to another, *e.g.*, from CT to MR image segmentation and vice versa [13]. Continual learning incrementally involve novel tasks into the segmentation model and avoid forgetting the old ones at the same time [41]. However, these methods require either a limited pre-defined set of tasks or substantial tuning on novel tasks, and thus can hardly scale up. The proposed method exploits textual prompt learning, *i.e.*, the term of the organs or lesions, to smoothly steer

the segmentation model to new tasks without costly training or tuning.

4.3 Universal Medical Image Segmentation

Universal medical image segmentation paves a way to superior generality and scalability by covering a wide range of organs and lesions across various medical imaging modalities and anatomies [37]. The universal model is usually driven by visual or textual prompts to adapt to various segmentation tasks. Since the significant success of SAM [46] in computer vision, several approaches follow the interactive framework and leverage box and/or point prompts to finetune the model on medical images [68, 37, 15, 102, 27]. Other methods also exploit image examples as visual prompts [11] or integrate visual prompts with textual prompts [22]. Despite showing promising results, these semi-automated approaches rely on carefully curated visual prompts, that may face critical challenges in clinical practice. Meanwhile, the typical 2D slice-wise segmentation in most visual prompting methods [68, 37, 15] inevitably leads to suboptimal context encoding for 3D medical imaging [27]. In contrast, pure textual prompts save the effort for burdensome interaction, especially when scaling up to tens of thousands of medical images. Several works have made successful attempts to adapt textual or learnable prompts for abdominal organ and lesion segmentation [61, 114], encouraging us to take a further step towards universal medical image segmentation. However, these studies still require a pre-defined set of categories and thus suffer from the shortage of medical domain knowledge, leading to limited generality across diverse medical segmentation tasks. To bridge this gap, we explicitly leverage multimodal medical knowledge composed of anatomy atlas and definition via visual language pre-training for universal medical image segmentation.

4.4 Knowledge-enhanced Representation Learning in Medical Image Analysis

As accurate medical image analysis relies on expert domain knowledge, several efforts have attempted to involve well-established medical knowledge to strengthen deep learning methods [111, 108]. These methods can be divided into two categories, namely, model-based and learning-based methods. Specifically, the model-based methods design the network architecture based on the clinical knowledge prior [55, 28] or mimicking the clinical practice [18, 23]. The learning-based methods exploit a multi-task learning scheme that takes medical knowledge as either inputs or additional supervision [107, 123]. Additionally, in the recent literature, [52, 89, 42] train or fine-tune language models with biomedical corpus [91, 10], boosting model performance over a wide range of biomedical language tasks; while [109, 116, 54, 121] adopt knowledge-enhanced visual-language representation learning and demonstrate superior performance in downstream classification tasks. Our method aligns with the representation learning methods. While all existing methods mainly focus on incorporation with domain knowledge in text form, we explore multimodal medical knowledge alignment for both text and anatomical atlas, facilitating fine-grained visual-language knowledge injection while training universal segmentation model.

5 Dataset

Toward building a universal segmentation model for medical imaging, with text as prompts, we collect two types of data in this work: medical domain knowledge to train the text encoder, and medical segmentation data, which includes both images and segmentation masks. In this section, we will describe them sequentially.

5.1 Domain Knowledge

To acquire textual knowledge, we mainly exploit two sources of domain knowledge: the Unified Medical Language System (UMLS)¹, a comprehensive medical knowledge graph consisting of concept definitions and their interrelations; and search engines, which are prompted to organize knowledge into a graph of the same format, specifically refined for the human anatomy corpus. Regarding visual knowledge, we have compiled 72 medical segmentation datasets, creating an atlas that covers over 497 anatomical structures of the human body. All sources of knowledge are systematically categorized, encompassing anatomies and concepts from all regions of the human body. Two examples of these sources are illustrated in Fig. 11 (a) and (b).

¹<https://www.nlm.nih.gov/research/umls>

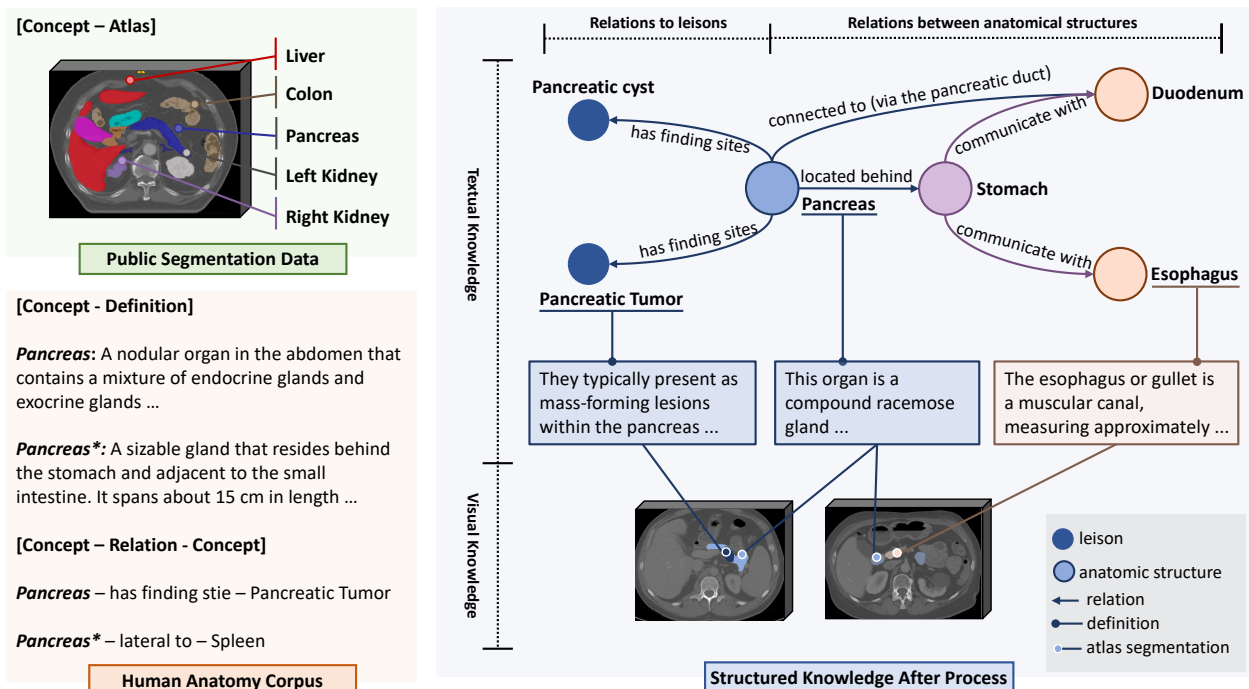


Figure 11 | The medical knowledge used in the visual-language pretraining. (a) Segmentation datasets provide an atlas for extensive anatomy concepts. In this example, atlas segmentation is marked with different colors. (b) Knowledge generated from UMLS and search engines encompasses a broad array of concept-definition pairs and extensive relationships. (c) By integrating all collected knowledge sources, a medical knowledge tree is constructed. All definitions are partially displayed for conciseness. Definition and relation denoted with * are derived from the search engine, otherwise from UMLS.

UMLS. Unified Medical Language System (UMLS) [10] is a knowledge source of biomedical vocabulary developed by the US National Library of Medicine². It integrates a wide range of concepts from more than 60 families of biomedical vocabularies, each equipped with a Concept Unique Identifier (CUI) and definition. It also contains the relations among these concepts. Following [116], we extract 229,435 biomedical terminologies and definitions, as well as 1,048,575 relationship triplets, composing a knowledge graph on these terminologies.

Search engine generated knowledge. Although UMLS is widely acknowledged and adopted as a general medical knowledge corpus [109, 116, 54, 121], it lacks a fine-grained description of anatomy concepts critical for segmentation tasks. For example, for ‘liver’, the definition is ‘A large lobed glandular organ in the abdomen of vertebrates that is responsible for detoxification, metabolism, synthesis, and storage of various substances.’, which erases the morphological features and focuses on functionality. Meanwhile, more comprehensive knowledge on human anatomy may be scattered across various authoritative websites online, *e.g.*, Wikipedia³, ScienceDirect⁴, *etc.*. To harvest such knowledge, we select 6,502 anatomy concepts, and prompt an search engine⁵ to retrieve and summarize definitions for them. We use the following prompt template:

Definition of xxx. Include the location, shape, appearance, structure and spatial relations to other anatomy structures. No need to include functionality. End with ‘END’.

For illustration, the search engine referred to authority websites including Columbiasurgery⁶, Hopkins

²<https://www.nlm.nih.gov>

³<https://www.wikipedia.org>

⁴<https://www.sciencedirect.com/browse/journals-and-books?subject=medicine-and-dentistry>

⁵<https://you.com>

⁶<https://columbiasurgery.org/liver/liver-and-its-functions>

Medicine⁷ and summarized definition for ‘liver’ as: ‘A large organ found in the upper right quadrant of the abdomen, it stands as the largest gland within the human body, with a weight of about 1.5 kilograms. This structure exhibits a reddish-brown hue and is cone or wedge-shaped’. While constructing the knowledge graph, we also adopt GPT4 [2] to extract 38,344 relations between anatomical structures in the generated information-dense definitions with the following prompt:

This is the description of xxx. Please help me find its relations with other anatomical structures in radiological images. Summarize them with the template: Relation: xxx (relational preposition), Anatomical structure: xxx (name of another anatomical structure).
For example, “Relation: situated below, Anatomical structure: xxx”, “Relation: connected to (via xxx), Anatomical structure: xxx”

Visual Atlas. Segmentation datasets naturally provide visual features for anatomy concepts corresponding or complementary to the textual description, such as the texture, spatial location, shape and so on. Details on our collected segmentation datasets are described in Sec. 5.2. Here, we use them as a large-scale and diverse visual atlas library, and link the visual regions to corresponding concepts in textual knowledge graph, bridging the knowledge between visual and language modality.

In summary, by mixing these data, we construct a multimodal medical knowledge tree. As demonstrated in Fig. 11 (c), the concepts (including both anatomical structures and lesions) are linked via the relations and further extended with their definitions, containing their characteristics. Additionally, some are further mapped to the visual atlas, demonstrating their visual features that may hardly be described purely by text.

5.2 Segmentation Dataset

To train our segmentation model with the ability to handle segmentation tasks of different targets, across various modalities and anatomical regions, we collect and integrate 72 diverse publicly available medical segmentation datasets, totaling 22,186 scans including both CT and MRI and 302,033 segmentation annotations spanning 8 different regions of the human body: Brain, Head and Neck, Upper Limb, Thorax, Abdomen, Plevis, and Lower Limb. The dataset is termed as **SAT-DS**. More details are present in Table 13 and Table 14. **Note that**, some public datasets are not mutually exclusive, *e.g.*, KITS23 and KITS21 [35], we thus only collect the latest version, to avoid redundancy and potential data leakage in train-test split.

Before mixing these datasets for training, two challenges remain: (i) the anatomical targets from each dataset must be integrated into a unified annotation system. The clinic demands beneath each dataset collection might be different, resulting in different annotation standards and granularity. Meanwhile, since most datasets are annotated for training specialist models like nnU-Net [38], precise and consistent terminology or expression for anatomical targets is often ignored. Therefore, a unified label system is demanded to avoid potential contradictions when training on mixed datasets. (ii) some critical image statistics, such as intensity distribution and voxel spacing vary from dataset to dataset, hindering the model from learning consistent image representations across datasets. In the following, we present details for dataset integration and pre-processing, and how we address the abovementioned challenges.

Unifying Label System. While integrating different datasets, three procedures are performed to ensure a unified annotation system: (i) we manually check each anatomical target in each dataset and assign a medical term to it, which is guaranteed to be precise and unambiguous across datasets. For instance, the targets that require distinction between orientations, such as the left lung and right lung, are always identified according to the left and right of the human body. And the same anatomical targets from different datasets are named consistently. For example, the i -th lumbar vertebrae in both TotalSegmentator [106] and MRSpineSeg [80] are named with format “lumbar vertebrae i (Li)”; (ii) we adjust the annotations to avoid contradictions between overlapped classes. For example, when lesions are merged into the organs or tissues where they occur, the affected organs and tissues are annotated consistently with the healthy ones; (iii) the same anatomy may have been annotated with different hierarchies in different datasets. In such cases, we manually merge the

⁷<https://www.hopkinsmedicine.org/health/conditions-and-diseases/liver-anatomy-and-functions>

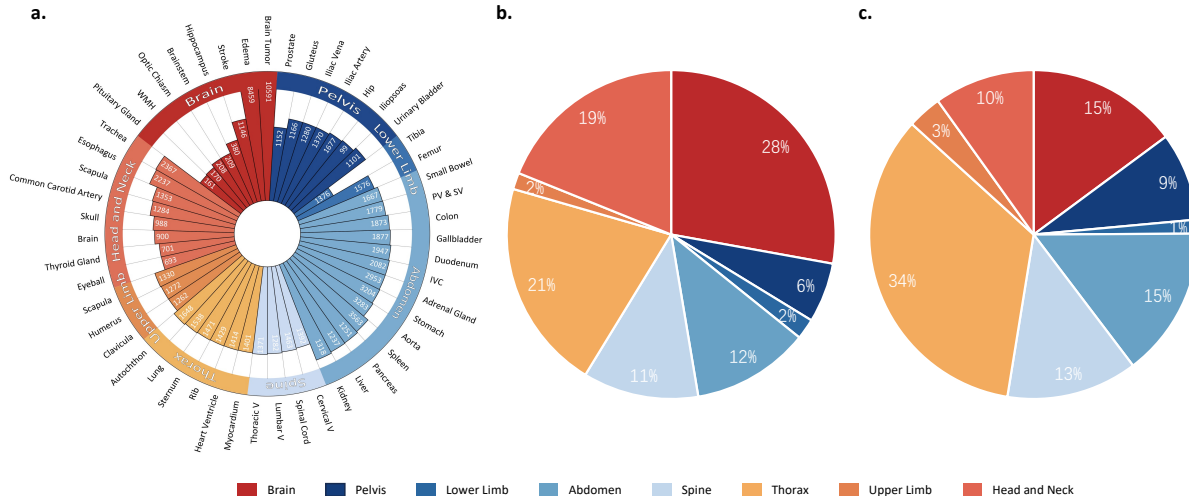


Figure 12 | Statistics of SAT-DS across different anatomical regions. (a) Annotation num of some representative classes in each anatomical region; (b) Number of classes in each anatomical region; (c) Number of annotations in each anatomical region. LC/HC: laryngeal/hypopharyngeal cancer, WHM: white matter hyperintensities, PV&SV: portal vein and splenic vein, IVC: inferior vena cava, Thoracic V: thoracic vertebrae, Cervical V: cervical vertebrae, Lumbar V: lumbar vertebrae.

fine-grained classes to generate additional classes as a complement to close the gap between datasets. For example, sub-regions of liver in Couinaud Liver [98] are merged and added as a new class “liver”. As we will keep collecting datasets to scale up SAT-DS, such a label system will be maintained and updated continuously.

Dataset Pre-processing. As properties of each dataset may greatly impact the training of the segmentation network [38], such as intensity distribution and voxel spacing, we deliberately apply some normalization procedures to all the datasets to ensure uniformity and compatibility between them. *Firstly*, all the images are reoriented to specific axcodes, respaced to a voxel size of $1 \times 1 \times 3 \text{ mm}^2$ and cropped to non-zero region. *Secondly*, we apply different intensity normalization strategies to CT images and MRI images, specifically, for CT images, intensity values are truncated to $[-500, 1000]$ and applied z-score normalization. For MRI images, intensity values are clipped by 0.5% and 99.5% of the image, and then z-score normalized. During training, we randomly crop the image patch with a fixed size of $288 \times 288 \times 96$. Random zoom-in, zoom-out, and intensity scaling are applied for data augmentation.

Dataset Statistics. After integrating datasets, we derive a segmentation data collection that covers 497 segmentation classes, far outpacing each single dataset in both diversity and scale. We divide human body into eight regions, and classify each class into them manually. Fig. 12 (b) and (c) show the distribution of classes and annotations across different human body regions. We further show the distribution of some example classes in each region in Fig. 12 (a). The extensive range of categories and regions lays the foundation for the SAT’s wide application scenarios. The data collection is more than **fourth times** the size of the largest dataset (BraTS2023-GLI) in terms of volume number, and nearly **triple** the most comprehensive dataset (DAP Atlas) in terms of the class number.

Discussion. In the process of building SAT-DS, we merge a wide range of segmentation tasks, and establishing a unified label system by using natural language/text. Generally speaking, there are three advantages to do this: (i) natural language is powerful and discriminative, that enables better differentiation of the medical terminologies in the language embedding space; (ii) as shown in previous work [109, 116, 54, 121], knowledge-enhanced representation learning for the text encoder demonstrates promising performance, allowing to learn the implicit or explicit relationships between these segmentation targets. For example, segmenting a specific lobe of the liver requires the exact segmentation of liver as an organ in abdomen cavity, and shall be facilitated by referring to other parts of the liver. Therefore, establishing such connections via systematic medical knowledge shall be beneficial. (iii) text prompt can be given automatically without any human intervention, for instance, from large language model. This would pave the way for building a universal segmentation

model that can be flexibly integrated into foundation models for generalist medical artificial intelligence, as a powerful grounding tool.

6 Method

Towards building up our universal segmentation model by text prompt, we consider two main stages, namely, multimodal knowledge injection and universal segmentation training. In the following, we start by defining the problem scenario (Sec. 6.1). Then, we show how to structure multimodal medical knowledge and inject it into a text encoder (Sec. 6.2). Lastly, we employ the text encoder to guide our universal segmentation model training on SAT-DS dataset (Sec. 6.3).

6.1 Problem Formulation

Assuming we have a segmentation dataset collection, *i.e.*, $\mathcal{D} = \{(x_1, y_1; T_1), \dots, (x_K, y_K; T_K)\}$, where $x_i \in \mathbb{R}^{H \times W \times D \times C}$ denotes the image scan, $y_i \in \mathbb{R}^{H \times W \times D \times M}$ is the binary segmentation annotations of the anatomical targets in the image, and $T_i = \{t_1, t_2, \dots, t_M\}$ denote the corresponding medical terminology set. The universal segmentation task can be formulated as:

$$\hat{y}_i = \Phi_{\text{SAT}}(\Phi_{\text{visual}}(x_i), \Phi_{\text{text}}(T_i)), \quad (1)$$

where Φ_{visual} is a visual encoder, Φ_{text} is a text encoder, Φ_{SAT} is a universal segmentation model and ideally, x_i can be an image scan from any modality of the anatomical region, T_i can contain any text-wise medical terminology of interest.

6.2 Multimodal Knowledge Injection

Here, we aim to inject rich multimodal medical knowledge into the visual and text encoders. The section starts from the procedure for structuring the multimodal medical knowledge data, and further presents details to use them for visual-language pre-training.

Multimodal Domain Knowledge Construction. As shown in Fig. 13 (a), the data from UMLS, search engine, and segmentation datasets can be aggregated into two formats:

- **Textual medical concept pair.** For text-only knowledge, each concept t_i is associated with a definition p_i , constructing pairs of text $(t_i; p_i)$. We also derive a knowledge graph that connects the medical concepts through abundant triplet relationships (t_i, r_{ij}, t_j) . This graph can be alternatively seen as a specialized text pair, $(t_i + r_{ij}; t_j)$ or $(t_i; r_{ij} + t_j)$, where ‘+’ refers to string concatenation. In this way, we can thus unify the two kinds of textual knowledge.
- **Visual medical concept pair.** To align with the segmentation task, we gather pairs consisting of a concept (can be either an anatomical structure or lesion) and its image atlas. Note that, multiple pairs could be extracted from a single image. These pairs share a similar format to the segmentation data, denoted as $(x_i, y_i; t_i)$, where x_i and t_i are consistent with their definition in Sec. 6.1 and $y_i \in \mathbb{R}^{H \times W \times D \times 1}$ is a binary segmentation mask for t_i .

In summary, all the knowledge can either be represented as pure text description, *e.g.*, $t_i, p_i, t_i + r_{ij}, r_{ij} + t_j$, or atlas segmentation (x_i, y_i) , and paired further.

Visual-Language Pre-training. As shown in Fig. 13 (a), for pure text description, we encode them with a BERT [45] pre-trained on PubMed abstract [52]:

$$z = \Phi_{\text{text}}(\mathbf{t}), \quad \mathbf{t} \in [t_i, p_i, t_i + r_{ij}, r_{ij} + t_j], \quad z \in \mathbb{R}^d, \quad (2)$$

where d refers to the feature dimension. For visual concepts, we adopt the visual encoder Φ_{visual} . Given the excellent robustness and performance of U-Net [38, 92], we apply a standard 3D U-Net encoder to extract

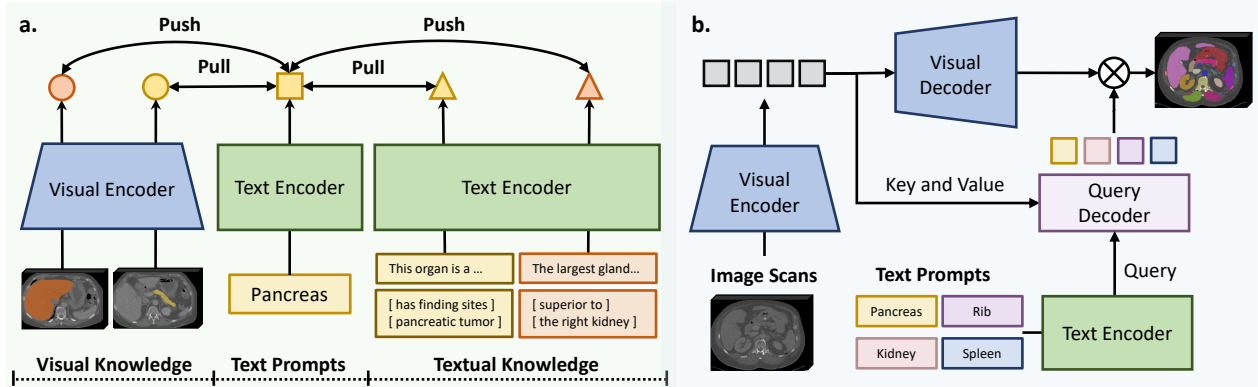


Figure 13 | Overview of SAT. (a) We inject multi-modal medical knowledge into knowledge encoders via contrastive learning. The knowledge is in different formats: atlas segmentation, concepts(terminologies), definitions, and relationships between concepts. We devise visual and text encoder to embed them; (b) We train a universal segmentation network based on the text prompts from the pre-trained text encoder. It is capable of segmenting a wide range of targets for image scans from different modalities and anatomical regions.

multi-scale image embeddings:

$$V_i = \{v_{i1}, v_{i2}, \dots, v_{iS}\} = \Phi_{\text{visual}}(x_i), \quad v_{is} \in \mathbb{R}^{H_s \times W_s \times D_s \times d}, \quad (3)$$

where V_i is the multi-scale feature maps from U-Net encoder layers, and H_s, W_s, D_s, d_s are the spatial resolutions and channel width at different layers. We further average ROI pooling on these feature maps respectively, based on the down-sampled segmentation mask fitting resolutions at different layers. The concatenated pooled features can thus be treated as representation of the anatomical target on this image, containing multi-scale visual clues for it.

$$z = \mathcal{F}_{\text{pooling}}(\Phi_{\text{visual}}(x_i); y_i), \quad z \in \mathbb{R}^d. \quad (4)$$

We train the visual encoder and text encoder by maximizing the similarities between all positive knowledge pairs, linked by text prompts (medical terminology names), as shown in Fig. 13. Specifically, given $(x_i, y_i; t_i), (t_i; p_i), (t_i + r_{ij}; t_j), (t_i; r_{ij} + t_j)$, for simplicity, we denote all the encoded features as z , regardless of their modality format. For a batch of N pairs $\{(z_1, z'_1), \dots, (z_N, z'_N)\}$, we have:

$$\mathcal{L}_{\text{knowledge}} = -\frac{1}{N} \sum_{i=1}^N \left(\log \frac{\exp(z_i \cdot z'_i / \tau)}{\sum_{k=1}^N \mathbb{1}_{i \neq k} \exp(z_i \cdot z'_k / \tau)} + \log \frac{\exp(z_i \cdot z'_i / \tau)}{\sum_{k=1}^N \mathbb{1}_{i \neq k} \exp(z_k \cdot z'_i / \tau)} \right), \quad (5)$$

which is a typical contrastive learning pipeline, with $\tau = 0.07$ as temperature.

Discussion. In general, by maximizing the similarities between positive textual and visual feature pairs, we force the text encoders to construct neural representations for medical concepts from two aspects: (i) through the well-established knowledge graph in text form, the text encoder enables to encode relationships between concepts in the latent space; (ii) the model captures the characteristics of anatomical structures and lesions via both visual atlas segmentations and detailed definitions. Therefore, in contrast to the one-hot labeling that treats each anatomical target as of being independent, such continuous neural representation shall provide more helpful guidance for the segmentation task.

6.3 Universal Segmentation Training

With the pre-trained visual and text encoder, we now continue the procedure for building the universal segmentation model with text as prompts. Fig. 13 (b) demonstrates the overall framework. Specifically, apart

from the pre-trained visual and text encoders, the segmentation model consists of three more components: a visual decoder Φ_{dec} , a query decoder Φ_{query} , and a mask generator.

Although a sample in the segmentation dataset collection $(x_i, y_i; T_i)$ may contain multiple annotations, *i.e.*, $T_i = \{t_1, t_2, \dots, t_M\}$, for simplicity, we describe the segmentation procedure for one structure (t_i) .

Terminology Encoding. We use the pre-trained text encoder to generate neural embedding for one anatomical target as a text prompt for segmentation:

$$z_i = \Phi_{\text{text}}(t_i), z_i \in \mathbb{R}^d. \quad (6)$$

Note that, after pre-training the text encoder with domain knowledge injection, z_i should contain both the textual background information and visual information from atlas samples.

Visual Encoding. We adopt the pre-trained visual encoder as explained in Sec. 6.2, Equa. 3, and continue training it.

Visual Decoding. In the visual decoder, the feature maps from the encoder are gradually upsampled with skip connections, effectively following the U-Net architecture [38, 92], ending up with per-pixel dense feature:

$$u_i = \Phi_{\text{dec}}(V_i), u_i \in \mathbb{R}^{H \times W \times D \times d'}, \quad (7)$$

where d' is the dimension for the per-pixel dense feature after recovering to the original resolution.

Query Decoder. Although a general representation of the anatomical target is derived from the pre-trained text encoder with a text prompt, visual variations may still exist from patient to patient, we thus insert a transformer-based query module to further enhance the text prompts with visual clues. In practice, this module consists of 6 standard transformer decoders [101], that treats text embedding as query, and the pooled multi-scale visual features from the U-Net encoder as key, values, formulated as:

$$q_i = \Phi_{\text{query}}(V_i, z_i), q_i \in \mathbb{R}^d. \quad (8)$$

Where z_i is consistent with z in Equa. 4. Therefore q_i can be seen as an adapted representation of the anatomical target in specific image scan x_i .

Mask Generator. By conducting pixel-wise dot-product between the representation of the anatomical target and the fine-grained per-pixel embedding, we can acquire a per-pixel segmentation:

$$\hat{y}_i = g(q_i) \cdot u_i, \hat{y}_i \in \mathbb{R}^{H \times W \times D}, \quad (9)$$

where $g(\cdot)$ is a feed-forward layer projecting q_i to a consistent dimension with the dense feature map u_i .

Training Objective. Following [38], we adopt a loss function as the sum of binary cross-entropy loss and dice loss. For a sample with M classes and C voxels, we denote $p_{c,m}$ and $s_{c,m}$ the prediction and ground-truth for c -th pixel respectively on class m , the loss is:

$$\mathcal{L} = \underbrace{-\frac{1}{M} \sum_{m=1}^M \frac{1}{C} \sum_{c=1}^C p_{c,m} \cdot \log s_{c,m}}_{\text{Binary Cross Entropy Loss}} + \underbrace{\left(1 - \frac{2 \sum_{i=1}^M \sum_{c=1}^C p_{c,m} \cdot s_{c,m}}{\sum_{m=1}^M \sum_{c=1}^C p_{c,m}^2 + \sum_{m=1}^M \sum_{c=1}^C s_{c,m}^2}\right)}_{\text{Dice Loss}} \quad (10)$$

7 Implement Details

We encounter several challenges in training on the combined large number of heterogeneous medical datasets in 3D format. In this section, we provide details on the adopted training strategies.

Progressive Multimodal Knowledge Injection. For the stability of training, we implement the multimodal knowledge injection procedure introduced in Sec. 6.2 progressively. At the beginning, the text encoder is

pretrained on the text knowledge via contrastive learning, *i.e.*, the textual medical concept pairs. The maximal sequence length after tokenization is 256, for even longer text input, we apply random truncation to fully exploit the knowledge in the long text. After convergence, to align text representations and visual features, we apply contrastive learning between the finetuned text encoder and the visual encoder on the visual medical concept pair.

Pre-processing Segmentation Dataset. We take voxel spacing as $1 \times 1 \times 3 \text{ mm}^2$ and patch size $288 \times 288 \times 96$, based on two empirical considerations: (i) when mixing the various datasets, scans with a wide range of voxel spacings ought to be normalized before processing in the same convolutional network. While resampling to larger voxel spacing may lose information, smaller voxel spacing will generate artifacts; (ii) a larger receptive field generally ensures better segmentation performance for most targets, however, increasing patch size will result in higher computational cost. We strike a balance between them based on the computational resources in use.

Balancing Segmentation Datasets. To balance between all datasets, we set the sampling strategy for each scan based on two intuitions respectively: (i) training case number varies significantly from dataset to dataset, which should be alleviated. We follow [100] and set the sampling weight of all scans in a dataset as the inverse proportion to \sqrt{N} , N is the number of training cases in the dataset; (ii) scans with larger annotation areas or more annotated classes should be sampled more as they are often harder to learn. Thus, we repeat such scans for R times in the sampling pool, where $R = \frac{S_{roi}}{288 \times 288 \times 96} \times \frac{M}{32}$. S_{roi} is size of the annotated area in a image scan, namely, its foreground area; $288 \times 288 \times 96$ is the patch size to crop; c is the number of annotated classes on it; and 32 is the maximal number of text prompts in a batch.

Balancing Segmentation Classes. While cropping the image scan, it’s a common practice [38] to over-sample foreground crops, *i.e.*, crops containing at least one segmentation target. However, weighting these crops evenly may ignore the unbalanced spatial distribution of segmentation targets. For example, in large scans with numerous annotations, tiny targets are harder to sample and thus may be ignored by the model. Thus, in foreground oversampling, we give more weight on regions with more segmentation targets.

Difference between SAT-Pro and SAT-Nano. We devise two variants of SAT with different model sizes in visual backbone. For SAT-Nano, we adopt a U-Net with 6 blocks in-depth, each block has 2 convolutional layers and 3×3 size each kernel. The channel widths for each stage are [64, 64, 128, 256, 512, 768]; SAT-Pro share the same architecture with SAT-Nano, except that each block consists of 3 convolutional layers, and the channel widths are doubled to [128, 128, 256, 512, 1024, 1536].

Other Hyperparameter Details. The query decoder is a 6-layer standard transformer decoder with 8 heads in each attention module. Feature dimensions of a text prompt $d = 768$ and per-pixel embedding $d' = 64$. To unify the features from visual backbone variants with varying channel widths, they are projected to $d = 768$ with different feed-forward layers, and input as key and value to query decoder. For images with multiple segmentation targets, we set the maximal text prompts sampled in a batch of up to 32. A combination of cross-entropy loss and dice loss is applied as supervision at training time. We use AdamW [63] as the optimizer with cosine annealing schedule, maximal $lr = 1 \times 10^{-4}$, 10000 steps for warm-up. The SAT-Nano is trained on 8 NVIDIA A100 GPUs with 80GB memory, using maximal batch size 2; while the SAT-Pro is trained on 16 NVIDIA A100 GPUs with 80GB memory, using maximal batch size 1.

8 Experiment Settings

8.1 Evaluation Datasets

To strike a balance between extensive experiments and computational cost, we utilize two collection of datasets:

- **SAT-DS.** As describe in Sec. 5.2, this contains all the 72 datasets, 497 classes from all human body regions, 22,186 image scans and 302,033 segmentation annotations.
- **SAT-DS-Nano.** A subset of SAT-DS, including only 49 datasets, 13,303 images and 151,461 annotations. Note that SAT-DS-Nano also covers 429 classes from all human body regions, adequate to evaluate universal segmentation task.

The detailed composition of SAT-DS and SAT-DS-Nano can be found in Table 13. As there is no existing benchmark for evaluating the universal segmentation model, we randomly split each dataset into 80% for training and 20% for testing: (i) datasets may share the same images but with different classes. For example, Couinaud Liver provides fine-grained liver segmentation on a subset of MSD Hepatic Vessel. We carefully split the Couinaud Liver to make sure the test set will not be leaked in the train set of MSD Hepatic Vessel; (ii) scans of the same patient but different modalities are treated as different samples during training and evaluation. For example, MSD Prostate contains T2 and ADC scans of each patient. However, they share the same structure on the image. To avoid potential data leaking, we carefully split such datasets by patient id. Note that when involving segmentation datasets in the visual-language pretraining, we only use the training data to avoid potential data leaking. For datasets involved in SAT-DS-Nano, we keep their splits the same as in SAT-DS. **The download link for each datasets can be found in Table 14, and we will release our dataset splits to the research community for model comparison.**

8.2 Baseline

We take nnU-Net [38] as a strong baseline for comparison, which specializes in a series of configurations for each dataset. For a comprehensive evaluation, we train one nnU-Net model on each of the datasets. Note that, following [106], we split Totalsegmentator into 6 subsets and train 6 different nnU-Net models. Similarly, datasets such as CHAOS with both MRI and CT images are treated as two different datasets. When training nnU-Nets on each dataset, we adopt a multi-class segmentation setting and deliver the masks of all categories in this dataset at once. We derive the optimal network architecture and pre-processing pipeline with the default setting of nnU-Net. The detailed network design is shown in Table 11. In summary, we train an assemble of 72 nnU-Nets, that are customized on each dataset and serve as the competitive baseline for evaluation. We adopt the latest official implementation of nnU-Net v2⁸ in practice.

8.3 Evaluation Protocols

Given our goal is to develop a universal medical segmentation model, this provides opportunities to evaluate novel perspectives in addition to the traditional evaluation per dataset. Specifically, we conduct the evaluations from three dimensions:

- **Class-wise Evaluation.** As SAT is capable of segmenting a wide range of anatomical targets across the human body, we merge the results from the same classes across datasets to indicate the performance on each anatomical target. Specifically, we follow macro-average method: for a class annotated in multiple datasets, we first calculate its average scores within each dataset, and then average them over all datasets. Note that, the same anatomical structures or lesions from different modalities are treated as different classes in this work, *e.g.*, liver in both CT and MRI images.
- **Region-wise Evaluation.** In general, anatomical structures from the same human body region are closely connected and more likely to be involved in diagnosis within the same hospital department. Here, we consider the region-wise evaluation: based on class-wise evaluation, we merge results from all classes in the same body region, as to indicate the general performance in this region. For classes existing in multiple regions, we classify them into ‘Whole Body’ category. In addition, we report results for lesions classes independently as a category ‘lesion’, instead of merging them into specific regions.
- **Dataset-wise Evaluation.** Results of the classes within the same dataset are averaged to indicate the performance on this dataset. This is the same as the conventional evaluation protocol of specialist segmentation models trained on a single dataset, **however, we believe this is less valuable for evaluating universal segmentation models.**

8.4 Evaluation Metrics

We quantitatively evaluate the segmentation performance from the perspective of region and boundary metrics [72], *e.g.*, Dice Similarity Coefficient (DSC) and Normalized Surface Distance (NSD) respectively.

DSC. Dice Similarity Coefficient (DSC) is a standard region-based metric for medical image segmentation

⁸<https://github.com/MIC-DKFZ/nnUNet/>

evaluation. It measures the overlap between model’s prediction P and ground truth G , formally defined as:

$$DSC(P, G) = \frac{2|P \cap G|}{|P| + |G|}. \quad (11)$$

NSD. Normalized Surface Distance (NSD) [78] is a boundary-based metric that measures the consistency at the boundary area of the model’s prediction P and ground truth G , which is defined as:

$$NSD(P, G) = \frac{|\partial P \cap B_{\partial G}| + |\partial G \cap B_{\partial P}|}{|\partial P| + |\partial G|}, \quad (12)$$

where $B_{\partial P} = \{x \in \mathbf{R}^3 | \exists \hat{x} \in \partial P, \|x - \hat{x}\| \leq \tau\}$ and $B_{\partial G} = \{x \in \mathbf{R}^3 | \exists \hat{x} \in \partial G, \|x - \hat{x}\| \leq \tau\}$ are the boundary area of model’s prediction and ground truth at a tolerance τ , respectively. We set τ as 1 in the experiments.

9 Conclusion

In this paper, we promote the progress of medical universal segmentation with text as prompt and knowledge enhancement. We build up the largest and most comprehensive 3D medical segmentation dataset, and the first multi-modal knowledge tree for human anatomy. In contrast to existing segmentation models that are limited in 2D input and box/point prompts, our model, **SAT**, enables text-driven universal segmentation on various radiologic modalities across 8 main human body parts, greatly reducing the usage difficulty of medical universal segmentation model in practice. The final solution we proposed, *i.e.*, SAT-Pro, which only contains 447M parameters, while demonstrating comparable performance to 72 specialist nnU-Nets, with around 2.2B parameters trained individually on 72 datasets for segmenting 497 categories. We demonstrate its strong generalization capability to clinic data, as an off-the-shelf automatic segmentation method serving the doctor in analysis and diagnosis. Importantly, we show the potential of SAT as a powerful agent, paving the way to equip large language models with grounding capability.

References

- [1] The 2023 kidney and kidney tumor segmentation challenge (kits23). <https://kits-challenge.org/kits23/>, 2023. Accessed: 2024-04-07.
- [2] OpenAI (2023). Gpt-4 technical report, 2023.
- [3] Maruf Adewole, Jeffrey D. Rudie, Anu Gbadamosi, Oluyemisi Toyobo, Confidence Raymond, Dong Zhang, Olubukola Omidiji, Rachel Akinola, Mohammad Abba Suwaid, Adaobi Emegoakor, Nancy Ojo, Kenneth Aguh, Chinasa Kalaiwo, Gabriel Babatunde, Afolabi Ogunleye, Yewande Gbadamosi, Kator Iorpagher, Evan Calabrese, Mariam Aboian, Marius Linguraru, Jake Albrecht, Benedikt Wiestler, Florian Kofler, Anastasia Janas, Dominic LaBella, Anahita Fathi Kzerooni, Hongwei Bran Li, Juan Eugenio Iglesias, Keyvan Farahani, James Eddy, Timothy Bergquist, Verena Chung, Russell Takeshi Shinohara, Walter Wiggins, Zachary Reitman, Chunhao Wang, Xinyang Liu, Zhifan Jiang, Ariana Familiar, Koen Van Leemput, Christina Bukas, Maire Piraud, Gian-Marco Conte, Elaine Johansson, Zeke Meier, Bjoern H Menze, Ujjwal Baid, Spyridon Bakas, Farouk Dako, Abiodun Fatade, and Udunna C Anazodo. The brain tumor segmentation (brats) challenge 2023: Glioma segmentation in sub-saharan africa patient population (brats-africa), 2023.
- [4] V. Andrearczyk, V. Oreiller, M. Hatt, and A. Depeursinge. Overview of the hecktor challenge at miccai 2022: Automatic head and neck tumor segmentation and outcome prediction in pet/ct. In V. Andrearczyk, V. Oreiller, M. Hatt, and A. Depeursinge, editors, *Head and Neck Tumor Segmentation and Outcome Prediction. HECKTOR 2022. Lecture Notes in Computer Science*, volume 13626. Springer, Cham, 2023.
- [5] Michela Antonelli, Annika Reinke, Spyridon Bakas, Keyvan Farahani, Annette Kopp-Schneider, Bennett A Landman, Geert Litjens, Bjoern Menze, Olaf Ronneberger, Ronald M Summers, et al. The medical segmentation decathlon. *Nature communications*, 13(1):4128, 2022.
- [6] Itzik Avital, Ilya Nelkenbaum, Galia Tsarfaty, Eli Konen, Nahum Kiryati, and Arnaldo Mayer. Neural segmentation of seeding rois (srois) for pre-surgical brain tractography. *IEEE Transactions on Medical Imaging*, 39(5):1655–1667, 2019.
- [7] Ujjwal Baid, Satyam Ghodasara, Suyash Mohan, Michel Bilello, Evan Calabrese, Errol Colak, Keyvan Farahani, Jayashree Kalpathy-Cramer, Felipe C Kitamura, Sarthak Pati, et al. The rsna-asnr-miccai brats 2021 benchmark on brain tumor segmentation and radiogenomic classification. *arXiv preprint arXiv:2107.02314*, 2021.
- [8] Shaimaa Bakr, Olivier Gevaert, Sebastian Echegaray, Kelsey Ayers, Mu Zhou, Majid Shafiq, Hong Zheng, Jalen Anthony Benson, Weiruo Zhang, Ann NC Leung, et al. A radiogenomic dataset of non-small cell lung cancer. *Scientific Data*, 5(1):1–9, 2018.
- [9] Olivier Bernard, Alain Lalonde, Clement Zotti, Frederick Cervenansky, Xin Yang, Pheng-Ann Heng, Irem Cetin, Karim Lekadir, Oscar Camara, Miguel Angel Gonzalez Ballester, et al. Deep learning techniques for automatic mri cardiac multi-structures segmentation and diagnosis: is the problem solved? *IEEE Transactions on Medical Imaging*, 37(11):2514–2525, 2018.
- [10] Olivier Bodenreider. The unified medical language system (umls): integrating biomedical terminology. *Nucleic acids research*, 32(suppl_1):D267–D270, 2004.
- [11] Victor Ion Butoi, Jose Javier Gonzalez Ortiz, Tianyu Ma, Mert R Sabuncu, John Guttag, and Adrian V Dalca. Universeg: Universal medical image segmentation. *arXiv preprint arXiv:2304.06131*, 2023.
- [12] Hu Cao, Yueyue Wang, Joy Chen, Dongsheng Jiang, Xiaopeng Zhang, Qi Tian, and Manning Wang. Swin-unet: Unet-like pure transformer for medical image segmentation. In *European Conference on Computer Vision*, pages 205–218. Springer, 2022.
- [13] Cheng Chen, Qi Dou, Hao Chen, Jing Qin, and Pheng Ann Heng. Unsupervised bidirectional cross-modality adaptation via deeply synergistic image and feature alignment for medical image segmentation. *IEEE Transactions on Medical Imaging*, 39(7):2494–2505, 2020.
- [14] Jieneng Chen, Jieru Mei, Xianhang Li, Yongyi Lu, Qihang Yu, Qingyue Wei, Xiangde Luo, Yutong Xie, Ehsan Adeli, Yan Wang, et al. 3d transunet: Advancing medical image segmentation through vision transformers. *arXiv preprint arXiv:2310.07781*, 2023.

- [15] Junlong Cheng, Jin Ye, Zhongying Deng, Jianpin Chen, Tianbin Li, Haoyu Wang, Yanzhou Su, Ziyang Huang, Jilong Chen, Lei Jiang, et al. Sam-med2d. *arXiv preprint arXiv:2308.16184*, 2023.
- [16] Özgün Çiçek, Ahmed Abdulkadir, Soeren S Lienkamp, Thomas Brox, and Olaf Ronneberger. 3d u-net: learning dense volumetric segmentation from sparse annotation. In *Medical Image Computing and Computer-Assisted Intervention (MICCAI)*, pages 424–432. Springer, 2016.
- [17] Marco Cipriano, Stefano Allegretti, Federico Bolelli, Mattia Di Bartolomeo, Federico Pollastri, Arrigo Pellacani, Paolo Minafra, Alexandre Anesi, and Costantino Grana. Deep segmentation of the mandibular canal: a new 3d annotated dataset of cbct volumes. *IEEE Access*, 10:11500–11510, 2022.
- [18] Hui Cui, Yiyue Xu, Wanlong Li, Linlin Wang, and Henry Duh. Collaborative learning of cross-channel clinical attention for radiotherapy-related esophageal fistula prediction from ct. In *Medical Image Computing and Computer-Assisted Intervention (MICCAI)*, pages 212–220. Springer, 2020.
- [19] Jiahua Dong, Yang Cong, Gan Sun, Bineng Zhong, and Xiaowei Xu. What can be transferred: Unsupervised domain adaptation for endoscopic lesions segmentation. In *Proceedings of the IEEE/CVF Conference on Computer Vision and Pattern Recognition*, pages 4023–4032, 2020.
- [20] Reuben Dorent, Aaron Kujawa, Marina Ivory, Spyridon Bakas, Nicola Rieke, Samuel Joutard, Ben Glocker, Jorge Cardoso, Marc Modat, Kayhan Batmanghelich, Arseniy Belkov, Maria Baldeon Calisto, Jae Won Choi, Benoit M. Dawant, Hexin Dong, Sergio Escalera, Yubo Fan, Lasse Hansen, Mattias P. Heinrich, Smriti Joshi, Victoriya Kashtanova, Hyeon Gyu Kim, Satoshi Kondo, Christian N. Kruse, Susana K. Lai-Yuen, Hao Li, Han Liu, Bunheng Ly, Ipek Oguz, Hyungseob Shin, Boris Shirokikh, Zixian Su, Guotai Wang, Jianghao Wu, Yanwu Xu, Kai Yao, Li Zhang, Sébastien Ourselin, Jonathan Shapey, and Tom Vercauteren. Crossmoda 2021 challenge: Benchmark of cross-modality domain adaptation techniques for vestibular schwannoma and cochlea segmentation. *Medical Image Analysis*, 83:102628, 2023.
- [21] Qi Dou, Lequan Yu, Hao Chen, Yueming Jin, Xin Yang, Jing Qin, and Pheng-Ann Heng. 3d deeply supervised network for automated segmentation of volumetric medical images. *Medical Image Analysis*, 41:40–54, 2017.
- [22] Yuxin Du, Fan Bai, Tiejun Huang, and Bo Zhao. Segvol: Universal and interactive volumetric medical image segmentation. *arXiv preprint arXiv:2311.13385*, 2023.
- [23] Leyuan Fang, Chong Wang, Shutao Li, Hossein Rabbani, Xiangdong Chen, and Zhimin Liu. Attention to lesion: Lesion-aware convolutional neural network for retinal optical coherence tomography image classification. *IEEE Transactions on Medical Imaging*, 38(8):1959–1970, 2019.
- [24] Xi Fang and Pingkun Yan. Multi-organ segmentation over partially labeled datasets with multi-scale feature abstraction. *IEEE Transactions on Medical Imaging*, 39(11):3619–3629, 2020.
- [25] Sergios Gatidis, Tobias Hepp, Marcel Früh, Christian La Fougère, Konstantin Nikolaou, Christina Pfannenbergl, Bernhard Schölkopf, Thomas Küstner, Clemens Cyran, and Daniel Rubin. A whole-body fdg-pet/ct dataset with manually annotated tumor lesions. *Scientific Data*, 9(1):601, 2022.
- [26] Eli Gibson, Francesco Giganti, Yipeng Hu, Ester Bonmati, Steve Bandula, Kurinchi Gurusamy, Brian Davidson, Stephen P Pereira, Matthew J Clarkson, and Dean C Barratt. Automatic multi-organ segmentation on abdominal ct with dense v-networks. *IEEE Transactions on Medical Imaging*, 37(8):1822–1834, 2018.
- [27] Shizhan Gong, Yuan Zhong, Wenao Ma, Jimpeng Li, Zhao Wang, Jingyang Zhang, Pheng-Ann Heng, and Qi Dou. 3dsam-adapter: Holistic adaptation of sam from 2d to 3d for promptable medical image segmentation. *arXiv preprint arXiv:2306.13465*, 2023.
- [28] Ivan Gonzalez-Diaz. Dermaknet: Incorporating the knowledge of dermatologists to convolutional neural networks for skin lesion diagnosis. *IEEE journal of biomedical and health informatics*, 23(2):547–559, 2018.
- [29] Albert Gu and Tri Dao. Mamba: Linear-time sequence modeling with selective state spaces. *arXiv preprint arXiv:2312.00752*, 2023.
- [30] Ali Hatamizadeh, Vishwesh Nath, Yucheng Tang, Dong Yang, Holger R Roth, and Daguang Xu. Swin unetr: Swin transformers for semantic segmentation of brain tumors in mri images. In *International MICCAI Brainlesion Workshop*, pages 272–284. Springer, 2021.

- [31] Ali Hatamizadeh, Vishwesh Nath, Yucheng Tang, Dong Yang, Holger R Roth, and Daguang Xu. Swin unetr: Swin transformers for semantic segmentation of brain tumors in mri images. In *International MICCAI Brainlesion Workshop*, pages 272–284. Springer, 2021.
- [32] Ali Hatamizadeh, Yucheng Tang, Vishwesh Nath, Dong Yang, Andriy Myronenko, Bennett Landman, Holger R Roth, and Daguang Xu. Unetr: Transformers for 3d medical image segmentation. In *Proceedings of the IEEE/CVF Winter Conference on Applications of Computer Vision*, pages 574–584, 2022.
- [33] Yuting He, Guanyu Yang, Jian Yang, Rongjun Ge, Youyong Kong, Xiaomei Zhu, Shaobo Zhang, Pengfei Shao, Huazhong Shu, Jean-Louis Dillenseger, et al. Meta grayscale adaptive network for 3d integrated renal structures segmentation. *Medical image analysis*, 71:102055, 2021.
- [34] Tobias Heimann, Bram Van Ginneken, Martin A Styner, Yulia Arzhaeva, Volker Aurich, Christian Bauer, Andreas Beck, Christoph Becker, Reinhard Beichel, György Bekes, et al. Comparison and evaluation of methods for liver segmentation from ct datasets. *IEEE Transactions on Medical Imaging*, 28(8):1251–1265, 2009.
- [35] Nicholas Heller, Fabian Isensee, Dasha Trofimova, Resha Tejpaul, Zhongchen Zhao, Huai Chen, Lisheng Wang, Alex Golts, Daniel Khapun, Daniel Shats, et al. The kits21 challenge: Automatic segmentation of kidneys, renal tumors, and renal cysts in corticomedullary-phase ct. *arXiv preprint arXiv:2307.01984*, 2023.
- [36] Moritz R Hernandez Petzsche, Ezequiel de la Rosa, Uta Hanning, Roland Wiest, Waldo Valenzuela, Mauricio Reyes, Maria Meyer, Sook-Lei Liew, Florian Kofler, Ivan Ezhov, et al. Isles 2022: A multi-center magnetic resonance imaging stroke lesion segmentation dataset. *Scientific data*, 9(1):762, 2022.
- [37] Yuhao Huang, Xin Yang, Lian Liu, Han Zhou, Ao Chang, Xinrui Zhou, Rusi Chen, Junxuan Yu, Jiongquan Chen, Chaoyu Chen, et al. Segment anything model for medical images? *arXiv preprint arXiv:2304.14660*, 2023.
- [38] Fabian Isensee, Paul F Jaeger, Simon AA Kohl, Jens Petersen, and Klaus H Maier-Hein. nnu-net: a self-configuring method for deep learning-based biomedical image segmentation. *Nature Methods*, 18(2):203–211, 2021.
- [39] Alexander Jaus, Constantin Seibold, Kelsey Hermann, Alexandra Walter, Kristina Giske, Johannes Haubold, Jens Kleesiek, and Rainer Stiefelhagen. Towards unifying anatomy segmentation: automated generation of a full-body ct dataset via knowledge aggregation and anatomical guidelines. *arXiv preprint arXiv:2307.13375*, 2023.
- [40] Yuanfeng Ji, Haotian Bai, Jie Yang, Chongjian Ge, Ye Zhu, Ruimao Zhang, Zhen Li, Lingyan Zhang, Wanling Ma, Xiang Wan, et al. Amos: A large-scale abdominal multi-organ benchmark for versatile medical image segmentation. *arXiv preprint arXiv:2206.08023*, 2022.
- [41] Zhanghexuan Ji, Dazhou Guo, Puyang Wang, Ke Yan, Le Lu, Minfeng Xu, Qifeng Wang, Jia Ge, Mingchen Gao, Xianghua Ye, et al. Continual segment: Towards a single, unified and non-forgetting continual segmentation model of 143 whole-body organs in ct scans. In *Proceedings of the IEEE/CVF International Conference on Computer Vision*, pages 21140–21151, 2023.
- [42] Qiao Jin, Won Kim, Qingyu Chen, Donald C Comeau, Lana Yeganova, W John Wilbur, and Zhiyong Lu. Medcpt: Contrastive pre-trained transformers with large-scale pubmed search logs for zero-shot biomedical information retrieval. *Bioinformatics*, 39(11):btad651, 2023.
- [43] A Emre Kavur, N Sinem Gezer, Mustafa Barış, Sinem Aslan, Pierre-Henri Conze, Vladimir Groza, Duc Duy Pham, Soumick Chatterjee, Philipp Ernst, Savaş Özkan, et al. Chaos challenge-combined (ct-mr) healthy abdominal organ segmentation. *Medical Image Analysis*, 69:101950, 2021.
- [44] Anahita Fathi Kazerooni, Nastaran Khalili, Xinyang Liu, Debanjan Haldar, Zhifan Jiang, Syed Muhammed Anwar, Jake Albrecht, Maruf Adewole, Uduinna Anazodo, Hannah Anderson, Sina Bagheri, Ujjwal Baid, Timothy Bergquist, Austin J. Borja, Evan Calabrese, Verena Chung, Gian-Marco Conte, Farouk Dako, James Eddy, Ivan Ezhov, Ariana Familiar, Keyvan Farahani, Shuvanjan Haldar, Juan Eugenio Iglesias, Anastasia Janas, Elaine Johansen, Blaise V Jones, Florian Kofler, Dominic LaBella, Hollie Anne Lai, Koen Van Leemput, Hongwei Bran Li, Nazanin Maleki, Aaron S McAllister, Zeke Meier, Bjoern Menze, Ahmed W Moawad, Khanak K Nandolia, Julija Pavaine, Marie Piraud, Tina Poussaint, Sanjay P Prabhu, Zachary Reitman, Andres Rodriguez, Jeffrey D Rudie, Ibraheem Salman

- Shaikh, Lubdha M. Shah, Nakul Sheth, Russel Taki Shinohara, Wenxin Tu, Karthik Viswanathan, Chunhao Wang, Jeffrey B Ware, Benedikt Wiestler, Walter Wiggins, Anna Zapaishchykova, Mariam Aboian, Miriam Bornhorst, Peter de Blank, Michelle Deutsch, Maryam Fouladi, Lindsey Hoffman, Benjamin Kann, Margot Lazow, Leonie Mikael, Ali Nabavizadeh, Roger Packer, Adam Resnick, Brian Rood, Arastoo Vossough, Spyridon Bakas, and Marius George Linguraru. The brain tumor segmentation (brats) challenge 2023: Focus on pediatrics (cbtbn-connect-dipgr-asnr-miccai brats-peds), 2023.
- [45] Jacob Devlin Ming-Wei Chang Kenton and Lee Kristina Toutanova. Bert: Pre-training of deep bidirectional transformers for language understanding. In *Proceedings of Annual Conference of the North American Chapter of the Association for Computational Linguistics: Human Language Technologies (NAACL-HLT)*, pages 4171–4186, 2019.
- [46] Alexander Kirillov, Eric Mintun, Nikhila Ravi, Hanzi Mao, Chloe Rolland, Laura Gustafson, Tete Xiao, Spencer Whitehead, Alexander C Berg, Wan-Yen Lo, et al. Segment anything. *arXiv preprint arXiv:2304.02643*, 2023.
- [47] Hugo J Kuijff, J Matthijs Biesbroek, Jeroen De Bresser, Rutger Heinen, Simon Andermatt, Mariana Bento, Matt Berseth, Mikhail Belyaev, M Jorge Cardoso, Adria Casamitjana, et al. Standardized assessment of automatic segmentation of white matter hyperintensities and results of the wmh segmentation challenge. *IEEE Transactions on Medical Imaging*, 38(11):2556–2568, 2019.
- [48] Dominic LaBella, Maruf Adewole, Michelle Alonso-Basanta, Talissa Altes, Syed Muhammad Anwar, Ujjwal Baid, Timothy Bergquist, Radhika Bhalerao, Sully Chen, Verena Chung, Gian-Marco Conte, Farouk Dako, James Eddy, Ivan Ezhov, Devon Godfrey, Fathi Hilal, Ariana Familiar, Keyvan Farahani, Juan Eugenio Iglesias, Zhifan Jiang, Elaine Johanson, Anahita Fathi Kazerooni, Collin Kent, John Kirkpatrick, Florian Kofler, Koen Van Leemput, Hongwei Bran Li, Xinyang Liu, Aria Mahtabfar, Shan McBurney-Lin, Ryan McLean, Zeke Meier, Ahmed W Moawad, John Mongan, Pierre Nedelec, Maxence Pajot, Marie Piraud, Arif Rashid, Zachary Reitman, Russell Takeshi Shinohara, Yury Velichko, Chunhao Wang, Pranav Warman, Walter Wiggins, Mariam Aboian, Jake Albrecht, Udunna Anazodo, Spyridon Bakas, Adam Flanders, Anastasia Janas, Goldey Khanna, Marius George Linguraru, Bjoern Menze, Ayman Nada, Andreas M Rauschecker, Jeff Rudie, Nourel Hoda Tahon, Javier Villanueva-Meyer, Benedikt Wiestler, and Evan Calabrese. The asnr-miccai brain tumor segmentation (brats) challenge 2023: Intracranial meningioma, 2023.
- [49] Zoé Lambert, Caroline Petitjean, Bernard Dubray, and Su Kuan. Segthor: Segmentation of thoracic organs at risk in ct images. In *2020 Tenth International Conference on Image Processing Theory, Tools and Applications (IPTA)*, pages 1–6. IEEE, 2020.
- [50] Bennett Landman, Zhoubing Xu, J Igelsias, Martin Styner, T Langerak, and Arno Klein. Miccai multi-atlas labeling beyond the cranial vault—workshop and challenge. In *Proc. MICCAI Multi-Atlas Labeling Beyond Cranial Vault—Workshop Challenge*, volume 5, page 12, 2015.
- [51] Bennett Landman, Zhoubing Xu, J Igelsias, Martin Styner, T Langerak, and Arno Klein. Miccai multi-atlas labeling beyond the cranial vault—workshop and challenge. In *Proc. MICCAI Multi-Atlas Labeling Beyond Cranial Vault—Workshop Challenge*, volume 5, page 12, 2015.
- [52] Jinhyuk Lee, Wonjin Yoon, Sungdong Kim, Donghyeon Kim, Sunkyu Kim, Chan Ho So, and Jaewoo Kang. Biobert: a pre-trained biomedical language representation model for biomedical text mining. *Bioinformatics*, 36(4):1234–1240, 2020.
- [53] Soochahn Lee, Hackjoon Shim, Sang Hyun Park, Il Dong Yun, and Sang Uk Lee. Learning local shape and appearance for segmentation of knee cartilage in 3d mri. In *Medical Image Computing and Computer Assisted Intervention (MICCAI)*, pages 231–240, 2010.
- [54] Jiayu Lei, Lisong Dai, Haoyun Jiang, Chaoyi Wu, Xiaoman Zhang, Yao Zhang, Jiangchao Yao, Weidi Xie, Yanyong Zhang, Yuehua Li, Ya Zhang, and Yanfeng Wang. Unibrain: Universal brain mri diagnosis with hierarchical knowledge-enhanced pre-training. *arXiv preprint arXiv:2309.06828*, 2023.
- [55] Liu Li, Mai Xu, Xiaofei Wang, Lai Jiang, and Hanruo Liu. Attention based glaucoma detection: A large-scale database and cnn model. In *Proceedings of the IEEE/CVF Conference on Computer Vision and Pattern Recognition*, pages 10571–10580, 2019.

- [56] Lei Li, Veronika A Zimmer, Julia A Schnabel, and Xiahai Zhuang. Atrialjsqnet: a new framework for joint segmentation and quantification of left atrium and scars incorporating spatial and shape information. *Medical image analysis*, 76:102303, 2022.
- [57] Xiaomeng Li, Hao Chen, Xiaojuan Qi, Qi Dou, Chi-Wing Fu, and Pheng-Ann Heng. H-denseunet: hybrid densely connected unet for liver and tumor segmentation from ct volumes. *IEEE Transactions on Medical Imaging*, 37(12):2663–2674, 2018.
- [58] Xiangyu Li, Gongning Luo, Kuanquan Wang, Hongyu Wang, Jun Liu, Xinjie Liang, Jie Jiang, Zhenghao Song, Chunyue Zheng, Haokai Chi, et al. The state-of-the-art 3d anisotropic intracranial hemorrhage segmentation on non-contrast head ct: The instance challenge. *arXiv preprint arXiv:2301.03281*, 2023.
- [59] Sook-Lei Liew, Bethany P Lo, Miranda R Donnelly, Artemis Zavalangos-Petropulu, Jessica N Jeong, Giuseppe Barisano, Alexandre Hutton, Julia P Simon, Julia M Juliano, Anisha Suri, et al. A large, curated, open-source stroke neuroimaging dataset to improve lesion segmentation algorithms. *Scientific data*, 9(1):320, 2022.
- [60] Geert Litjens, Robert Toth, Wendy Van De Ven, Caroline Hoeks, Sjoerd Kerkstra, Bram Van Ginneken, Graham Vincent, Gwenael Guillard, Neil Birbeck, Jindang Zhang, et al. Evaluation of prostate segmentation algorithms for mri: the promise12 challenge. *Medical Image Analysis*, 18(2):359–373, 2014.
- [61] Jie Liu, Yixiao Zhang, Jie-Neng Chen, Junfei Xiao, Yongyi Lu, Bennett A Landman, Yixuan Yuan, Alan Yuille, Yucheng Tang, and Zongwei Zhou. Clip-driven universal model for organ segmentation and tumor detection. In *Proceedings of the IEEE/CVF International Conference on Computer Vision*, pages 21152–21164, 2023.
- [62] Pengbo Liu, Hu Han, Yuanqi Du, Heqin Zhu, Yinhao Li, Feng Gu, Honghu Xiao, Jun Li, Chungpeng Zhao, Li Xiao, Xinbao Wu, and S. Kevin Zhou. Deep learning to segment pelvic bones: large-scale ct datasets and baseline models. *International Journal of Computer Assisted Radiology and Surgery*, 16(5):749, 2021.
- [63] Ilya Loshchilov and Frank Hutter. Decoupled weight decay regularization. In *International Conference on Learning Representations*, 2018.
- [64] Gongning Luo, Kuanquan Wang, Jun Liu, Shuo Li, Xinjie Liang, Xiangyu Li, Shaowei Gan, Wei Wang, Suyu Dong, Wenyi Wang, et al. Efficient automatic segmentation for multi-level pulmonary arteries: The parse challenge. *arXiv preprint arXiv:2304.03708*, 2023.
- [65] Xiangde Luo, Jia Fu, Yunxin Zhong, Shuolin Liu, Bing Han, Mehdi Astaraki, Simone Bendazzoli, Iuliana Toma-Dasu, Yiwen Ye, Ziyang Chen, et al. Segrap2023: A benchmark of organs-at-risk and gross tumor volume segmentation for radiotherapy planning of nasopharyngeal carcinoma. *arXiv preprint arXiv:2312.09576*, 2023.
- [66] X Luo, W Liao, J Xiao, J Chen, T Song, X Zhang, K Li, DN Metaxas, G Wang, and S Zhang. Word: A large scale dataset, benchmark and clinical applicable study for abdominal organ segmentation from ct image. *Medical Image Analysis*, 82:102642–102642, 2022.
- [67] Jun Ma, Feifei Li, and Bo Wang. U-mamba: Enhancing long-range dependency for biomedical image segmentation. *arXiv preprint arXiv:2401.04722*, 2024.
- [68] Jun Ma and Bo Wang. Segment anything in medical images. *arXiv preprint arXiv:2304.12306*, 2023.
- [69] Jun Ma, Yixin Wang, Xingle An, Cheng Ge, Ziqi Yu, Jianan Chen, Qiongjie Zhu, Guoqiang Dong, Jian He, Zhiqiang He, et al. Toward data-efficient learning: A benchmark for covid-19 ct lung and infection segmentation. *Medical physics*, 48(3):1197–1210, 2021.
- [70] Jun Ma, Yao Zhang, Song Gu, Cheng Ge, Shihao Ma, Adamo Young, Cheng Zhu, Kangkang Meng, Xin Yang, Ziyang Huang, Fan Zhang, Wentao Liu, Yuanke Pan, Shoujin Huang, Jiacheng Wang, Mingze Sun, Weixin Xu, Dengqiang Jia, Jae Won Choi, Natália Alves, Bram de Wilde, Gregor Koehler, Yajun Wu, Manuel Wieserfarth, Qiongjie Zhu, Guoqiang Dong, Jian He, the FLARE Challenge Consortium, and Bo Wang. Unleashing the strengths of unlabeled data in pan-cancer abdominal organ quantification: the flare22 challenge. *arXiv preprint arXiv:2308.05862*, 2023.
- [71] Jun Ma, Yao Zhang, Song Gu, Cheng Zhu, Cheng Ge, Yichi Zhang, Xingle An, Congcong Wang, Qiyuan Wang, Xin Liu, et al. Abdomenct-1k: Is abdominal organ segmentation a solved problem? *IEEE Transactions on Pattern Analysis and Machine Intelligence*, 44(10):6695–6714, 2021.

- [72] Lena Maier-Hein, Bjoern Menze, et al. Metrics reloaded: Pitfalls and recommendations for image analysis validation. *arXiv.org*, (2206.01653), 2022.
- [73] Mojtaba Masoudi, Hamid-Reza Pourreza, Mahdi Saadatmand-Tarzjan, Noushin Eftekhari, Fateme Shafiee Zargar, and Masoud Pezeshki Rad. A new dataset of computed-tomography angiography images for computer-aided detection of pulmonary embolism. *Scientific Data*, 5, 2018.
- [74] Bjoern H Menze, Andras Jakab, Stefan Bauer, Jayashree Kalpathy-Cramer, Keyvan Farahani, Justin Kirby, Yuliya Burren, Nicole Porz, Johannes Slotboom, Roland Wiest, et al. The multimodal brain tumor image segmentation benchmark (brats). *IEEE transactions on medical imaging*, 34(10):1993–2024, 2014.
- [75] Fausto Milletari, Nassir Navab, and Seyed-Ahmad Ahmadi. V-net: Fully convolutional neural networks for volumetric medical image segmentation. In *International Conference on 3D Vision (3DV)*, pages 565–571. Ieee, 2016.
- [76] Ahmed W. Moawad, Anastasia Janas, Ujjwal Baid, Divya Ramakrishnan, Leon Jekel, Kiril Krantchev, Harrison Moy, Rachit Saluja, Klara Osenberg, Klara Wilms, Manpreet Kaur, Arman Avesta, Gabriel Cassinelli Pedersen, Nazanin Maleki, Mahdi Salimi, Sarah Merkaç, Marc von Reppert, Niklas Tillmans, Jan Lost, Khaled Bousabarah, Wolfgang Holler, MingDe Lin, Malte Westerhoff, Ryan Maresca, Katherine E. Link, Nourel hoda Tahon, Daniel Marcus, Aristeidis Sotiras, Pamela LaMontagne, Strajit Chakrabarty, Oleg Teytelboym, Ayda Youssef, Ayaman Nada, Yuri S. Velichko, Nicolo Gennaro, Connectome Students, Group of Annotators, Justin Cramer, Derek R. Johnson, Benjamin Y. M. Kwan, Boyan Petrovic, Satya N. Patro, Lei Wu, Tiffany So, Gerry Thompson, Anthony Kam, Gloria Guzman Perez-Carrillo, Neil Lall, Group of Approvers, Jake Albrecht, Udunna Anazodo, Marius George Lingaru, Bjoern H Menze, Benedikt Wiestler, Maruf Adewole, Syed Muhammad Anwar, Dominic Labella, Hongwei Bran Li, Juan Eugenio Iglesias, Keyvan Farahani, James Eddy, Timothy Bergquist, Verena Chung, Russel Takeshi Shinohara, Farouk Dako, Walter Wiggins, Zachary Reitman, Chunhao Wang, Xinyang Liu, Zhifan Jiang, Koen Van Leemput, Marie Piraud, Ivan Ezhov, Elaine Johanson, Zeke Meier, Ariana Familiar, Anahita Fathi Kazerooni, Florian Kofler, Evan Calabrese, Sanjay Aneja, Veronica Chiang, Ichiro Ikuta, Umber Shafique, Fatima Memon, Gian Marco Conte, Spyridon Bakas, Jeffrey Rudie, and Mariam Aboian. The brain tumor segmentation (brats-mets) challenge 2023: Brain metastasis segmentation on pre-treatment mri, 2023.
- [77] Michael Moor, Oishi Banerjee, Zahra Shakeri Hossein Abad, Harlan M Krumholz, Jure Leskovec, Eric J Topol, and Pranav Rajpurkar. Foundation models for generalist medical artificial intelligence. *Nature*, 616(7956):259–265, 2023.
- [78] Stanislav Nikolov, Sam Blackwell, Alexei Zverovitch, Ruheena Mendes, and et al. Clinically applicable segmentation of head and neck anatomy for radiotherapy: deep learning algorithm development and validation study. *Journal of Medical Internet Research*, 23(7):e26151, 2021.
- [79] Saman Nouranian, Mahdi Ramezani, Ingrid Spadinger, William J Morris, Septimu E Salcudean, and Purang Abolmaesumi. Learning-based multi-label segmentation of transrectal ultrasound images for prostate brachytherapy. *IEEE transactions on medical imaging*, 35(3):921–932, 2015.
- [80] Shumao Pang, Chunlan Pang, Lei Zhao, Yangfan Chen, Zhihai Su, Yujia Zhou, Meiyuan Huang, Wei Yang, Hai Lu, and Qianjin Feng. Spineparsenet: spine parsing for volumetric mr image by a two-stage segmentation framework with semantic image representation. *IEEE Transactions on Medical Imaging*, 40(1):262–273, 2020.
- [81] Kelly Payette, Priscille de Dumast, Hamza Kebiri, Ivan Ezhov, Johannes C Paetzold, Suprosanna Shit, Asim Iqbal, Romesa Khan, Raimund Kottke, Patrice Grethen, et al. An automatic multi-tissue human fetal brain segmentation benchmark using the fetal tissue annotation dataset. *Scientific data*, 8(1):167, 2021.
- [82] João Pedrosa, Guilherme Aresta, Carlos Ferreira, Gurraj Atwal, Hady Ahmady Phoulady, Xiaoyu Chen, Rongzhen Chen, Jiaoliang Li, Liansheng Wang, Adrian Galdran, et al. Lndb challenge on automatic lung cancer patient management. *Medical image analysis*, 70:102027, 2021.
- [83] Sérgio Pereira, Adriano Pinto, Victor Alves, and Carlos A Silva. Brain tumor segmentation using convolutional neural networks in mri images. *IEEE Transactions on Medical Imaging*, 35(5):1240–1251, 2016.

- [84] Gašper Podobnik, Primož Strojani, Primož Peterlin, Bulat Ibragimov, and Tomaž Vrtovec. Han-seg: The head and neck organ-at-risk ct and mr segmentation dataset. *Medical physics*, 50(3):1917–1927, 2023.
- [85] Junyi Qiu, Lei Li, Sihan Wang, Ke Zhang, Yinyin Chen, Shan Yang, and Xiahai Zhuang. Myops-net: Myocardial pathology segmentation with flexible combination of multi-sequence cmr images. *Medical Image Analysis*, 84:102694, 2023.
- [86] Félix Quinton, Romain Popoff, Benoît Presles, Sarah Leclerc, Fabrice Meriaudeau, Guillaume Nodari, Olivier Lopez, Julie Pellegrinelli, Olivier Chevallier, Dominique Ginhac, et al. A tumour and liver automatic segmentation (atlas) dataset on contrast-enhanced magnetic resonance imaging for hepatocellular carcinoma. *Data*, 8(5):79, 2023.
- [87] Lukas Radl, Yuan Jin, Antonio Pepe, Jianning Li, Christina Gsaxner, Fen-hua Zhao, and Jan Egger. Avt: Multicenter aortic vessel tree cta dataset collection with ground truth segmentation masks. *Data in brief*, 40:107801, 2022.
- [88] Patrik F Raudaschl, Paolo Zaffino, Gregory C Sharp, Maria Francesca Spadea, Antong Chen, Benoit M Dawant, Thomas Albrecht, Tobias Gass, Christoph Langguth, Marcel Lüthi, et al. Evaluation of segmentation methods on head and neck ct: auto-segmentation challenge 2015. *Medical physics*, 44(5):2020–2036, 2017.
- [89] François Remy, Kris Demuynck, and Thomas Demeester. Biolord: Learning ontological representations from definitions (for biomedical concepts and their textual descriptions). *arXiv preprint arXiv:2210.11892*, 2022.
- [90] Blaine Rister, Darvin Yi, Kaushik Shivakumar, Tomomi Nobashi, and Daniel L Rubin. Ct-org, a new dataset for multiple organ segmentation in computed tomography. *Scientific Data*, 7(1):381, 2020.
- [91] Richard J Roberts. Pubmed central: The genbank of the published literature, 2001.
- [92] Olaf Ronneberger, Philipp Fischer, and Thomas Brox. U-net: Convolutional networks for biomedical image segmentation. In *Medical Image Computing and Computer-Assisted Intervention (MICCAI)*, pages 234–241. Springer, 2015.
- [93] H. Roth, A. Farag, E. B. Turkbey, L. Lu, J. Liu, and R. M. Summers. Data from pancreas-ct (version 2). <https://doi.org/10.7937/K9/TCIA.2016.tNB1kqBU>, 2016.
- [94] Jo Schlemper, Ozan Oktay, Michiel Schaap, Mattias Heinrich, Bernhard Kainz, Ben Glocker, and Daniel Rueckert. Attention gated networks: Learning to leverage salient regions in medical images. *Medical Image Analysis*, 53:197–207, 2019.
- [95] Anjany Sekuboyina, Malek E Hussein, Amirhossein Bayat, Maximilian Löffler, Hans Liebl, Hongwei Li, Giles Tetteh, Jan Kukačka, Christian Payer, Darko Štern, et al. Verse: A vertebrae labelling and segmentation benchmark for multi-detector ct images. *Medical image analysis*, 73:102166, 2021.
- [96] Ahmed Serag, Paul Aljabar, Gareth Ball, Serena J Counsell, James P Boardman, Mary A Rutherford, A David Edwards, Joseph V Hajnal, and Daniel Rueckert. Construction of a consistent high-definition spatio-temporal atlas of the developing brain using adaptive kernel regression. *Neuroimage*, 59(3):2255–2265, 2012.
- [97] Arnaud Arindra Adiyoso Setio, Alberto Traverso, Thomas De Bel, Moira SN Berens, Cas Van Den Bogaard, Piergiorgio Cerello, Hao Chen, Qi Dou, Maria Evelina Fantacci, Bram Geurts, et al. Validation, comparison, and combination of algorithms for automatic detection of pulmonary nodules in computed tomography images: the luna16 challenge. *Medical image analysis*, 42:1–13, 2017.
- [98] Jiang Tian, Li Liu, Zhongchao Shi, and Feiyu Xu. Automatic couinaud segmentation from ct volumes on liver using glc-unet. In *International Workshop on Machine Learning in Medical Imaging*, pages 274–282. Springer, 2019.
- [99] Hugo Touvron, Louis Martin, Kevin Stone, Peter Albert, Amjad Almahairi, Yasmine Babaei, Nikolay Bashlykov, Soumya Batra, Prajjwal Bhargava, Shruti Bhosale, et al. Llama 2: Open foundation and fine-tuned chat models. *arXiv preprint arXiv:2307.09288*, 2023.
- [100] Constantin Ulrich, Fabian Isensee, Tassilo Wald, Maximilian Zenk, Michael Baumgartner, and Klaus H Maier-Hein. Multitalent: A multi-dataset approach to medical image segmentation. *arXiv preprint arXiv:2303.14444*, 2023.

- [101] Ashish Vaswani, Noam Shazeer, Niki Parmar, Jakob Uszkoreit, Llion Jones, Aidan N Gomez, Łukasz Kaiser, and Illia Polosukhin. Attention is all you need. *Advances in Neural Information Processing Systems*, 30, 2017.
- [102] Haoyu Wang, Sizheng Guo, Jin Ye, Zhongying Deng, Junlong Cheng, Tianbin Li, Jianpin Chen, Yanzhou Su, Ziyang Huang, Yiqing Shen, et al. Sam-med3d. *arXiv preprint arXiv:2310.15161*, 2023.
- [103] Shuo Wang, Chen Qin, Chengyan Wang, Kang Wang, Haoran Wang, Chen Chen, Cheng Ouyang, Xutong Kuang, Chengliang Dai, Yuanhan Mo, Zhang Shi, Chenchen Dai, Xinrong Chen, He Wang, and Wenjia Bai. The extreme cardiac mri analysis challenge under respiratory motion (cmrxmotion), 2022.
- [104] Yixin Wang, Yao Zhang, Yang Liu, Jiang Tian, Cheng Zhong, Zhongchao Shi, Yang Zhang, and Zhiqiang He. Does non-covid-19 lung lesion help? investigating transferability in covid-19 ct image segmentation. *Computer Methods and Programs in Biomedicine*, 202:106004, 2021.
- [105] Yueyue Wang, Liang Zhao, Manning Wang, and Zhijian Song. Organ at risk segmentation in head and neck ct images using a two-stage segmentation framework based on 3d u-net. *IEEE Access*, 7:144591–144602, 2019.
- [106] Jakob Wasserthal, Hanns-Christian Breit, Manfred T Meyer, Maurice Pradella, Daniel Hinck, Alexander W Sauter, Tobias Heye, Daniel T Boll, Joshy Cyriac, Shan Yang, et al. Totalsegmentator: Robust segmentation of 104 anatomic structures in ct images. *Radiology: Artificial Intelligence*, 5(5), 2023.
- [107] Chaoyi Wu, Feng Chang, Xiao Su, Zhihan Wu, Yanfeng Wang, Ling Zhu, and Ya Zhang. Integrating features from lymph node stations for metastatic lymph node detection. *Computerized Medical Imaging and Graphics*, 101:102108, 2022.
- [108] Chaoyi Wu, Xiaoman Zhang, Yanfeng Wang, Ya Zhang, and Weidi Xie. K-diag: Knowledge-enhanced disease diagnosis in radiographic imaging. *MICCAI Workshop on Big Task Small Data (BTS D)*, 2023.
- [109] Chaoyi Wu, Xiaoman Zhang, Ya Zhang, Yanfeng Wang, and Weidi Xie. Medklip: Medical knowledge enhanced language-image pre-training for x-ray diagnosis. In *Proceedings of the IEEE/CVF International Conference on Computer Vision*, pages 21372–21383, October 2023.
- [110] Chaoyi Wu, Xiaoman Zhang, Ya Zhang, Yanfeng Wang, and Weidi Xie. Pmc-llama: Further finetuning llama on medical papers. *arXiv preprint arXiv:2304.14454*, 2023.
- [111] Xiaozheng Xie, Jianwei Niu, Xuefeng Liu, Zhengsu Chen, Shaojie Tang, and Shui Yu. A survey on incorporating domain knowledge into deep learning for medical image analysis. *Medical Image Analysis*, 69:101985, 2021.
- [112] Yutong Xie, Jianpeng Zhang, Chunhua Shen, and Yong Xia. Cotr: Efficiently bridging cnn and transformer for 3d medical image segmentation. In *Medical Image Computing and Computer-Assisted Intervention (MICCAI)*, pages 171–180. Springer, 2021.
- [113] Ke Yan, Xiaosong Wang, Le Lu, and Ronald M Summers. Deeplesion: automated mining of large-scale lesion annotations and universal lesion detection with deep learning. *Journal of medical imaging*, 5(3):036501–036501, 2018.
- [114] Yiwen Ye, Yutong Xie, Jianpeng Zhang, Ziyang Chen, and Yong Xia. Uniseg: A prompt-driven universal segmentation model as well as a strong representation learner. *arXiv preprint arXiv:2304.03493*, 2023.
- [115] Qihang Yu, Lingxi Xie, Yan Wang, Yuyin Zhou, Elliot K Fishman, and Alan L Yuille. Recurrent saliency transformation network: Incorporating multi-stage visual cues for small organ segmentation. In *Proceedings of the IEEE Conference on Computer Vision and Pattern Recognition*, pages 8280–8289, 2018.
- [116] Xiaoman Zhang, Chaoyi Wu, Ya Zhang, Weidi Xie, and Yanfeng Wang. Knowledge-enhanced visual-language pre-training on chest radiology images. *Nature Communications*, 14(1):4542, 2023.
- [117] Yao Zhang, Nanjun He, Jiawei Yang, Yuexiang Li, Dong Wei, Yawen Huang, Yang Zhang, Zhiqiang He, and Yefeng Zheng. mmformer: Multimodal medical transformer for incomplete multimodal learning of brain tumor segmentation. In *International Conference on Medical Image Computing and Computer-Assisted Intervention (MICCAI)*, pages 107–117. Springer, 2022.
- [118] Yixiao Zhang, Xinyi Li, Huimiao Chen, Alan L Yuille, Yaoyao Liu, and Zongwei Zhou. Continual learning for abdominal multi-organ and tumor segmentation. In *International Conference on Medical Image Computing and Computer-Assisted Intervention (MICCAI)*, pages 35–45. Springer, 2023.

- [119] Yao Zhang, Jiawei Yang, Yang Liu, Jiang Tian, Siyun Wang, Cheng Zhong, Zhongchao Shi, Yang Zhang, and Zhiqiang He. Decoupled pyramid correlation network for liver tumor segmentation from ct images. *Medical Physics*, 49(11):7207–7221, 2022.
- [120] Yao Zhang, Jiawei Yang, Jiang Tian, Zhongchao Shi, Cheng Zhong, Yang Zhang, and Zhiqiang He. Modality-aware mutual learning for multi-modal medical image segmentation. In *Medical Image Computing and Computer-Assisted Intervention (MICCAI)*, pages 589–599. Springer, 2021.
- [121] Qiaoyu Zheng, Weike Zhao, Chaoyi Wu, Xiaoman Zhang, Ya Zhang, Yanfeng Wang, and Weidi Xie. Large-scale long-tailed disease diagnosis on radiology images. *arXiv preprint arXiv:2312.16151*, 2023.
- [122] Hong-Yu Zhou, Jiansen Guo, Yinghao Zhang, Xiaoguang Han, Lequan Yu, Liansheng Wang, and Yizhou Yu. nnformer: volumetric medical image segmentation via a 3d transformer. *IEEE Transactions on Image Processing*, 2023.
- [123] Yuhang Zhou, Shu-Wen Sun, Qiu-Ping Liu, Xun Xu, Ya Zhang, and Yu-Dong Zhang. Ted: Two-stage expert-guided interpretable diagnosis framework for microvascular invasion in hepatocellular carcinoma. *Medical Image Analysis*, 82:102575, 2022.
- [124] Yuhang Zhou, Xiaoman Zhang, Shixiang Feng, and Ya Zhang. Uncertainty-aware incremental learning for multi-organ segmentation. *arXiv preprint arXiv:2103.05227*, 2021.
- [125] Zongwei Zhou, Md Mahfuzur Rahman Siddiquee, Nima Tajbakhsh, and Jianming Liang. Unet++: Redesigning skip connections to exploit multiscale features in image segmentation. *IEEE Transactions on Medical Imaging*, 39(6):1856–1867, 2019.
- [126] Xiahai Zhuang and Juan Shen. Multi-scale patch and multi-modality atlases for whole heart segmentation of mri. *Medical image analysis*, 31:77–87, 2016.

10 Appendix

10.1 Dataset-wise Comparison of SAT-Pro, SAT-Nano and nnU-Nets

Table 2 | Dataset-wise comparison of SAT-Pro, SAT-Nano and nnU-Nets on 72 individual datasets. The results of nnU-Nets are aggregated from the assemble of 72 specialist models trained separately on the corresponding datasets. TS is the abbreviation for TotalSegmentator.

Dataset	DSC \uparrow			NSD \uparrow		
	nnU-Nets	SAT-Nano	SAT-Pro	nnU-Nets	SAT-Nano	SAT-Pro
AbdomenCT1K [71]	95.09	93.26	94.27	88.24	84.41	87.25
ACDC [9]	90.76	85.75	87.74	97.62	66.77	72.42
AMOS22 CT [40]	89.76	84.74	86.36	87.11	80.21	83.03
AMOS22 MRI [40]	86.4	77.56	79.5	79.54	74.01	75.83
ATLAS [86]	78.17	70.41	75.93	45.25	40.21	47.14
ATLASR2 [59]	53.42	52.21	61.77	48.85	51.57	61.41
autoPET [25]	75.09	62.62	68.65	57.99	48.17	56.36
Brain Atlas [96]	83.78	74.5	78.52	85.35	73.34	78.36
BrainPTM [6]	68.37	64.62	67.0	33.9	50.68	53.96
BraTS2023 GLI [74]	73.21	65.05	67.95	68.24	58.26	61.94
BraTS2023 MEN [48]	64.38	52.54	57.5	61.56	47.95	53.87
BraTS2023 MET [76]	47.6	41.36	44.02	46.01	37.22	41.76
BraTS2023 PED [44]	57.41	48.66	51.91	51.33	42.89	45.9
BraTS2023 SSA [3]	58.84	53.18	55.97	46.5	42.94	46.48
BTCV Abdomen [50]	77.48	79.02	80.11	74.76	76.22	76.54
BTCV Cervix [51]	70.49	72.97	73.78	46.92	49.21	51.27
CHAOS CT [43]	97.08	96.55	97.02	81.04	81.12	84.75
CHAOS MRI [43]	88.8	82.05	87.37	64.35	47.39	53.99
CMRxMotion [103]	91.14	87.24	88.21	86.54	70.39	73.01
Couinaud [98]	87.86	72.45	81.24	70.44	42.72	53.13
COVID-19 CT Seg [69]	91.53	69.36	76.1	77.02	48.68	52.96
CrossMoDA2021 [20]	81.38	74.33	78.27	93.01	93.06	95.71
CT-ORG [90]	75.72	84.92	89.81	66.55	72.0	77.23
CTPelvic1K [62]	76.23	95.18	95.84	73.21	96.28	97.56
DAP Atlas [39]	88.7	84.39	85.38	88.06	85.49	86.07
FeTA2022 [81]	76.34	68.98	73.14	81.92	75.62	80.25
FLARE22 [70]	93.36	89.72	91.15	91.15	85.76	89.54
FUMPE [73]	45.07	36.05	22.19	41.38	32.15	18.22
HAN Seg [84]	62.18	70.56	72.25	63.52	74.29	77.89
Hecktor2022 [4]	64.53	55.71	57.56	43.91	43.21	44.37
Instance [58]	81.89	54.16	69.8	80.54	45.25	66.06
ISLES2022 [36]	64.95	46.68	55.51	60.1	42.15	54.97
KiPA22 [33]	90.61	64.36	75.29	89.7	61.68	75.33
KiTS23 [1]	74.61	55.44	67.96	70.05	47.06	59.87
LAScarQS2022 Task1 [56]	70.69	66.82	69.05	77.3	75.39	80.51
LAScarQS2022 Task2 [56]	85.29	90.03	91.97	64.28	72.58	79.97
LNDb [82]	24.98	23.2	35.31	30.01	31.24	43.76
LUNA16 [97]	96.64	95.94	96.32	93.85	92.42	94.16
MM-WHS CT [126]	88.67	87.78	90.02	64.43	70.1	75.71
MM-WHS MR [126]	31.76	84.38	86.65	24.54	64.67	69.32

Continued on next page

Table 2 | Cont.

Dataset	DSC \uparrow			NSD \uparrow		
	nnU-Nets	SAT-Nano	SAT-Pro	nnU-Nets	SAT-Nano	SAT-Pro
MRSpineSeg [80]	68.97	73.56	71.49	58.82	68.62	66.31
MSD Cardiac [5]	94.28	90.01	92.58	64.21	77.29	82.98
MSD Colon [5]	54.39	23.97	34.23	51.07	15.7	28.64
MSD HepaticVessel [5]	67.74	55.02	63.33	61.85	46.49	56.24
MSD Hippocampus [5]	89.18	86.25	87.63	97.92	95.64	96.46
MSD Liver [5]	77.92	69.76	76.96	63.78	52.66	63.25
MSD Lung [5]	71.74	52.72	62.56	58.32	38.62	52.55
MSD Pancreas [5]	68.64	57.85	58.76	53.31	45.25	46.43
MSD Prostate [5]	71.32	73.38	78.25	51.1	49.53	56.19
MSD Spleen [5]	92.95	92.78	94.15	88.01	80.46	85.01
MyoPS2020 [85]	14.99	59.92	58.63	14.11	40.74	39.98
NSCLC [8]	42.04	75.47	77.44	37.57	58.51	62.59
Pancreas CT [93]	61.45	83.97	85.56	49.52	74.06	76.14
PARSE2022 [64]	85.69	70.96	74.08	90.26	64.53	70.71
PDDCA [88]	57.25	72.83	76.72	52.99	74.48	79.22
PROMISE12 [60]	88.86	84.35	86.46	71.9	57.73	64.51
SEGA [87]	88.87	82.02	84.01	80.09	69.4	74.51
SegRap2023 Task 1 [65]	78.71	82.31	84.85	80.37	86.51	89.23
SegRap2023 Task 2 [65]	74.58	64.96	70.91	52.01	44.91	51.45
SegTHOR [49]	91.38	81.23	86.53	82.64	69.72	75.01
SKI10 [53]	88.15	80.52	83.37	94.38	88.06	91.52
SLIVER07 [34]	97.3	97.02	97.45	85.62	83.4	86.99
ToothFairy [17]	83.19	62.69	78.02	89.53	67.61	83.58
TS Cardiac [106]	93.3	76.62	89.15	84.83	72.9	86.87
TS Muscles [106]	91.6	82.35	88.04	84.53	79.99	87.15
TS Organs [106]	93.22	83.64	87.7	86.06	78.49	84.15
TS Ribs [106]	92.1	76.14	83.72	91.95	80.43	88.68
TS V2 [106]	92.39	72.7	78.75	89.21	72.98	79.69
TS Vertebrae [106]	95.37	81.82	85.38	94.7	82.76	86.86
VerSe [95]	81.8	61.29	60.64	82.87	59.34	59.35
WMH [47]	77.02	62.92	68.97	88.88	76.58	84.05
WORD [66]	85.49	86.55	86.68	78.79	76.83	77.48

10.2 Class-wise Comparison of SAT-Pro, SAT-Nano and nnU-Nets

Table 3 | Class-wise comparison of SAT-Pro, SAT-Nano and nnU-Nets on common anatomical structures in abdomen, brain, spine, and pelvis. The results of nnU-Nets are aggregated from the assemble of 72 specialist models trained separately on the corresponding datasets.

Region	Modality	Anatomical Target	DSC \uparrow			NSD \uparrow		
			nnU-Nets	SAT-Pro	SAT-Nano	nnU-Nets	SAT-Pro	SAT-Nano
Abdomen	CT	Adrenal gland	84.72	81.54	79.24	89.97	90.26	87.83
	CT	Celiac trunk	85.64	87.56	84.55	92.62	94.35	92.7
	CT	Duodenum	84.76	80.77	79.23	77.18	73.62	71.01
	CT	Gallbladder	85.95	80.37	78.96	80.48	77.31	74.73
	CT	Inferior vena cava	92.17	90.94	89.93	87.25	88.77	86.6
	CT	Intestine	89.41	86.6	86.03	81.87	73.51	72.01
	CT	Kidney	91.97	93.23	91.21	89.05	90.28	86.64
	CT	Liver	94.06	96.21	95.12	82.97	84.4	80.99
	CT	Pancreas	85.26	86.09	85.21	74.79	77.55	75.4
	CT	Small bowel	78.46	76.43	75.52	65.85	64.16	61.63
	CT	Spleen	94.34	94.88	92.54	91.06	89.89	86.61
	CT	Stomach	91.71	76.04	72.01	81.26	62.3	56.92
	MRI	Adrenal gland	69.61	64.16	62.59	71.65	76.5	73.96
	MRI	Kidney	94.28	91.79	90.43	78.98	74.17	71.17
	MRI	Liver	92.98	92.9	90.94	68.99	64.37	61.24
	MRI	Pancreas	89.19	84.2	79.23	74.8	72.39	66.29
MRI	Spleen	90.44	88.12	80.81	75.3	67.22	60.42	
Brain	CT	Brainstem	88.3	86.29	85.4	71.24	73.24	70.3
	CT	Hippocampus	65.43	77.96	77.11	63.94	78.57	77.24
	CT	Temporal lobe	87.96	93.74	92.71	72.15	81.75	77.66
	MRI	Brain ventricle	77.24	80.62	74.73	86.26	89.72	83.31
	MRI	Cerebellum	93.23	90.94	88.37	93.17	86.0	79.57
	MRI	Parietal lobe	83.62	77.26	73.92	72.0	59.57	54.02
	MRI	Optic radiation	65.04	63.52	60.43	35.42	56.61	53.12
	MRI	Thalamus	91.09	87.4	85.06	93.5	88.97	84.79
Spine	CT	Lumbar vertebrae	88.78	75.85	74.56	89.2	74.3	73.34
	CT	Sacrum	96.77	92.35	89.22	96.31	91.94	89.89
	CT	Spinal canal	96.86	94.6	93.4	98.73	97.37	96.09
	CT	Spinal cord	87.6	83.71	83.14	85.36	87.42	86.1
	CT	Thoracic vertebrae	90.43	79.33	79.18	90.98	79.88	79.3
	MRI	Intervertebral discs	74.72	87.3	86.69	63.3	89.29	88.12
	MRI	Lumbar vertebrae	69.59	79.74	79.7	54.02	66.87	66.64
	MRI	Sacrum	67.31	79.64	79.99	55.61	68.22	70.06
MRI	Thoracic vertebrae	60.97	53.75	60.71	54.57	46.31	53.25	
Pelvis	CT	Gluteus maximus	79.98	96.37	91.74	68.51	93.56	88.25
	CT	Gluteus medius	87.3	93.33	84.01	73.04	90.88	79.62
	CT	Gluteus minimus	91.39	90.59	92.91	84.69	88.44	92.29
	CT	Hip	83.61	93.29	92.91	79.68	91.75	93.55
	CT	Iliopsoas	93.98	91.19	90.14	88.59	91.82	90.19
	CT	Iliac vena	92.04	89.96	75.48	90.22	90.71	76.73
	CT	Urinary bladder	88.53	89.19	87.23	74.36	73.49	70.51
	CT	Uterocervix	43.84	68.95	52.89	37.04	67.93	51.04
	CT	Uterus	59.34	51.28	51.28	44.86	36.29	35.46
MRI	Prostate	77.17	78.18	73.28	58.03	57.58	50.58	

Table 4 | Class-wise comparison of SAT-Pro, SAT-Nano and nnU-Nets on common anatomical structures in head and neck, lower limb, upper limb, whole body and common lesions. The results of nnU-Nets are aggregated from the assemble of 72 specialist models trained separately on the corresponding datasets.

Region	Modality	Anatomical Target	DSC \uparrow			NSD \uparrow		
			nnU-Nets	SAT-Pro	SAT-Nano	nnU-Nets	SAT-Pro	SAT-Nano
Head and neck	CT	Brain	94.92	98.03	94.78	91.53	91.65	88.28
	CT	Carotid artery	73.51	77.35	72.37	81.32	86.27	82.79
	CT	Cervical esophagus	62.0	67.31	60.06	57.53	69.79	61.1
	CT	Cheek	51.62	40.71	43.16	50.82	34.49	38.3
	CT	Cochlea	67.49	70.34	69.48	82.81	91.75	89.93
	CT	Eustachian tube bone	75.86	80.13	76.22	89.23	96.48	94.07
	CT	Eyeball	54.04	85.15	82.64	52.57	88.73	84.02
	CT	Lacrimal gland	35.26	49.52	48.55	43.7	67.06	66.5
	CT	Lens	75.67	76.97	75.25	87.22	93.76	92.53
	CT	Mandible	73.93	93.31	92.68	71.69	95.17	94.38
	CT	Middle ear	76.7	84.5	81.36	85.27	91.93	87.74
	CT	Optic nerve	59.4	71.71	59.15	68.47	89.46	75.78
	CT	Parotid gland	60.89	85.24	84.51	48.79	75.09	73.31
	CT	Submandibular gland	63.49	80.36	79.68	55.14	78.08	76.03
	CT	Thyroid gland	64.89	81.83	41.3	63.4	83.83	40.55
	CT	Tympanic cavity	74.37	78.83	78.59	85.61	94.05	93.36
MRI	Brain	95.11	94.59	94.42	37.75	53.91	53.17	
Lower limb	CT	Head of femur	92.78	90.1	91.77	84.97	78.75	81.25
	MRI	Femur bone	98.25	96.33	95.33	96.8	91.0	86.57
	MRI	Femur cartilage	78.87	71.52	66.7	91.39	89.84	86.39
	MRI	Tibia bone	98.19	97.11	96.06	97.11	95.16	92.32
	MRI	Tibia cartilage	77.3	68.5	63.94	92.21	90.23	86.98
Thorax	CT	Autochthon	93.23	95.71	93.82	83.73	95.02	91.36
	CT	Breast	44.43	61.82	58.17	30.97	61.33	56.36
	CT	Heart atrium	92.63	91.17	89.33	74.92	82.05	78.34
	MRI	Heart ventricle	93.83	92.2	88.97	78.62	81.78	75.05
	CT	Lung	95.6	92.36	90.44	89.83	81.63	77.8
	CT	Rib	93.39	85.62	80.47	94.52	89.86	84.98
	CT	Myocardium	93.1	88.8	83.66	84.23	83.63	75.39
	CT	Thoracic cavity	72.12	95.36	94.62	53.52	73.15	70.54
CT	Thymus	50.0	68.15	70.22	50.0	73.72	75.26	
Upper limb	CT	Clavicle	91.7	91.63	90.93	88.71	93.6	92.78
	CT	Humerus	82.53	88.92	87.06	74.26	89.53	86.39
	CT	Scapula	93.57	94.21	91.56	92.17	97.58	94.87
Whole body	CT	Bone	70.06	79.41	64.72	61.78	69.8	54.22
	CT	Fat	98.49	96.43	95.81	97.8	96.35	94.91
	CT	Muscle	98.16	95.84	95.17	97.74	93.96	92.1
	CT	Skin	95.32	87.41	84.76	99.71	99.3	98.56
	PET	Lymph node	58.68	51.87	50.15	38.53	38.66	37.01
Lesions	CT	Liver tumor	66.0	61.47	45.64	50.26	43.83	28.09
	CT	Lung nodule	24.45	37.08	28.0	29.38	45.52	31.24
	MRI	Brain tumor	60.33	55.46	52.12	54.78	50.14	45.85
	MRI	Myocardial edema	5.37	7.5	13.09	9.02	13.34	17.23
	MRI	Stroke	59.32	58.28	48.8	54.52	57.95	46.86
	PET	Head and neck tumor	70.35	64.72	61.34	49.16	52.33	49.42
	PET	Tumor	74.98	68.56	62.27	57.94	56.3	48.17

10.3 Dataset-wise Results in Text Encoder Ablation Study

Table 5 | Dataset-wise comparison of three SAT-Nano variants with different text encoders. ‘Ours’ denotes the SAT-Nano prompted with the text encoder pre-trained on our multi-modal medical knowledge graph; ‘MedCPT’ denotes the variant with MedCPT as text encoder; BERT-Base denotes the variant with BERT-base as text encoder.

Dataset	DSC \uparrow			NSD \uparrow		
	Ours	MedCPT	BERT-Base	Ours	MedCPT	BERT-Base
AbdomenCT1K [71]	93.14	92.49	92.41	85.31	82.49	82.23
ACDC [9]	86.1	85.3	85.03	69.39	66.39	65.82
AMOS22 CT [40]	85.81	84.48	84.31	82.25	79.07	78.84
AMOS22 MRI [40]	80.58	80.77	75.44	76.79	75.39	70.12
ATLAS [86]	62.62	67.9	69.7	38.47	39.22	40.53
ATLASR2 [59]	55.15	53.8	53.39	54.49	49.68	50.18
Brain Atlas [96]	76.35	74.77	75.57	76.11	72.64	73.59
BrainPTM [6]	65.85	66.25	65.57	53.8	51.95	51.35
CHAOS MRI [43]	85.06	82.59	83.67	52.41	46.68	48.21
CMRxMotion [103]	88.57	87.01	86.81	75.15	68.85	67.8
Couinaud [98]	79.28	81.36	80.44	53.89	54.62	53.78
CrossMoDA2021 [20]	73.62	71.91	71.78	93.59	90.98	91.93
CT-ORG [90]	87.02	89.82	89.15	74.49	75.9	75.0
CTPelvic1K [62]	95.72	94.76	94.79	97.37	95.91	95.84
FeTA2022 [81]	72.19	68.98	68.69	79.61	75.31	75.12
FLARE22 [70]	88.42	88.97	89.19	86.26	85.37	85.57
FUMPE [73]	35.16	36.11	30.14	35.83	31.91	28.93
HAN Seg [84]	70.63	68.95	65.37	76.56	73.44	67.88
Instance [58]	52.49	61.0	56.56	42.54	51.65	46.67
ISLES2022 [36]	41.14	44.2	42.27	39.87	42.41	39.96
KiPA22 [33]	63.98	67.52	67.46	62.13	65.89	66.51
KiTS23 [1]	60.09	53.49	55.22	51.63	43.66	45.42
LAScarQS2022 Task1 [56]	67.8	65.6	66.44	79.54	73.42	74.5
LAScarQS2022 Task2 [56]	91.66	88.78	89.09	79.28	69.87	69.73
LNDb [82]	18.91	5.14	9.96	21.34	8.01	12.73
LUNA16 [97]	96.52	95.92	96.02	94.85	93.02	93.25
MMWHS CT [126]	87.79	88.23	89.08	68.79	69.85	72.82
MMWHS MRI [126]	84.97	85.82	85.38	65.32	66.85	65.89
MRSpineSeg [80]	77.25	76.21	76.97	74.14	72.45	72.67
MyoPS2020 [85]	59.55	59.54	59.68	41.64	40.68	40.9
NSCLC [8]	75.21	74.17	75.42	60.88	56.99	57.3
Pancreas CT [93]	86.47	83.79	83.89	79.27	72.39	72.31
PARSE2022 [64]	73.73	68.56	68.04	70.03	54.16	51.62
PDDCA [88]	72.98	73.44	72.9	75.45	74.29	73.57
PROMISE12 [60]	83.24	84.23	82.67	55.04	57.34	52.78
SEGA [87]	80.08	77.68	79.32	69.56	63.48	65.51
SegRap2023 Task1 [65]	85.22	85.12	84.93	90.29	89.72	89.54
SegRap2023 Task2 [65]	67.35	64.95	65.69	46.51	43.85	43.86
SegTHOR [49]	86.17	84.59	84.8	72.19	67.75	68.62
SKI10 [53]	82.05	81.25	81.08	89.98	88.27	88.38
SLIVER07 [34]	97.41	96.59	96.74	86.63	80.76	81.89
TS Cardiac [106]	88.99	86.96	85.93	86.64	83.04	81.99

Continued on next page

Table 5 | Cont.

Dataset	DSC \uparrow			NSD \uparrow		
	Ours	MedCPT	BERT-Base	Ours	MedCPT	BERT-Base
TS Muscles [106]	90.32	87.04	87.93	89.49	85.15	85.95
TS Organs [106]	87.18	84.13	85.37	83.27	78.71	79.8
TS Ribs [106]	86.27	82.72	84.0	89.03	86.86	88.7
TS Vertebrae [106]	85.99	83.25	81.57	86.73	83.5	81.77
VerSe [95]	78.19	76.51	70.77	77.7	75.56	69.69
WMH [47]	64.61	62.07	61.59	78.89	75.69	75.14
WORD [66]	86.49	84.79	84.79	76.96	72.42	72.4

10.4 Class-wise Results in Text Encoder Ablation Study

Table 6 | Class-wise comparison of three SAT-Nano variants with different text encoders on common anatomical structures in abdomen, brain, spine, and pelvis. ‘Ours’ denotes the SAT-Nano prompted with the text encoder pre-trained on our multi-modal medical knowledge graph; ‘MedCPT’ denotes the variant with MedCPT as text encoder; BERT-Base denotes the variant with BERT-base as text encoder.

Region	Modality	Anatomical Target	DSC \uparrow			NSD \uparrow		
			Ours	MedCPT	BERT-Base	Ours	MedCPT	BERT-Base
Abdomen	CT	Adrenal gland	80.14	78.54	78.52	88.48	86.94	86.91
	CT	Duodenum	77.23	75.88	76.58	68.65	65.15	66.11
	CT	Gallbladder	81.29	78.48	79.28	76.4	72.19	72.76
	CT	Inferior vena cava	89.26	88.41	87.81	86.06	84.05	83.26
	CT	Intestine	86.21	82.72	82.81	72.69	63.93	64.77
	CT	Kidney	94.08	93.41	93.34	90.37	88.69	88.39
	CT	Liver	95.8	94.97	95.02	83.69	79.47	79.5
	CT	Pancreas	85.13	82.12	83.61	76.41	70.91	72.52
	CT	Small bowel	75.78	78.24	78.62	68.82	69.27	69.3
	CT	Spleen	94.71	93.8	93.57	91.16	88.82	88.35
	CT	Stomach	85.1	87.93	89.3	71.75	71.14	72.39
	MRI	Adrenal gland	61.13	62.99	60.35	73.1	74.7	71.36
	MRI	Kidney	91.93	90.34	90.85	74.61	69.4	71.03
	MRI	Liver	91.29	90.69	91.6	64.15	61.02	60.69
	MRI	Pancreas	81.43	82.78	82.51	69.09	69.41	69.02
MRI	Spleen	84.53	82.11	82.63	63.45	61.7	62.31	
Brain	CT	Brainstem	86.66	85.2	84.1	74.95	69.55	68.18
	CT	Hippocampus	78.36	77.17	77.02	79.7	77.51	77.55
	CT	Temporal lobe	94.52	94.26	94.23	85.6	83.86	83.86
	MRI	Brain ventricle	77.48	75.86	76.0	86.27	83.23	83.26
	MRI	Cerebellum	89.89	88.72	88.85	84.8	80.23	80.83
	MRI	Parietal lobe	75.57	74.47	73.97	57.82	53.83	53.23
	MRI	Optic radiation	61.06	60.41	60.99	55.35	52.84	53.56
	MRI	Thalamus	85.28	84.72	84.88	85.44	83.69	83.89
Spine	CT	Lumbar vertebrae	77.03	73.88	73.05	76.64	72.58	71.33
	CT	Sacrum	94.15	92.81	85.87	94.82	92.75	85.59
	CT	Spinal cord	82.49	79.99	76.93	87.46	82.54	77.93
	CT	Thoracic vertebrae	80.21	79.04	78.59	80.33	78.67	78.25
	MRI	Intervertebral discs	88.67	88.21	88.05	91.43	90.92	90.42
	MRI	Lumbar vertebrae	81.95	81.49	81.87	72.96	70.83	71.08
	MRI	Sacrum	83.71	81.58	81.4	77.75	73.0	72.88
	MRI	Thoracic vertebrae	64.5	59.57	64.72	59.06	53.72	58.12
Pelvis	CT	Gluteus maximus	94.54	95.39	94.05	90.96	90.19	88.63
	CT	Gluteus medius	91.99	90.19	92.93	88.9	84.74	87.15
	CT	Gluteus minimus	93.76	91.85	89.71	93.36	90.26	87.83
	CT	Hip	95.48	92.95	93.89	96.14	93.24	94.13
	CT	Iliopsoas	91.32	89.98	87.99	91.52	88.72	86.64
	CT	Iliac vena	90.69	89.17	85.38	92.32	90.69	86.72
	CT	Urinary bladder	86.28	83.71	82.32	69.11	63.38	61.65
	MRI	Prostate	83.24	84.23	82.67	55.04	57.34	52.78

Table 7 | Class-wise comparison of three SAT-Nano variants with different text encoders on common anatomical structures in head and neck, lower limb, upper limb and whole body, and on common lesions. ‘Ours’ denotes the SAT-Nano prompted with the text encoder pre-trained on our multi-modal medical knowledge graph; ‘MedCPT’ denotes the variant with MedCPT as text encoder; BERT-Base denotes the variant with BERT-base as text encoder.

Region	Modality	Anatomical Target	DSC \uparrow			NSD \uparrow		
			Ours	MedCPT	BERT-Base	Ours	MedCPT	BERT-Base
Head and neck	CT	Brain	89.97	96.43	97.85	86.86	91.38	93.13
	CT	Carotid artery	66.6	60.76	60.63	80.1	68.93	69.05
	CT	Cervical esophagus	61.46	64.13	61.99	62.33	68.21	63.18
	CT	Cochlea	70.75	68.99	69.65	90.59	89.94	89.88
	CT	Eustachian tube bone	79.42	81.81	81.71	95.86	97.1	97.44
	CT	Eyeball	85.84	84.18	84.88	88.56	85.85	86.61
	CT	Lacrimal gland	47.62	47.32	0.0	66.76	65.35	0.0
	CT	Lens	73.89	73.9	74.37	90.48	91.87	91.9
	CT	Mandible	94.3	93.26	92.79	96.69	95.28	94.34
	CT	Middle ear	87.04	82.52	85.11	93.8	88.51	91.96
	CT	Optic nerve	61.67	70.52	71.01	78.05	88.25	88.48
	CT	Parotid gland	85.27	83.89	84.09	76.23	73.01	72.81
	CT	Submandibular gland	79.94	78.91	78.25	77.51	75.9	74.39
	CT	Tympanic cavity	82.53	81.4	81.0	95.28	94.7	94.48
	CT	Thyroid gland	85.61	82.79	82.49	87.85	82.09	80.97
MRI	Brain	95.21	94.72	94.36	58.25	55.57	53.53	
Lower limb	CT	Head of femur	91.86	88.21	88.17	81.87	75.11	74.59
	MRI	Femur bone	95.8	95.43	95.37	88.57	87.43	86.9
	MRI	Femur cartilage	68.8	67.85	66.77	88.03	85.83	86.15
	MRI	Tibia bone	96.53	96.25	96.31	93.83	92.24	92.48
	MRI	Tibia cartilage	67.07	65.47	65.87	89.48	87.57	87.98
Thorax	CT	Autochthon	93.06	91.97	92.15	90.33	85.79	85.95
	CT	Heart atrium	91.13	90.16	89.29	79.94	76.89	77.68
	MRI	Heart ventricle	87.49	87.84	89.31	70.48	71.1	72.71
	CT	Lung	91.14	90.05	90.06	84.42	80.81	80.59
	CT	Rib	86.04	82.54	83.83	88.76	86.6	88.45
	CT	Myocardium	84.96	84.28	86.7	74.58	75.1	75.97
	CT	Thoracic cavity	95.35	94.64	94.56	74.4	70.21	69.38
Upper limb	CT	Clavicle	92.11	82.82	85.65	93.24	84.3	87.04
	CT	Humerus	85.91	80.38	79.68	86.43	80.17	79.62
	CT	Scapula	92.54	80.47	88.3	94.7	83.45	91.46
Abnormal	CT	Lung nodule	18.91	5.14	9.96	21.34	8.01	12.73
	MRI	Myocardial edema	12.24	9.32	14.41	18.83	14.48	19.69
	MRI	Stroke	48.14	49.0	47.83	47.18	46.05	45.07

10.5 Dataset-wise Results in Visual Backbone Ablation Study

Table 8 | Dataset-wise comparison of three SAT-Nano variants with different visual backbones. ‘U-Net’ denotes the SAT-Nano based on U-Net; ‘U-Mamba’ denotes the variant based on U-Mamba; ‘SwinUNETR’ denotes the variant based on SwinUNETR.

Dataset	DSC \uparrow			NSD \uparrow		
	U-Net	U-Mamba	SwinUNETR	U-Net	U-Mamba	SwinUNETR
AbdomenCT1K [71]	92.49	92.67	89.88	82.49	83.6	74.1
ACDC [9]	85.3	83.82	82.3	66.39	63.68	59.04
AMOS22 CT [40]	85.81	84.71	78.05	82.25	79.65	66.03
AMOS22 MRI [40]	80.77	80.53	75.47	75.39	75.63	66.96
ATLAS [86]	67.9	64.5	63.82	39.22	39.33	36.07
ATLASR2 [59]	53.8	55.96	51.66	49.68	52.06	46.06
Brain Atlas [96]	74.77	75.05	64.99	72.64	73.53	59.49
BrainPTM [6]	66.25	65.09	64.96	51.95	51.08	49.48
CHAOS MRI [43]	82.59	81.14	81.5	46.68	48.2	42.96
CMRxMotion [103]	87.01	86.47	85.48	68.85	67.58	63.75
Couinaud [98]	81.36	80.87	75.58	54.62	54.21	44.92
CrossMoDA2021 [20]	71.91	73.37	68.7	90.98	92.04	89.86
CT-ORG [90]	89.82	88.75	87.65	75.9	75.4	70.02
CTPelvic1K [62]	94.76	95.24	92.58	95.91	96.29	90.89
FeTA2022 [81]	68.98	69.84	60.57	75.31	76.54	65.0
FLARE22 [70]	88.97	89.44	83.05	85.37	86.02	73.77
FUMPE [73]	36.11	34.21	26.01	31.91	32.15	24.98
HAN Seg [84]	68.95	69.89	55.67	73.44	74.97	55.62
Instance22 [58]	61.0	58.64	36.44	51.65	46.78	26.63
ISLES2022 [36]	44.2	43.95	43.82	42.41	42.63	40.77
KiPA22 [33]	67.52	66.34	61.49	65.89	63.84	57.35
KiTS23 [1]	53.49	54.5	49.75	43.66	45.48	38.41
LAScarQS2022 Task1 [56]	65.6	67.08	64.35	73.42	75.82	69.96
LAScarQS2022 Task2 [56]	88.78	87.52	86.06	69.87	68.91	62.89
LNDb [82]	5.14	14.9	14.17	8.01	19.03	15.67
LUNA16 [97]	95.92	96.37	95.28	93.02	93.39	87.52
MMWHS CT [126]	88.23	85.58	85.67	69.85	64.93	62.98
MMWHS MRI [126]	85.82	85.17	82.15	66.85	66.85	59.54
MRSpineSeg [80]	76.21	76.0	68.33	72.45	71.54	61.29
MyoPS2020 [85]	59.54	60.16	59.79	40.68	41.59	40.49
NSCLC [8]	74.17	75.28	73.66	56.99	57.81	55.93
Pancreas CT [93]	83.79	84.52	80.61	72.39	74.27	64.5
PARSE2022 [64]	68.56	68.98	66.84	54.16	62.3	50.61
PDDCA [88]	73.44	74.41	66.88	74.29	76.28	62.7
PROMISE12 [60]	84.23	80.32	79.52	57.34	49.03	44.69
SEGA [87]	77.68	78.54	77.95	63.48	66.03	65.03
SegRap2023 Task1 [65]	85.12	84.71	80.8	89.72	89.12	83.27
SegRap2023 Task2 [65]	64.95	65.61	60.77	43.85	44.5	38.78
SegTHOR [49]	84.59	84.73	79.84	67.75	69.23	59.19
SKI10 [53]	81.25	81.37	78.63	88.27	88.06	83.55
SLIVER07 [34]	96.59	96.94	94.96	80.76	84.35	69.25
TS Cardiac [106]	86.96	83.72	81.52	83.04	79.93	72.13
TS Muscles [106]	87.04	85.07	84.61	85.15	83.08	78.19

Continued on next page

Table 8 | Cont.

Dataset	DSC \uparrow			NSD \uparrow		
	U-Net	U-Mamba	SwinUNETR	U-Net	U-Mamba	SwinUNETR
TS Organs [106]	84.13	82.36	77.69	78.71	76.86	65.08
TS Ribs [106]	82.72	84.1	68.65	86.86	87.7	71.88
TS Vertebrae [106]	83.25	82.04	70.25	83.5	82.43	66.1
VerSe [95]	76.51	70.91	68.36	75.56	70.0	65.09
WMH [47]	62.07	63.85	61.82	75.69	77.98	75.58
WORD [66]	84.79	85.25	78.6	72.42	73.89	59.68

10.6 Class-wise Results in Visual Backbone Ablation Study

Table 9 | Class-wise comparison of three SAT-Nano variants with different visual backbones on common anatomical structures in abdomen, brain, spine, and pelvis. ‘U-Net’ denotes the SAT-Nano based on U-Net; ‘U-Mamba’ denotes the variant based on U-Mamba; ‘SwinUNETR’ denotes the variant based on SwinUNETR.

Region	Modality	Anatomical Target	DSC \uparrow			NSD \uparrow		
			U-Net	U-Mamba	SwinUNETR	U-Net	U-Mamba	SwinUNETR
Abdomen	CT	Adrenal gland	78.54	79.03	71.97	86.94	87.41	79.02
	CT	Duodenum	75.88	73.89	66.05	65.15	63.77	50.51
	CT	Gallbladder	78.48	77.9	67.31	72.19	71.51	54.17
	CT	Inferior vena cava	88.41	87.35	79.98	84.05	82.96	66.37
	CT	Intestine	82.72	83.04	65.65	63.93	65.84	37.69
	CT	Kidney	93.41	93.25	90.74	88.69	88.64	82.23
	CT	Liver	94.97	95.42	92.35	79.47	81.66	65.55
	CT	Pancreas	82.12	83.44	77.43	70.91	73.35	60.9
	CT	Small bowel	78.24	71.92	57.71	69.27	62.77	41.44
	CT	Spleen	93.8	94.36	90.25	88.82	90.02	76.55
	CT	Stomach	87.93	87.39	79.88	71.14	71.46	48.43
	MRI	Adrenal gland	62.99	63.86	59.31	74.7	75.85	69.1
	MRI	Kidney	90.34	90.6	88.76	69.4	70.8	65.11
	MRI	Liver	90.69	90.34	89.57	61.02	61.67	55.64
MRI	Pancreas	82.78	81.32	75.76	69.41	68.49	58.7	
MRI	Spleen	82.11	78.48	81.21	61.7	61.9	55.71	
Brain	CT	Brainstem	85.2	84.33	82.35	69.55	68.91	61.72
	CT	Hippocampus	77.17	70.85	74.46	77.51	71.06	72.25
	CT	Temporal lobe	94.26	93.81	91.0	83.86	82.51	71.79
	MRI	Brain ventricle	75.86	76.04	65.04	83.23	83.34	70.19
	MRI	Cerebellum	88.72	89.18	80.13	80.23	82.15	57.62
	MRI	Parietal lobe	74.47	73.52	64.93	53.83	54.02	42.72
	MRI	Optic radiation	60.41	59.83	61.32	52.84	51.7	52.9
	MRI	Thalamus	84.72	83.77	79.08	83.69	81.27	72.55
Spine	CT	Lumbar vertebrae	73.88	73.37	67.38	72.58	72.01	61.53
	CT	Sacrum	92.81	91.31	89.01	92.75	91.47	85.08
	CT	Spinal cord	79.99	82.07	63.82	82.54	86.83	61.75
	CT	Thoracic vertebrae	79.04	75.64	62.92	78.67	75.49	58.4
	MRI	Intervertebral discs	88.21	87.76	85.97	90.92	89.81	87.49
	MRI	Lumbar vertebrae	81.49	81.15	74.77	70.83	69.76	59.43
	MRI	Sacrum	81.58	81.45	74.59	73.0	74.14	61.25
	MRI	Thoracic vertebrae	59.57	65.46	52.99	53.72	58.69	43.84
Pelvis	CT	Gluteus maximus	95.39	94.64	92.54	90.19	89.45	81.87
	CT	Gluteus medius	90.19	91.09	91.19	84.74	84.93	80.59
	CT	Gluteus minimus	91.85	90.92	86.39	90.26	88.97	80.41
	CT	Hip	92.95	92.91	92.99	93.24	93.1	90.72
	CT	Iliopsoas	89.98	82.42	83.17	88.72	81.21	74.85
	CT	Iliac vena	89.17	89.31	84.71	90.69	90.6	83.26
	CT	Urinary bladder	83.71	84.94	78.64	63.38	64.83	52.45
	MRI	Prostate	84.23	80.32	79.52	57.34	49.03	44.69

Table 10 | Class-wise comparison of three SAT-Nano variants with different visual backbones on common anatomical structures in head and neck, lower limb, upper limb and whole body, and on common lesions. ‘U-Net’ denotes the SAT-Nano based on U-Net; ‘U-Mamba’ denotes the variant based on U-Mamba; ‘SwinUNETR’ denotes the variant based on SwinUNETR.

Region	Modality	Anatomical Target	DSC \uparrow			NSD \uparrow		
			U-Net	U-Mamba	SwinUNETR	U-Net	U-Mamba	SwinUNETR
Head and neck	CT	Brain	96.43	91.95	95.61	91.38	88.45	82.17
	CT	Carotid artery	60.76	62.78	31.49	68.93	72.42	33.11
	CT	Cervical esophagus	64.13	59.58	41.62	68.21	59.77	41.72
	CT	Cochlea	68.99	69.07	66.73	89.94	89.45	89.35
	CT	Eustachian tube bone	81.81	82.44	78.51	97.1	97.6	96.08
	CT	Eyeball	84.18	84.34	79.12	85.85	86.24	76.38
	CT	Lacrimal gland	47.32	48.27	0.0	65.35	66.95	0.0
	CT	Lens	73.9	75.35	63.77	91.87	91.69	82.36
	CT	Mandible	93.26	93.58	88.38	95.28	95.52	85.75
	CT	Middle ear	82.52	83.53	81.2	88.51	89.91	88.92
	CT	Optic nerve	70.52	70.77	62.75	88.25	88.33	78.39
	CT	Parotid gland	83.89	84.66	80.64	73.01	74.85	63.7
	CT	Submandibular gland	78.91	79.45	75.78	75.9	76.93	68.87
	CT	Tympanic cavity	81.4	80.87	76.85	94.7	93.91	92.3
	CT	Thyroid gland	82.79	83.96	74.85	82.09	84.53	64.63
MRI	Brain	94.72	94.92	94.41	55.57	57.45	54.3	
Lower limb	CT	Head of femur	88.21	89.21	85.96	75.11	77.22	66.86
	MRI	Femur bone	95.43	95.24	94.15	87.43	85.94	81.78
	MRI	Femur cartilage	67.85	66.98	63.02	85.83	85.94	82.27
	MRI	Tibia bone	96.25	96.02	94.26	92.24	91.13	84.68
	MRI	Tibia cartilage	65.47	67.24	63.09	87.57	89.2	85.46
Thorax	CT	Autochthon	91.97	90.26	87.01	85.79	83.89	72.14
	CT	Heart atrium	90.16	87.1	86.02	76.89	72.57	65.35
	MRI	Heart ventricle	87.84	83.78	84.54	71.1	64.83	61.81
	CT	Lung	90.05	88.22	85.26	80.81	78.71	66.04
	CT	Rib	82.54	84.08	68.12	86.6	87.62	71.14
	CT	Myocardium	84.28	80.6	79.67	75.1	68.33	62.09
	CT	Thoracic cavity	94.64	94.82	93.81	70.21	69.91	68.41
Upper limb	CT	Clavicle	82.82	78.93	86.24	84.3	80.15	85.73
	CT	Humerus	80.38	77.63	65.62	80.17	78.08	58.56
	CT	Scapula	80.47	80.98	75.47	83.45	83.91	77.06
Abnormal	CT	Lung nodule	5.14	14.9	14.17	8.01	19.03	15.67
	MRI	Myocardial edema	9.32	12.79	15.9	14.48	18.75	20.06
	MRI	Stroke	49.0	49.95	47.74	46.05	47.35	43.42

10.7 Detailed Architecture of nnU-Nets Specialist

Table 11 | The configurations of 72 nnU-Nets trained on each dataset. All nnU-Nets are planned under ‘3d_fullres’ setting. The total size of all the nnU-Nets is around 2247M.

Dataset	Input Size	#Stage	#Depth	#Width	Model Size
AbdomenCT1K [71]	[96 160 160]	6	[2 2 2 2 2 2]	[32 64 128 256 320 320]	31M
ACDC [9]	[10 256 224]	6	[2 2 2 2 2 2]	[32 64 128 256 320 320]	31M
AMOS22 CT [40]	[64 192 160]	6	[2 2 2 2 2 2]	[32 64 128 256 320 320]	31M
AMOS22 MRI [40]	[64 160 224]	6	[2 2 2 2 2 2]	[32 64 128 256 320 320]	31M
ATLASR2 [59]	[128 128 128]	6	[2 2 2 2 2 2]	[32 64 128 256 320 320]	31M
ATLAS [86]	[48 192 224]	6	[2 2 2 2 2 2]	[32 64 128 256 320 320]	31M
autoPET [25]	[80 192 160]	6	[2 2 2 2 2 2]	[32 64 128 256 320 320]	31M
Brain Atlas [96]	[112 128 112]	5	[2 2 2 2 2]	[32 64 128 256 320]	17M
BrainPTM [6]	[112 144 112]	5	[2 2 2 2 2]	[32 64 128 256 320]	17M
BraTS2023 GLI [74]	[128 160 112]	6	[2 2 2 2 2 2]	[32 64 128 256 320 320]	31M
BraTS2023 MEN [48]	[128 160 112]	6	[2 2 2 2 2 2]	[32 64 128 256 320 320]	31M
BraTS2023 MET [76]	[128 160 112]	6	[2 2 2 2 2 2]	[32 64 128 256 320 320]	31M
BraTS2023 PED [44]	[128 128 128]	6	[2 2 2 2 2 2]	[32 64 128 256 320 320]	31M
BraTS2023 SSA [3]	[128 160 112]	6	[2 2 2 2 2 2]	[32 64 128 256 320 320]	31M
BTCV Cervix [51]	[64 192 160]	6	[2 2 2 2 2 2]	[32 64 128 256 320 320]	31M
BTCV Abdomen [50]	[48 192 192]	6	[2 2 2 2 2 2]	[32 64 128 256 320 320]	31M
CHAOS CT [43]	[48 224 192]	6	[2 2 2 2 2 2]	[32 64 128 256 320 320]	31M
CHAOS MRI [43]	[32 192 288]	6	[2 2 2 2 2 2]	[32 64 128 256 320 320]	31M
CMRxMotion [103]	[10 448 384]	7	[2 2 2 2 2 2 2]	[32 64 128 256 320 320 320]	45M
Couinaud [98]	[64 192 192]	6	[2 2 2 2 2 2]	[32 64 128 256 320 320]	31M
COVID-19 CT Seg [69]	[56 192 192]	6	[2 2 2 2 2 2]	[32 64 128 256 320 320]	31M
CrossMoDA2021 [20]	[48 224 192]	6	[2 2 2 2 2 2]	[32 64 128 256 320 320]	31M
CT-ORG [90]	[128 128 128]	6	[2 2 2 2 2 2]	[32 64 128 256 320 320]	31M
CTPelvic1K [62]	[96 160 160]	6	[2 2 2 2 2 2]	[32 64 128 256 320 320]	31M
DAP Atlas [39]	[80 128 128]	6	[2 2 2 2 2 2]	[32 64 128 256 320 320]	31M
FeTA2022 [81]	[96 112 96]	5	[2 2 2 2 2]	[32 64 128 256 320]	17M
FLARE22 [70]	[40 224 192]	6	[2 2 2 2 2 2]	[32 64 128 256 320 320]	31M
FUMPE [73]	[80 192 160]	6	[2 2 2 2 2 2]	[32 64 128 256 320 320]	31M
HAN Seg [84]	[40 224 192]	6	[2 2 2 2 2 2]	[32 64 128 256 320 320]	31M
Hecktor2022 [4]	[128 128 128]	6	[2 2 2 2 2 2]	[32 64 128 256 320 320]	31M
Instance22 [58]	[16 320 320]	7	[2 2 2 2 2 2 2]	[32 64 128 256 320 320 320]	45M
ISLES2022 [36]	[80 96 80]	5	[2 2 2 2 2]	[32 64 128 256 320]	17M
KiPA22 [33]	[160 128 112]	6	[2 2 2 2 2 2]	[32 64 128 256 320 320]	31M
KiTS23 [1]	[128 128 128]	6	[2 2 2 2 2 2]	[32 64 128 256 320 320]	31M
LAScarQS22 Task1 [56]	[24 256 256]	7	[2 2 2 2 2 2 2]	[32 64 128 256 320 320 320]	45M
LAScarQS22 Task2 [56]	[40 256 224]	6	[2 2 2 2 2 2]	[32 64 128 256 320 320]	31M
LNDb [82]	[96 160 160]	6	[2 2 2 2 2 2]	[32 64 128 256 320 320]	31M
LUNA16 [97]	[80 192 160]	6	[2 2 2 2 2 2]	[32 64 128 256 320 320]	31M
MM-WHS CT [126]	[80 192 160]	6	[2 2 2 2 2 2]	[32 64 128 256 320 320]	31M
MM-WHS MR [126]	[96 160 160]	6	[2 2 2 2 2 2]	[32 64 128 256 320 320]	31M
MRSpineSeg [80]	[8 640 320]	7	[2 2 2 2 2 2 2]	[32 64 128 256 320 320 320]	43M
MSD Colon [5]	[56 192 192]	6	[2 2 2 2 2 2]	[32 64 128 256 320 320]	31M
MSD Heart [5]	[80 192 160]	6	[2 2 2 2 2 2]	[32 64 128 256 320 320]	31M
MSD HepaticVessel [5]	[64 192 192]	6	[2 2 2 2 2 2]	[32 64 128 256 320 320]	31M
MSD Hippocampus [5]	[40 56 40]	4	[2 2 2 2]	[32 64 128 256]	6M
MSD Liver [5]	[128 128 128]	6	[2 2 2 2 2 2]	[32 64 128 256 320 320]	31M
MSD Lung [5]	[80 192 160]	6	[2 2 2 2 2 2]	[32 64 128 256 320 320]	31M
MSD Pancreas [5]	[40 224 224]	6	[2 2 2 2 2 2]	[32 64 128 256 320 320]	31M
MSD Prostate [5]	[16 320 320]	7	[2 2 2 2 2 2 2]	[32 64 128 256 320 320 320]	45M
MSD Spleen [5]	[64 192 160]	6	[2 2 2 2 2 2]	[32 64 128 256 320 320]	31M
MyoPS2020 [85]	[48 224 224]	6	[2 2 2 2 2 2]	[32 64 128 256 320 320]	31M
NSCLC [8]	[48 224 192]	6	[2 2 2 2 2 2]	[32 64 128 256 320 320]	31M
Pancreas CT [93]	[80 192 160]	6	[2 2 2 2 2 2]	[32 64 128 256 320 320]	31M

Continue on next page

Table 11 | Cont.

Dataset	#Input Size	#Stage	#Depth	#Width	Model Size
PARSE2022 [64]	[96 160 160]	6	[2 2 2 2 2 2]	[32 64 128 256 320 320]	31M
PDDCA [88]	[48 192 192]	6	[2 2 2 2 2 2]	[32 64 128 256 320 320]	31M
PROMISE12 [60]	[20 320 256]	7	[2 2 2 2 2 2 2]	[32 64 128 256 320 320 320]	45M
SEGA [87]	[72 160 160]	6	[2 2 2 2 2 2]	[32 64 128 256 320 320]	31M
SegRap2023 Task1 [65]	[28 256 224]	6	[2 2 2 2 2 2]	[32 64 128 256 320 320]	31M
SegRap2023 Task2 [65]	[28 256 256]	7	[2 2 2 2 2 2 2]	[32 64 128 256 320 320 320]	45M
SegTHOR [49]	[64 192 160]	6	[2 2 2 2 2 2]	[32 64 128 256 320 320]	31M
SKI10 [53]	[64 192 160]	6	[2 2 2 2 2 2]	[32 64 128 256 320 320]	31M
SLIVER07 [34]	[80 192 160]	6	[2 2 2 2 2 2]	[32 64 128 256 320 320]	31M
ToothFairy [17]	[80 192 160]	6	[2 2 2 2 2 2]	[32 64 128 256 320 320]	31M
TS Heart [106]	[128 128 128]	6	[2 2 2 2 2 2]	[32 64 128 256 320 320]	31M
TS Muscles [106]	[128 128 128]	6	[2 2 2 2 2 2]	[32 64 128 256 320 320]	31M
TS Organs [106]	[128 128 128]	6	[2 2 2 2 2 2]	[32 64 128 256 320 320]	31M
TS Ribs [106]	[128 128 128]	6	[2 2 2 2 2 2]	[32 64 128 256 320 320]	31M
TS Vertebrae [106]	[128 128 128]	6	[2 2 2 2 2 2]	[32 64 128 256 320 320]	31M
TS V2 [106]	[128 128 128]	6	[2 2 2 2 2 2]	[32 64 128 256 320 320]	31M
VerSe [95]	[160 128 112]	6	[2 2 2 2 2 2]	[32 64 128 256 320 320]	31M
WMH [47]	[48 224 192]	6	[2 2 2 2 2 2]	[32 64 128 256 320 320]	31M
WORD [66]	[64 192 160]	6	[2 2 2 2 2 2]	[32 64 128 256 320 320]	31M

10.8 All classes in SAT-DS

Table 12 | Detailed name list of the 497 classes involved in SAT-DS.

Name List 1	Name List 2	Name List 3
(ct) abdominal tissue	(ct) adrenal gland	(ct) anterior eyeball
(ct) aorta	(ct) arytenoid	(ct) autochthon
(ct) bone	(ct) brachiocephalic trunk	(ct) brachiocephalic vein
(ct) brain	(ct) brainstem	(ct) breast
(ct) bronchie	(ct) buccal mucosa	(ct) carotid artery
(ct) caudate lobe	(ct) celiac trunk	(ct) cervical esophagus
(ct) cervical vertebrae	(ct) cervical vertebrae 1 (c1)	(ct) cervical vertebrae 2 (c2)
(ct) cervical vertebrae 3 (c3)	(ct) cervical vertebrae 4 (c4)	(ct) cervical vertebrae 5 (c5)
(ct) cervical vertebrae 6 (c6)	(ct) cervical vertebrae 7 (c7)	(ct) cheek
(ct) clavicle	(ct) cochlea	(ct) colon
(ct) colon cancer	(ct) common carotid artery	(ct) costal cartilage
(ct) covid-19 infection	(ct) cricopharyngeal inlet	(ct) duodenum
(ct) esophagus	(ct) eustachian tube bone	(ct) eyeball
(ct) fat	(ct) femur	(ct) gallbladder
(ct) gluteus maximus	(ct) gluteus medius	(ct) gluteus minimus
(ct) gonad	(ct) head of femur	(ct) head of left femur
(ct) head of right femur	(ct) heart	(ct) heart ascending aorta
(ct) heart atrium	(ct) heart tissue	(ct) heart ventricle
(ct) hip	(ct) hippocampus	(ct) humerus
(ct) iliac artery	(ct) iliac vena	(ct) iliopsoas
(ct) inferior alveolar nerve	(ct) inferior vena cava	(ct) internal auditory canal
(ct) internal carotid artery	(ct) internal jugular vein	(ct) intestine
(ct) intracranial hemorrhage	(ct) kidney	(ct) kidney cyst
(ct) kidney tumor	(ct) lacrimal gland	(ct) larynx
(ct) larynx glottis	(ct) larynx supraglottis	(ct) left adrenal gland
(ct) left anterior eyeball	(ct) left auricle of heart	(ct) left autochthon
(ct) left brachiocephalic vein	(ct) left breast	(ct) left carotid artery
(ct) left cheek	(ct) left clavicle	(ct) left cochlea
(ct) left common carotid artery	(ct) left eustachian tube bone	(ct) left eyeball
(ct) left femur	(ct) left gluteus maximus	(ct) left gluteus medius
(ct) left gluteus minimus	(ct) left heart atrium	(ct) left heart ventricle
(ct) left hip	(ct) left hippocampus	(ct) left humerus
(ct) left iliac artery	(ct) left iliac vena	(ct) left iliopsoas
(ct) left internal auditory canal	(ct) left internal carotid artery	(ct) left internal jugular vein
(ct) left kidney	(ct) left kidney cyst	(ct) left lacrimal gland
(ct) left lateral inferior segment of liver	(ct) left lateral superior segment of liver	(ct) left lens
(ct) left lobe of liver	(ct) left lung	(ct) left lung lower lobe
(ct) left lung upper lobe	(ct) left mandible	(ct) left mastoid process
(ct) left medial segment of liver	(ct) left middle ear	(ct) left optic nerve
(ct) left parotid gland	(ct) left posterior eyeball	(ct) left rib
(ct) left rib 1	(ct) left rib 10	(ct) left rib 11
(ct) left rib 12	(ct) left rib 2	(ct) left rib 3
(ct) left rib 4	(ct) left rib 5	(ct) left rib 6
(ct) left rib 7	(ct) left rib 8	(ct) left rib 9
(ct) left scapula	(ct) left subclavian artery	(ct) left submandibular gland
(ct) left temporal lobe	(ct) left temporomandibular joint	(ct) left thyroid
(ct) left tympanic cavity	(ct) left vestibule semicircular canal	(ct) lens
(ct) lips	(ct) liver	(ct) liver tumor
(ct) liver vessel	(ct) lumbar vertebrae	(ct) lumbar vertebrae 1 (l1)
(ct) lumbar vertebrae 2 (l2)	(ct) lumbar vertebrae 3 (l3)	(ct) lumbar vertebrae 4 (l4)
(ct) lumbar vertebrae 5 (l5)	(ct) lumbar vertebrae 6 (l6)	(ct) lung
(ct) lung effusion	(ct) lung lower lobe	(ct) lung nodule
(ct) lung tumor	(ct) lung upper lobe	(ct) mandible
(ct) manubrium of sternum	(ct) mastoid process	(ct) mediastinal tissue
(ct) middle ear	(ct) muscle	(ct) myocardium

Table 12 | Cont.

Name List 1	Name List 2	Name List 3
(ct) nasal cavity	(ct) nasopharyngeal lymph node	(ct) nasopharyngeal tumor
(ct) optic chiasm	(ct) optic nerve	(ct) oral cavity
(ct) pancreas	(ct) pancreas tumor	(ct) parotid gland
(ct) pharynx constrictor muscle	(ct) pituitary gland	(ct) portal vein and splenic vein
(ct) posterior eyeball	(ct) prostate	(ct) pulmonary artery
(ct) pulmonary embolism	(ct) pulmonary vein	(ct) rectum
(ct) renal artery	(ct) renal vein	(ct) rib
(ct) rib 1	(ct) rib 10	(ct) rib 11
(ct) rib 12	(ct) rib 2	(ct) rib 3
(ct) rib 4	(ct) rib 5	(ct) rib 6
(ct) rib 7	(ct) rib 8	(ct) rib 9
(ct) rib cartilage	(ct) right adrenal gland	(ct) right anterior eyeball
(ct) right anterior inferior segment of liver	(ct) right anterior superior segment of liver	(ct) right autochthon
(ct) right brachiocephalic vein	(ct) right breast	(ct) right carotid artery
(ct) right cheek	(ct) right clavicle	(ct) right cochlea
(ct) right common carotid artery	(ct) right eustachian tube bone	(ct) right eyeball
(ct) right femur	(ct) right gluteus maximus	(ct) right gluteus medius
(ct) right gluteus minimus	(ct) right heart atrium	(ct) right heart ventricle
(ct) right hip	(ct) right hippocampus	(ct) right humerus
(ct) right iliac artery	(ct) right iliac vena	(ct) right iliopsoas
(ct) right internal auditory canal	(ct) right internal carotid artery	(ct) right internal jugular vein
(ct) right kidney	(ct) right kidney cyst	(ct) right lacrimal gland
(ct) right lens	(ct) right lobe of liver	(ct) right lung
(ct) right lung lower lobe	(ct) right lung middle lobe	(ct) right lung upper lobe
(ct) right mandible	(ct) right mastoid process	(ct) right middle ear
(ct) right optic nerve	(ct) right parotid gland	(ct) right posterior eyeball
(ct) right posterior inferior segment of liver	(ct) right posterior superior segment of liver	(ct) right rib
(ct) right rib 1	(ct) right rib 10	(ct) right rib 11
(ct) right rib 12	(ct) right rib 2	(ct) right rib 3
(ct) right rib 4	(ct) right rib 5	(ct) right rib 6
(ct) right rib 7	(ct) right rib 8	(ct) right rib 9
(ct) right scapula	(ct) right subclavian artery	(ct) right submandibular gland
(ct) right temporal lobe	(ct) right temporomandibular joint	(ct) right thyroid
(ct) right tympanic cavity	(ct) right vestibule semicircular canal	(ct) sacral vertebrae 1 (s1)
(ct) sacrum	(ct) scapula	(ct) skin
(ct) skull	(ct) small bowel	(ct) spinal canal
(ct) spinal cord	(ct) spleen	(ct) sternum
(ct) stomach	(ct) subclavian artery	(ct) submandibular gland
(ct) superior vena cava	(ct) temporal lobe	(ct) temporomandibular joint
(ct) thoracic cavity	(ct) thoracic vertebrae	(ct) thoracic vertebrae 1 (t1)
(ct) thoracic vertebrae 10 (t10)	(ct) thoracic vertebrae 11 (t11)	(ct) thoracic vertebrae 12 (t12)
(ct) thoracic vertebrae 2 (t2)	(ct) thoracic vertebrae 3 (t3)	(ct) thoracic vertebrae 4 (t4)
(ct) thoracic vertebrae 5 (t5)	(ct) thoracic vertebrae 6 (t6)	(ct) thoracic vertebrae 7 (t7)
(ct) thoracic vertebrae 8 (t8)	(ct) thoracic vertebrae 9 (t9)	(ct) thymus
(ct) thyroid gland	(ct) trachea	(ct) tympanic cavity
(ct) urinary bladder	(ct) uterocervix	(ct) uterus
(ct) vertebrae	(ct) vestibule semicircular canal	(mri) adrenal gland
(mri) amygdala	(mri) anterior hippocampus	(mri) aorta
(mri) basal ganglia	(mri) brain	(mri) brain edema
(mri) brain tumor	(mri) brain ventricle	(mri) brainstem
(mri) brainstem excluding substantia nigra	(mri) cerebellum	(mri) cingulate gyrus
(mri) cochlea	(mri) corpus callosum	(mri) corticospinal tract
(mri) deep grey matter	(mri) duodenum	(mri) enhancing brain tumor
(mri) esophagus	(mri) external cerebrospinal fluid	(mri) femur bone

Table 12 | Cont.

Name List 1	Name List 2	Name List 3
(mri) femur cartilage	(mri) frontal lobe	(mri) gallbladder
(mri) grey matter	(mri) heart ascending aorta	(mri) heart atrium
(mri) heart ventricle	(mri) hippocampus	(mri) inferior vena cava
(mri) insula	(mri) intervertebral disc between lumbar vertebrae 1 (l1) and lumbar vertebrae 2 (l2)	(mri) intervertebral disc between lumbar vertebrae 2 (l2) and lumbar vertebrae 3 (l3)
(mri) intervertebral disc between lumbar vertebrae 3 (l3) and lumbar vertebrae 4 (l4)	(mri) intervertebral disc between lumbar vertebrae 4 (l4) and lumbar vertebrae 5 (l5)	(mri) intervertebral disc between lumbar vertebrae 5 (l5) and sacrum
(mri) intervertebral disc between thoracic vertebrae 10 (t10) and thoracic vertebrae 11 (t11)	(mri) intervertebral disc between thoracic vertebrae 11 (t11) and thoracic vertebrae 12 (t12)	(mri) intervertebral disc between thoracic vertebrae 12 (t12) and lumbar vertebrae 1 (l1)
(mri) intervertebral disc between thoracic vertebrae 9 (t9) and thoracic vertebrae 10 (t10)	(mri) intervertebral discs	(mri) kidney
(mri) lateral ventricle	(mri) left adrenal gland	(mri) left amygdala
(mri) left angular gyrus	(mri) left anterior cingulate gyrus	(mri) left anterior orbital gyrus
(mri) left anterior temporal lobe lateral part	(mri) left anterior temporal lobe medial part	(mri) left caudate nucleus
(mri) left cerebellum	(mri) left corticospinal tract	(mri) left cuneus
(mri) left fusiform gyrus	(mri) left heart atrium	(mri) left heart atrium scar
(mri) left heart ventricle	(mri) left hippocampus	(mri) left inferior frontal gyrus
(mri) left insula anterior inferior cortex	(mri) left insula anterior long gyrus	(mri) left insula anterior short gyrus
(mri) left insula middle short gyrus	(mri) left insula posterior long gyrus	(mri) left insula posterior short gyrus
(mri) left kidney	(mri) left lateral orbital gyrus	(mri) left lateral remainder occipital lobe
(mri) left lateral ventricle excluding temporal horn	(mri) left lateral ventricle temporal horn	(mri) left lingual gyrus
(mri) left medial orbital gyrus	(mri) left middle and inferior temporal gyrus	(mri) left middle frontal gyrus
(mri) left nucleus accumbens	(mri) left optic radiation	(mri) left pallidum
(mri) left parahippocampal and ambient gyrus	(mri) left postcentral gyrus	(mri) left posterior cingulate gyrus
(mri) left posterior orbital gyrus	(mri) left posterior temporal lobe	(mri) left pre-subgenual frontal cortex
(mri) left precentral gyrus	(mri) left putamen	(mri) left straight gyrus
(mri) left subcallosal area	(mri) left subgenual frontal cortex	(mri) left substantia nigra
(mri) left superior frontal gyrus	(mri) left superior parietal gyrus	(mri) left superior temporal gyrus anterior part
(mri) left superior temporal gyrus middle part	(mri) left supramarginal gyrus	(mri) left thalamus
(mri) liver	(mri) liver tumor	(mri) lumbar vertebrae
(mri) lumbar vertebrae 1 (l1)	(mri) lumbar vertebrae 2 (l2)	(mri) lumbar vertebrae 3 (l3)
(mri) lumbar vertebrae 4 (l4)	(mri) lumbar vertebrae 5 (l5)	(mri) myocardial edema
(mri) myocardial scar	(mri) myocardium	(mri) necrotic brain tumor core
(mri) occipital lobe	(mri) optic radiation	(mri) pancreas
(mri) parietal lobe	(mri) peripheral zone of prostate	(mri) posterior hippocampus
(mri) prostate	(mri) pulmonary artery	(mri) right adrenal gland
(mri) right amygdala	(mri) right angular gyrus	(mri) right anterior cingulate gyrus
(mri) right anterior orbital gyrus	(mri) right anterior temporal lobe lateral part	(mri) right anterior temporal lobe medial part
(mri) right caudate nucleus	(mri) right cerebellum	(mri) right corticospinal tract
(mri) right cuneus	(mri) right fusiform gyrus	(mri) right heart atrium
(mri) right heart ventricle	(mri) right hippocampus	(mri) right inferior frontal gyrus
(mri) right insula anterior inferior cortex	(mri) right insula anterior long gyrus	(mri) right insula anterior short gyrus
(mri) right insula middle short gyrus	(mri) right insula posterior long gyrus	(mri) right insula posterior short gyrus
(mri) right kidney	(mri) right lateral orbital gyrus	(mri) right lateral remainder occipital lobe

Table 12 | Cont.

Name List 1	Name List 2	Name List 3
(mri) right lateral ventricle excluding temporal horn	(mri) right lateral ventricle temporal horn	(mri) right lingual gyrus
(mri) right medial orbital gyrus	(mri) right middle and inferior temporal gyrus	(mri) right middle frontal gyrus
(mri) right nucleus accumbens	(mri) right optic radiation	(mri) right pallidum
(mri) right parahippocampal and ambient gyrus	(mri) right postcentral gyrus	(mri) right posterior cingulate gyrus
(mri) right posterior orbital gyrus	(mri) right posterior temporal lobe	(mri) right pre-subgenual frontal cortex
(mri) right precentral gyrus	(mri) right putamen	(mri) right straight gyrus
(mri) right subcallosal area	(mri) right subgenual frontal cortex	(mri) right substantia nigra
(mri) right superior frontal gyrus	(mri) right superior parietal gyrus	(mri) right superior temporal gyrus anterior part
(mri) right superior temporal gyrus middle part	(mri) right supramarginal gyrus	(mri) right thalamus
(mri) sacrum	(mri) spleen	(mri) stomach
(mri) stroke	(mri) temporal lobe	(mri) thalamus
(mri) third ventricle	(mri) thoracic vertebrae	(mri) thoracic vertebrae 10 (t10)
(mri) thoracic vertebrae 11 (t11)	(mri) thoracic vertebrae 12 (t12)	(mri) thoracic vertebrae 9 (t9)
(mri) tibia bone	(mri) tibia cartilage	(mri) transition zone of prostate
(mri) urinary bladder	(mri) vertebrae	(mri) vestibular schwannoma
(mri) white matter	(mri) white matter hyperintensities	(pet) head and neck tumor
(pet) lymph node	(pet) tumor	

10.9 Dataset Details

Table 13 | The 72 datasets we collect to build up SAT-DS.

Dataset Name	#Scans	#Classes	#Annotati	Region
CT Data				
AbdomenCT1K [71]	988	4	3,950	Abdomen
ACDC [9]	300	4	1,200	Thorax
AMOS22 CT [40]	300	16	4,765	Abdomen
BTCV Abdomen [50]	30	15	448	Abdomen
BTCV Cervix [51]	30	4	118	Abdomen
CHAOS CT [43]	20	1	20	Abdomen
Couinaud [98]	161	10	1,599	Abdomen
COVID-19 CT Seg [69]	20	4	80	Thorax
CrossMoDA2021 [20]	105	2	210	Head and Neck
CT-ORG [90]	140	6	680	Whole Body
CTPelvic1K [62]	117	5	585	Lower Limb
DAP Atlas [39]	533	179	93072	Whole Body
FLARE22 [70]	50	15	750	Abdomen
FUMPE [73]	35	1	33	Thorax
HAN Seg [84]	41	41	1,681	Head and Neck
INSTANCE [58]	100	1	100	Brain
KiPA22 [33]	70	4	280	Abdomen
KiT23 [1]	489	3	1226	Abdomen
LNDb [82]	236	1	206	Thorax
LUNA16 [97]	888	4	3,551	Thorax
MM-WHS CT [126]	40	9	180	Thorax
MSD Colon [5]	126	1	126	Abdomen
MSD HepaticVessel [5]	303	2	606	Abdomen
MSD Liver [5]	131	2	249	Abdomen
MSD Lung [5]	63	1	63	Thorax
MSD Pancreas [5]	281	2	562	Abdomen
MSD Spleen [5]	41	1	41	Abdomen
NSCLC [8]	85	2	162	Thorax
Pancreas CT [93]	80	1	80	Abdomen
Parse2022 [64]	100	1	100	Thorax
PDDCA [88]	48	12	543	Head and Neck
SEGA [87]	56	1	56	Whole Body
SegRap2023 Task 1 [65]	120	61	7320	Head and Neck
SegRap2023 Task 2 [65]	120	2	240	Head and Neck
SegTHOR [49]	40	4	160	Thorax
SLIVER07 [34]	20	1	20	Abdomen
ToothFairy [17]	153	1	153	Head and Neck
TotalSegmentor Cardiac [106]	1,202	17	13,264	Whole Body
TotalSegmentor Muscles [106]	1,202	31	21,510	Whole Body
TotalSegmentor Organs [106]	1,202	24	20,361	Whole Body
TotalSegmentor Ribs [106]	1,202	39	32,666	Whole Body
TotalSegmentor Vertebrae [106]	1,202	29	19,503	Whole Body
TotalSegmentor V2 [106]	1,202	24	15,729	Whole Body
VerSe [95]	96	29	1,295	Whole Body
WORD [66]	150	18	2,700	Abdomen

Continued on next page

Table 13 | Cont.

Dataset Name	#Scans	#Classes	#Annotati	Region
MRI Data				
AMOS22 MRI [40]	60	16	896	Thorax
ATLAS [86]	60	2	120	Abdomen
ATLASR2 [59]	654	1	652	Brain
Brain Atlas [96]	30	108	3,240	Brain
BrainPTM [6]	60	7	408	Brain
BraTS2023 GLI [74]	5004	4	19680	Brain
BraTS2023 MEN [48]	4000	4	11420	Brain
BraTS2023 MET [76]	951	4	3476	Brain
BraTS2023 PED [44]	396	4	1328	Brain
BraTS2023 SSA [3]	240	4	940	Brain
CHAOS MRI [43]	60	5	300	Abdomen
CMRxMotion [103]	138	4	536	Thorax
FeTA2022 [81]	80	7	560	Brain
ISLES2022 [36]	500	1	492	Brain
LAScarQS2022 Task 1 [56]	60	2	120	Thorax
LAScarQS2022 Task 2 [56]	130	1	130	Thorax
MM-WHS MRI [126]	40	9	180	Thorax
MRSpineSeg [80]	91	23	1,783	Spine
MSD Cardiac [5]	20	1	20	Thorax
MSD Hippocampus [5]	260	3	780	Brain
MSD Prostate [5]	64	2	124	Pelvis
MyoPS2020 [85]	135	6	450	Thorax
PROMISE12 [60]	50	1	50	Pelvis
SKI10 [53]	99	4	396	Upper Limb
WMH [47]	170	1	170	Brain
PET Data				
autoPET [25]	501	1	501	Whole Body
HECKTOR2022 [4]	524	2	972	Head and Neck
Summary	22,186	497	302,033	/

10.10 Data Availability of SAT-DS

Table 14 | Downlinks of the 72 datasets in SAT-DS.

Dataset	Download Link
AbdomenCT1K [71]	https://github.com/JunMa11/AbdomenCT-1K
ACDC [9]	https://humanheart-project.creatis.insa-lyon.fr/database/
AMOS CT [40]	https://zenodo.org/records/7262581
AMOS MRI [40]	https://zenodo.org/records/7262581
ATLASR2 [59]	http://fcon_1000.projects.nitrc.org/indi/retro/atlas.html
ATLAS [86]	https://atlas-challenge.u-bourgogne.fr
autoPET [25]	https://wiki.cancerimagingarchive.net/pages/viewpage.action?pageId=93258287
Brain Atlas [96]	http://brain-development.org/
BrainPTM [6]	https://brainptm-2021.grand-challenge.org/
BraTS2023 GLI [74]	https://www.synapse.org/#!Synapse:syn51514105
BraTS2023 MEN [48]	https://www.synapse.org/#!Synapse:syn51514106
BraTS2023 MET [76]	https://www.synapse.org/#!Synapse:syn51514107
BraTS2023 PED [44]	https://www.synapse.org/#!Synapse:syn51514108
BraTS2023 SSA [3]	https://www.synapse.org/#!Synapse:syn51514109
BTCV Abdomen [50]	https://www.synapse.org/#!Synapse:syn3193805/wiki/217789
BTCV Cervix [51]	https://www.synapse.org/#!Synapse:syn3193805/wiki/217790
CHAOS CT [43]	https://chaos.grand-challenge.org/
CHAOS MRI [43]	https://chaos.grand-challenge.org/
CMRxMotion [103]	https://www.synapse.org/#!Synapse:syn28503327/files/
Couinaud [98]	https://github.com/GLCUnet/dataset
COVID-19 CT Seg [69]	https://github.com/JunMa11/COVID-19-CT-Seg-Benchmark
CrossMoDA2021 [20]	https://crossmoda.grand-challenge.org/Data/
CT-ORG [90]	https://wiki.cancerimagingarchive.net/pages/viewpage.action?pageId=61080890
CTPelvic1K [62]	https://zenodo.org/record/4588403#YyLq_OzaCo
DAP Atlas [39]	https://github.com/alexanderjaus/AtlasDataset
FeTA2022 [81]	https://feta.grand-challenge.org/data-download/
FLARE22 [70]	https://flare22.grand-challenge.org/
FUMPE [73]	https://www.kaggle.com/datasets/andrewmvd/pulmonary-embolism-in-ct-images
HAN Seg [84]	https://zenodo.org/record/
HECKTOR2022 [4]	https://hecktor.grand-challenge.org/Data/
INSTANCE [58]	https://instance.grand-challenge.org/Dataset/
ISLES2022 [36]	http://www.isles-challenge.org/
KiPA22 [33]	https://kipa22.grand-challenge.org/dataset/
KiTS23 [1]	https://github.com/neheller/kits23
LAScarQS2022 Task 1 [56]	https://zmiclab.github.io/projects/lascarqs22/data.html
LAScarQS2022 Task 2 [56]	https://zmiclab.github.io/projects/lascarqs22/data.html
LNDb [82]	https://zenodo.org/record/7153205#Yz_oVHbMJPZ
LUNA16 [97]	https://luna16.grand-challenge.org/
MM-WHS CT [126]	https://mega.nz/folder/UNMF2YYI#1cqJVzo4p_wESv9P_pc8uA
MM-WHS MR [126]	https://mega.nz/folder/UNMF2YYI#1cqJVzo4p_wESv9P_pc8uA
MRSpineSeg [80]	https://www.cg.informatik.uni-siegen.de/en/spine-segmentation-and-analysis
MSD Cardiac [5]	http://medicaldecathlon.com/
MSD Colon [5]	http://medicaldecathlon.com/
MSD HepaticVessel [5]	http://medicaldecathlon.com/
MSD Hippocampus [5]	http://medicaldecathlon.com/
MSD Liver [5]	http://medicaldecathlon.com/
MSD Lung [5]	http://medicaldecathlon.com/
MSD Pancreas [5]	http://medicaldecathlon.com/
MSD Prostate [5]	http://medicaldecathlon.com/
MSD Spleen [5]	http://medicaldecathlon.com/
MyoPS2020 [85]	https://mega.nz/folder/BRdnDISQ#FnCg9ykPITWYe5hrRZxi-w
NSCLC [8]	https://wiki.cancerimagingarchive.net/pages/viewpage.action?pageId=68551327

Continued on next page

Table 14 | Cont.

Dataset	Download Link
Pancreas CT [93]	https://wiki.cancerimagingarchive.net/display/public/pancreas-ct
Parse2022 [64]	https://parse2022.grand-challenge.org/Dataset/
PDDCA [88]	https://www.imagenglab.com/newsite/pddca/
PROMISE12 [60]	https://promise12.grand-challenge.org/Details/
SEGA [87]	https://multicenteraorta.grand-challenge.org/data/
SegRap2023 Task1 [65]	https://segrap2023.grand-challenge.org/
SegRap2023 Task2 [65]	https://segrap2023.grand-challenge.org/
SegTHOR [49]	https://competitions.codalab.org/competitions/21145#learn_the_details
SKI10 [53]	https://ambellan.de/sharing/QjrrntLwah
SLIVER07 [34]	https://sliver07.grand-challenge.org/
ToothFairy [17]	https://ditto.ing.unimore.it/toothfairy/
TotalSegmentator Cardiac [106]	https://zenodo.org/record/6802614
TotalSegmentator Muscles [106]	https://zenodo.org/record/6802614
TotalSegmentator Organs [106]	https://zenodo.org/record/6802614
TotalSegmentator Ribs [106]	https://zenodo.org/record/6802614
TotalSegmentator Vertebrae [106]	https://zenodo.org/record/6802614
TotalSegmentator V2 [106]	https://zenodo.org/record/6802614
VerSe [95]	https://github.com/anjany/verse
WMH [47]	https://wmh.isi.uu.nl/
WORD [66]	https://github.com/HiLab-git/WORD